UNIVERSITY OF OKLAHOMA

GRADUATE COLLEGE

INTEGRATED GEOPHYSICAL INVESTIGATION OF SHALLOW IGNEOUS BODIES AND THE IMPACT ON SESIMIC DATA QUALITY. CHICONTEPEC BASIN, MEXICO

A THESIS

SUBMITTED TO THE GRADUATE FACULTY

in partial fulfillment of the requirements for the

Degree of

MASTER OF SCIENCE

By

VICTOR DAVID PENA MARINO
Norman, Oklahoma
2010

INTEGRATED GEOPHYSICAL INVESTIGATION OF SHALLOW IGNEOUS BODIES AND THE IMPACT ON SESIMIC DATA QUALITY. CHICONTEPEC BASIN, MEXICO

A DISSERTATION APPROVED FOR THE
CONOCOPHILLIPS SCHOOL OF GEOLOGY AND GEOPHYSICS

BY

_____
Dr. Kurt J. Marfurt, Committee Chairman

_____
Dr. G. Randy Keller, Committee Member

_____
Dr. Tim J. Kwiatkowski, Committee Member

Dedication

This thesis is dedicated to all my family and friends.

Acknowledgments

I will like to thank my advisor Dr. Kurt Marfurt and committee members Randy Keller and Tim Kwiatkowski for their dedicated help and support. Thanks to PEMEX Exploración y Producción for permission to publish this work and particularly Sergio Chavez, Juan M. Berlanga, Proyecto Aceite Terciario del Golfo, for making our work possible through access to seismic data, support for the data reprocessing, and bits of help along the way. I thank Bunmi Elebiju and Bradley Wallet at OU for helping with the magnetic data and topographic information. I thank Roger Slatt, Gustavo Diaz, and Supratik Sarkar for helpful information about the geology of the area.

In this thesis, I have used a wide range of commercial software applications: Schlumberger's Petrel for interpretation, Landmark's Promax for processing, Tesseral for ray-trace and wave-equation modeling, and Hampson Russell's AVO for generating angle gathers and angle stacks. My support and attributes generated are thanks to the industry sponsors of OU's Attribute-Assisted Seismic Processing and Interpretation (AASPI) consortium.

Table of Contents

List of Tables

List of Figures

Abstracts

Unlike the world-famous Cantarel and Poza Rica carbonate fields, characterized by high-producing wells tapping large continuous reservoirs, the Chicontepec Play is characterized by thin, sometimes multi-storied turbidite and fan reservoirs that are incased in shales and cut by mud slumps and mass transport complexes. One of the major interpretational challenges is to differentiate between geologic 'noise' associated with slumps, turbidites, and small fans, and seismic noise associated with low fold, surface topography, and complex overburden. In the Amatitlan survey, one of the more difficult causes of seismic noise at the Chincontepec formation level is that of overlying intrusive and extrusive volcanics. Seismic modeling shows the down-going wave to be scattered by irregular igneous intrusive bodies. From my modeling experiments, I can demonstrate how stacked igneous bodies give rise to multiples and subsequently affect the seismic data. I use this insight along with seismic attributes and magnetic data to map the location of the shallow igneous features. These maps guide my subsequent velocity analysis in reprocessing the data. In this manner, I am able to suppress seismic noise while preserving the geologic noise such as mass transport complexes.

Chapter 1: Introduction

Although common in occurrence from Alaska to Patagonia, the 3D seismic expression of igneous bodies is somewhat under-reported in geological and geophysical literature. Davies et al. (2004) included in their volume on 3D seismic illumination of sedimentary basins, three excellent cases studies illustrating the seismic expression of igneous bodies in the North Sea. Recently, Garten et al. (2008) identified a volcanic vent on seismic acquired in the Norwegian Sea. In Latin America, Klarner et al. (2006) showed how 3D seismic can image not only shallow igneous bodies and submarine vents, but also deeper sills (Figure 1.1). Igneous bodies are routinely encountered in Argentina in both the Neuquen and San Jorge Basins (Juan Soldo and Daniel Delpino, personal communication). These images are commonly shown at oral presentations with published documentations more difficult to find. Although the igneous bodies can cause the same data quality problems as those we find in Amatitlán, Argentine igneous bodies can also serve alternatively as an updip seal, as the reservoir rock (if fractured), or as a cause of fracturing above intrusive dikes due to either the force of mechanical injection or due to subsequent differential compaction about these relatively rigid features. The igneous bodies in Argentina also have a profound effect on permeability. In some lithologies, igneous bodies reduce permeability through the formation of clays; in others igneous bodies improve permeability through some kinds of leaching processes.

The Chicontepec Basin is one of the most productive basins in Mexico. Unlike the world-famous Cantarell and Poza Rica carbonate fields, characterized by high-producing wells tapping large continuous reservoirs, the Chicontepec Play is characterized by thin, sometimes multi-storied turbidite and fan reservoirs that are incased in shales and cut by

mud slumps and mass transport complexes. These sand reservoirs are relatively small and have very low permeability. Most modern wells need to be hydraulically fractured, with anomalously higher production being hypothesized as due to fractures draining nearby, otherwise disconnected sand bodies.

Mapping laterally-discontinuous, thin sand fans and turbidites is difficult even when using the best of seismic data. These problems are exacerbated in the Amatitlán seismic survey, acquired in the northern end of the Chicontepec Basin, where rough topography, dense forestation, human habitation, and archaeological sites cause lateral amplitude and signal-to-noise heterogeneity. It is important to note that these heterogeneities are due to acquisition obstacles, rather than to geology. Further complicating the effort of maintaining data fidelity is the presence of shallow volcanic sills (and perhaps shallow volcanic extrusives).

Given the relative paucity of published 3D seismic images of igneous bodies, one of the primary objectives of this work is to not only to map them but to quantify the negative impact they may have on seismic data quality. A future question to be addressed is whether there is any correlation between the igneous bodies in Amatitlán and the field's overall poor permeability.

1.1 Objective for the study

The first objective of this thesis is to quantify the negative impact igneous bodies may have on seismic data quality. I will show how integration of post stack and prestack seismic data, seismic modeling, magnetic data, and well logs can help identify intrusive and extrusive igneous bodies.

The study focused on the northern part of the Chicontepec basin where the 3D seismic "Amatitlan" survey was acquired in 2003 with the objective of better understanding and delineating the reservoir. The Amatitlán survey was both more expensive and more difficult to acquire than most other surveys. In addition to rugged topography, dense forestation, human settlements, and sensitive archaeological sites, there are strong impedance anomalies in the shallow section that generate amplitude shadows deeper in the section. For this reason, the Amatitlán survey was reprocessed in 2007 with the objective of obtaining better shallow imaging. The new processing flow did not introduce new processing technology, but rather focused on much more detailed, processor-intensive attention to details in trace editing, amplitude balancing, statics, regularization, and a rather careful, very detailed velocity analysis. After this basic reprocessing, the data were prestack Kirchhoff time migrated; the migrated gathers were subjected to residual NMO corrections, random noise attenuation, and multiple suppression.

Even with this careful reprocessing, artifacts due to variable fold and shallow volcanic intrusives remain. For this reason, the second objective of this thesis to reprocess the data with careful attention to velocity analysis, NMO correction, and the quality of the angle gathers that will facilitate future inversion for P- and S-impedances by Supratik Sarkar. Specifically, I aim to improve resolution in areas below the igneous intrusive and extrusive bodies.

1.2 Available data

The available data for the study have been provided by PEMEX and consist of:

1. 2 versions of the poststack 3D seismic data (Amatitlan 3D survey) one processed in 2003 and the reprocessed in 2007

2. A prestack version of the 3D seismic data (Amatitlan 3D survey) provided in SEGY format

3. Outcrop analogues located in the Sierra Madre Oriental where the Chicontepec formation is exposed (acquired by Supratik Sarkar, Gustavo Diaz, Brad Wallet, and Steve Cossey)

4. 324 wells with conventional log suites provided in LAS format

1.3 Methodology overview

In order to better understand the effects of igneous bodies on seismic data quality, and to improve the vertical and lateral resolution on seismic data, a combination of different geophysical methods will be integrated. This includes the following steps:

- Review of previous geophysics work done on seismic expression of igneous bodies
- Analysis and integration of the different data set
- Multiattribute analysis
- Integration of magnetic data with seismic data
- Acoustic and elastic seismic modeling
- Reprocessing of the seismic data

1.4 Thesis Significance

The integration of magnetic data, seismic attributes, data reprocessing, seismic modeling, and structural-oriented filter will help better image and understand the Chicontepec formation, especially on those areas below the igneous intrusive and extrusive cover a large portion of the shallow section. Ideally, this case study will serve as one of a sequence of future studies to better understand the impact of igneous bodies on seismic data quality and reservoir characterization.

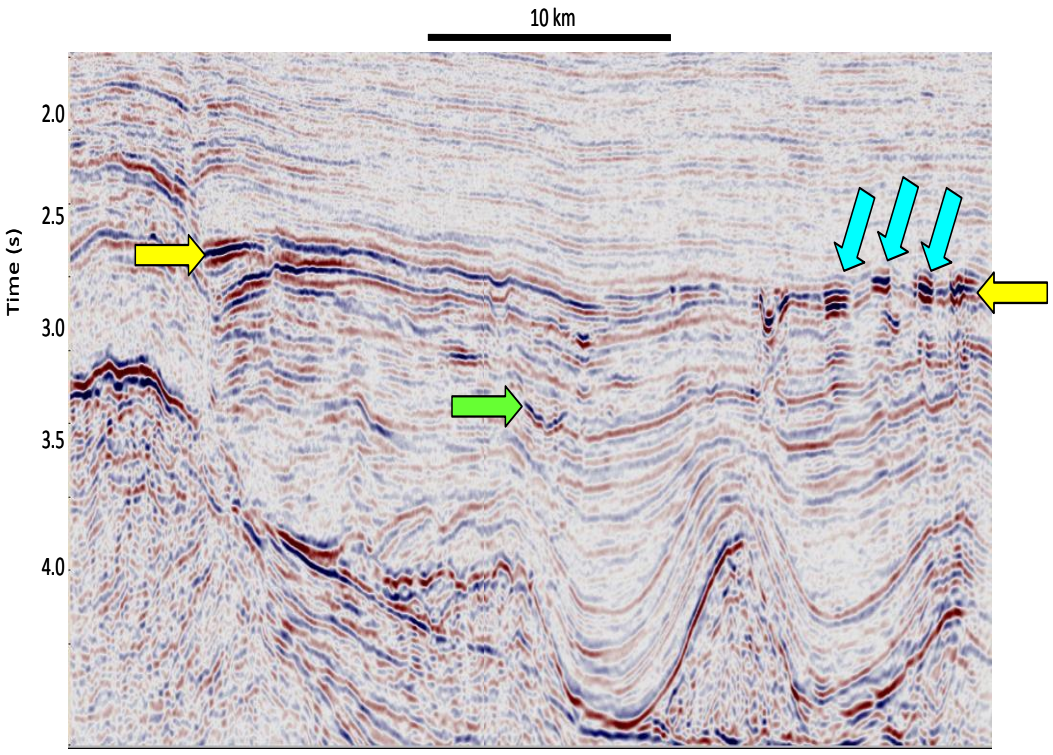

Figure 1.1 *The seismic expression of volcanics in the Santos Basin, offshore Brazil. Yellow arrows indicate a shallow lava flow that has since been buried. Cyan arrows are volcanic vents identified as circular features on the horizon slice. Green arrow indicates an intrusive sill. (After Klarner et al., 2006).*

Chapter 2: Geology Setting

The Mexican part of the Gulf of Mexico basin can be divided into five areas: (1) The Burgos Basin, (2) The Southeast Basin, (3) The Eastern Continental Margin (ECM), (4) The Yucatan Peninsula, and (5) The Abyssal Plain. Of these areas, the Burgos and Southeast Basins developed over transitional or stretched continental crust and have thick, earliest Late Jurassic salt deposits. The Eastern Continental Margin and the Yucatan Peninsula developed over rifted continental crust. The Abyssal Plain is thought to have developed over much-stretched continental or oceanic crust (Pindell and Kennan, 2001; Diaz, 2008).

The Paleogene Chicontepec Formation was deposited between the Sierra Madre Oriental and the Golden Lane Platform, extending northwest-southeast along the Gulf Coast in Mexico (Figure 2.1). This formation is made of submarine fan turbidity sediments derived from the Sierra Madre Oriental to the west of the basin and is composed mainly of alternating shales and thin-bedded sandstones (Figure 2.2). The formation has a thickness of ~2000 m covering most of the 3731 km² western Gulf of Mexico Tampico-Misantla Basin, (Bermúdez et al., 2006). Although the Chicontepec play was discovered in 1925, production did not begin until 1952. Previous sedimentological studies demonstrate that there were multiple sediment supply systems forming submarine fans along the western margin of the Chicontepec Formation. Sediments derived from the uplifted Mesozoic carbonate units were deposited along a deep marine foreland basin developed eastward of the deformation front of the Sierra Madre Oriental fold-thrust belt.

The Tampico-Misantla Basin tectonostratigraphic history can be divided into four major stages: (1) Late Triassic-Callovian rifting related to the breakup of Pangea, development of linear grabens and half-grabens, and opening of the Gulf of Mexico; (2) Late Jurassic-Early Cretaceous drift stage, passive margin development, and widespread marine transgression; (3) Late Cretaceous marine connection of the Gulf of Mexico Basin to the Pacific Ocean; and (4) Late Cretaceous-Early Tertiary Laramide Orogeny, due to subduction of an oceanic plate or plates under the Pacific margin of the North American plate; uplift of the Sierra Madre Oriental in eastern Mexico and the Sierra Madre de Chiapas in southeastern Mexico, and associated foredeep development (Morán-Zenteno, 1994; Cantú-Chapa, 2001a; Goldhammer and Johnson, 2001; Diaz, 2008).

Triassic-Jurassic graben development initially led to the formation of predominantly non-marine red-bed sequences and associated volcanic and during the Middle Jurassic extensive salt deposits accumulated in the southern and northern Gulf of Mexico (Diaz, 2008).

During Late Jurassic-Early Cretaceous, passive-margin development and widespread marine transgression changed the palaeogeography of the Gulf of Mexico. Seawater entered the basin from the Pacific Ocean across central Mexico, and by mid-Oxfordian time, a large inland sea with unrestricted circulation and normal salinity was well-developed. Carbonates and shales of the Tepexic, Santiago, Taman and San Andrés Formations were deposited at this time in the Tampico-Misantla Basin (Figure 2.3) (Salvador, 1991; Goldhammer and Johnson, 2001; Diaz, 2008).

During the Late Paleocene-Early Eocene, fine-grained clastic sediments of the Chicontepec Formation (partly turbiditic) were derived from the west and from the Tuxpan Platform to the east, and deposited in submarine canyons within the east-migrating foredeep. In the late Middle or Late Eocene, continuing uplift of the western uplands gave rise to the deposition of coarser clastics predominantly in the western part of the Tampico-Misantla Basin (Diaz, 2008).

During the Oligocene, the west-to-east, proximal-to-distal depositional relationship continued (Goldhammer and Johnson, 2001), along with alternating transgressive and regressive episodes. These gave rise to the deposition of coarse-grained nonmarine and shallow marine clastics in the western part of the basin (Palma Real and Meson Formations) with eastward lateral changes of facies into marine shales (Horcones and Alazan Formations). A major flooding event initially drowned topography associated with the middle Oligocene uplift. Across the whole basin, clastic shelf systems appear to have become rapidly established and were strongly progradational (Horbury et al., 2003; Diaz, 2008).

The normal stratigraphic succession places the Chicontepec Formation disconformably on top of the Upper Cretaceous marls of the Méndez Formation. However, the most accepted interpretation is of a deeply-eroding submarine canyon north of the modern city of Poza Rica that suggests that the Chicontepec Formation rests unconformably on older rocks ranging from Lower Eocene to Upper Jurassic.

The geological column has been investigated from the Lower Jurassic to Upper Oligocene. In the southeastern area, the Tertiary Chicontepec deposits rest discordantly

on the Upper Jurassic San Andres, in the central and northern part, underlie the Cretaceous Superior Mendez. The Paleocene section is comprised of the Velasco Formation, Lower Chicontepec and Middle Chicontepec; the Lower Eocene by the formations Aragon and Upper Chicontepec Channel; the Middle Eocene by the Guayabal formation and the upper Eocene by formations Tantoyuca and Chapopote (Figure 2.4).

While the Chicontepec Basin includes some 29 oil and gas fields. The Amatitlán seismic survey is situated in the northern part of the basin to the west of Tuxpan, Veracruz. The reservoir facies are highly compartmentalized and in general have very low permeability. The most commonly accepted description of the reservoirs is one of the submarine turbidites and fans deposited from the west (and possibly from the east) sides of the basin margin. Although channel-like features have been mapped by 2D lines to the south of the play, these features have low permeability and it is unclear whether they are turbidites or mass-transport complexes. The 3D Amatitlán survey was acquired in 2003 with the objective of better understanding and delineating the compartmentalized reservoir. While the deeper carbonate Mesozoic section is extremely well imaged, it is not clear whether the shallower Paleocene objective is incoherent because of an inherently chaotic depositional nature, due to the shallow acquisition obstacles, or because of shallow volcanics in the section giving rise to both 'penetration' problems and lateral velocity heterogeneities.

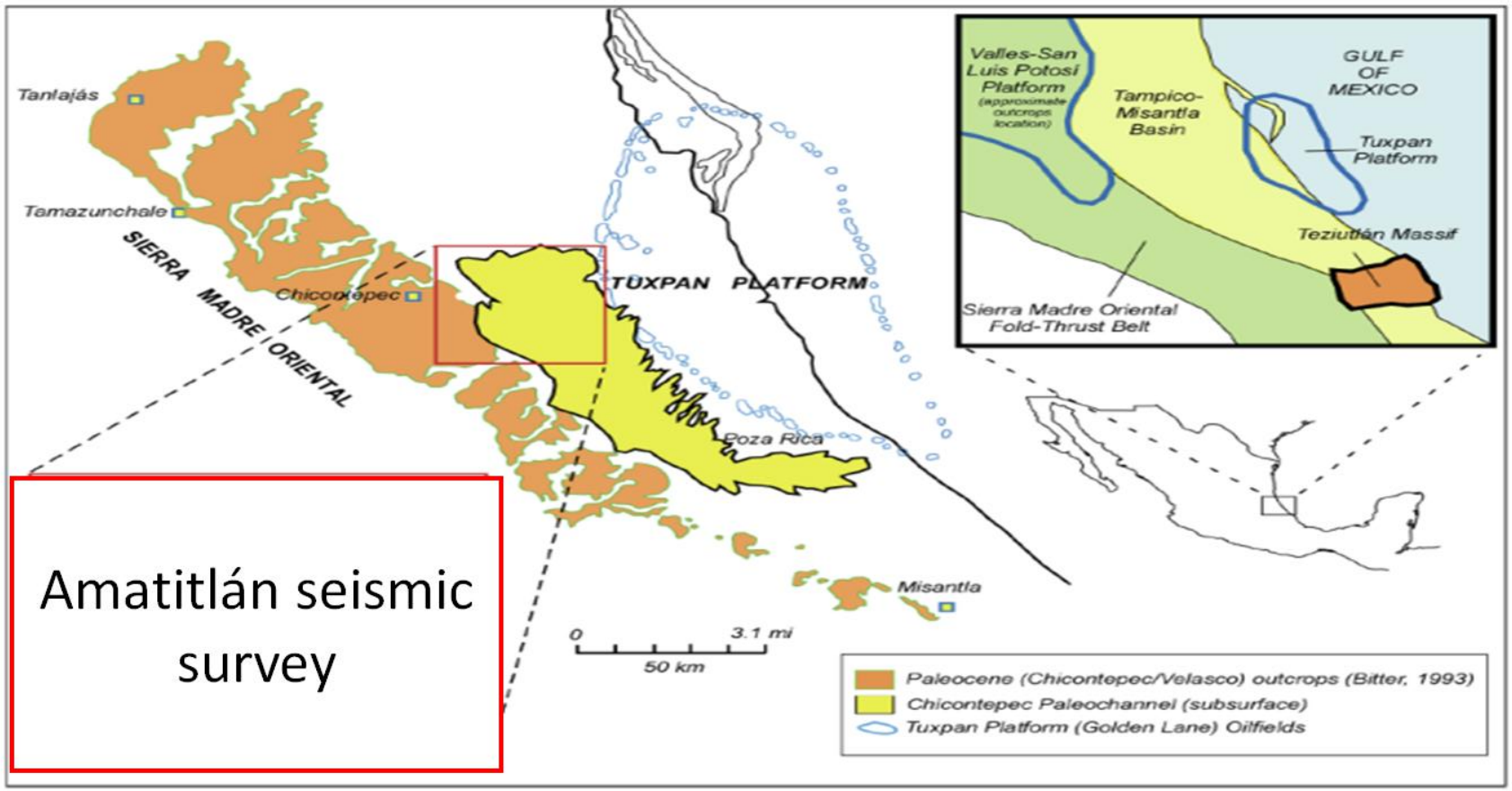

Figure 2.1. *Location of the Chicontepec Basin and the Amatitlán seismic survey. (After Abbaszadeh et al., 2003).*

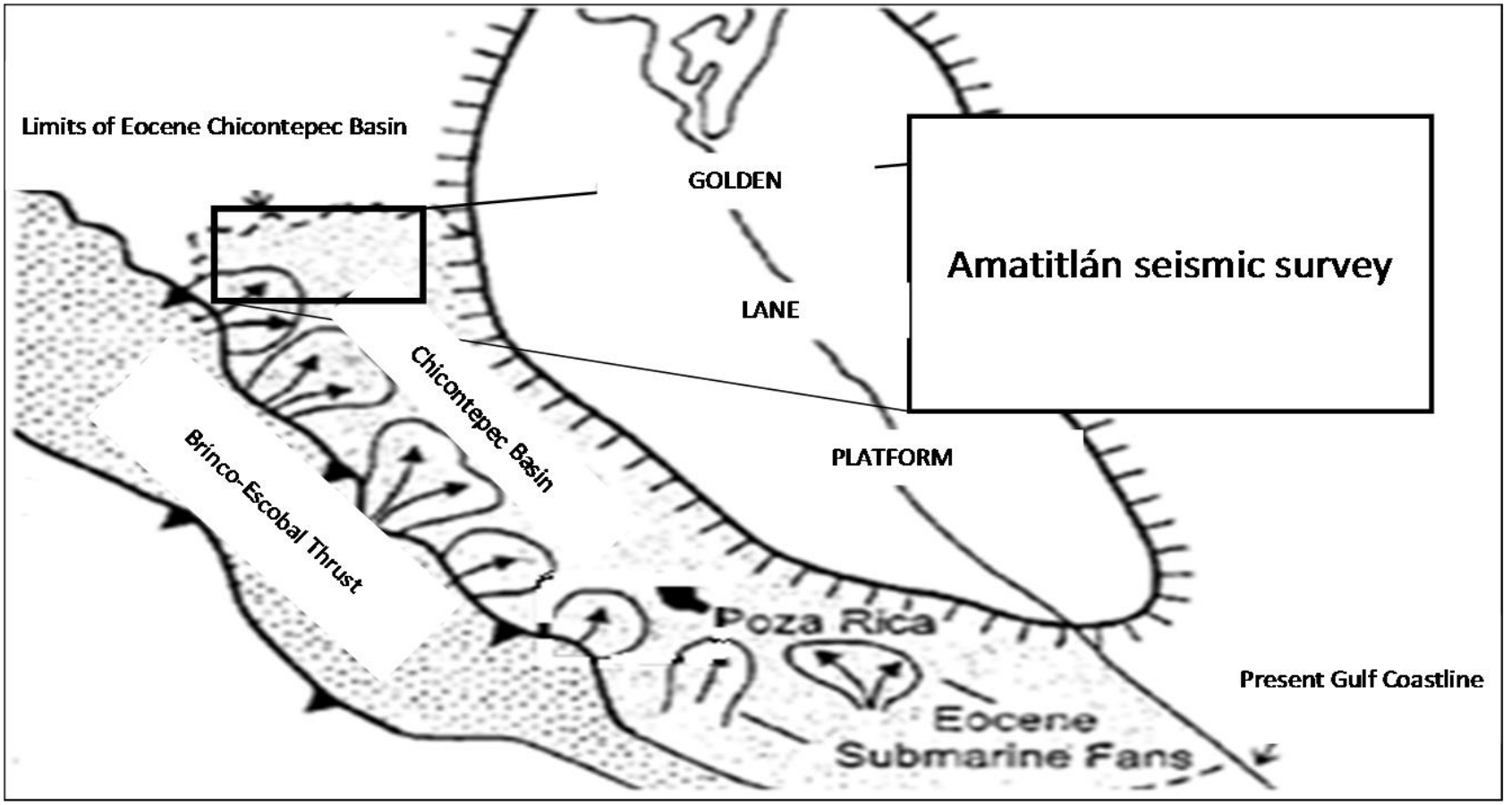

Figure 2.2 *Paleogeographical map of the Paleogene Chicontepec Basin. (After Abbaszadeh et al., 2003).*

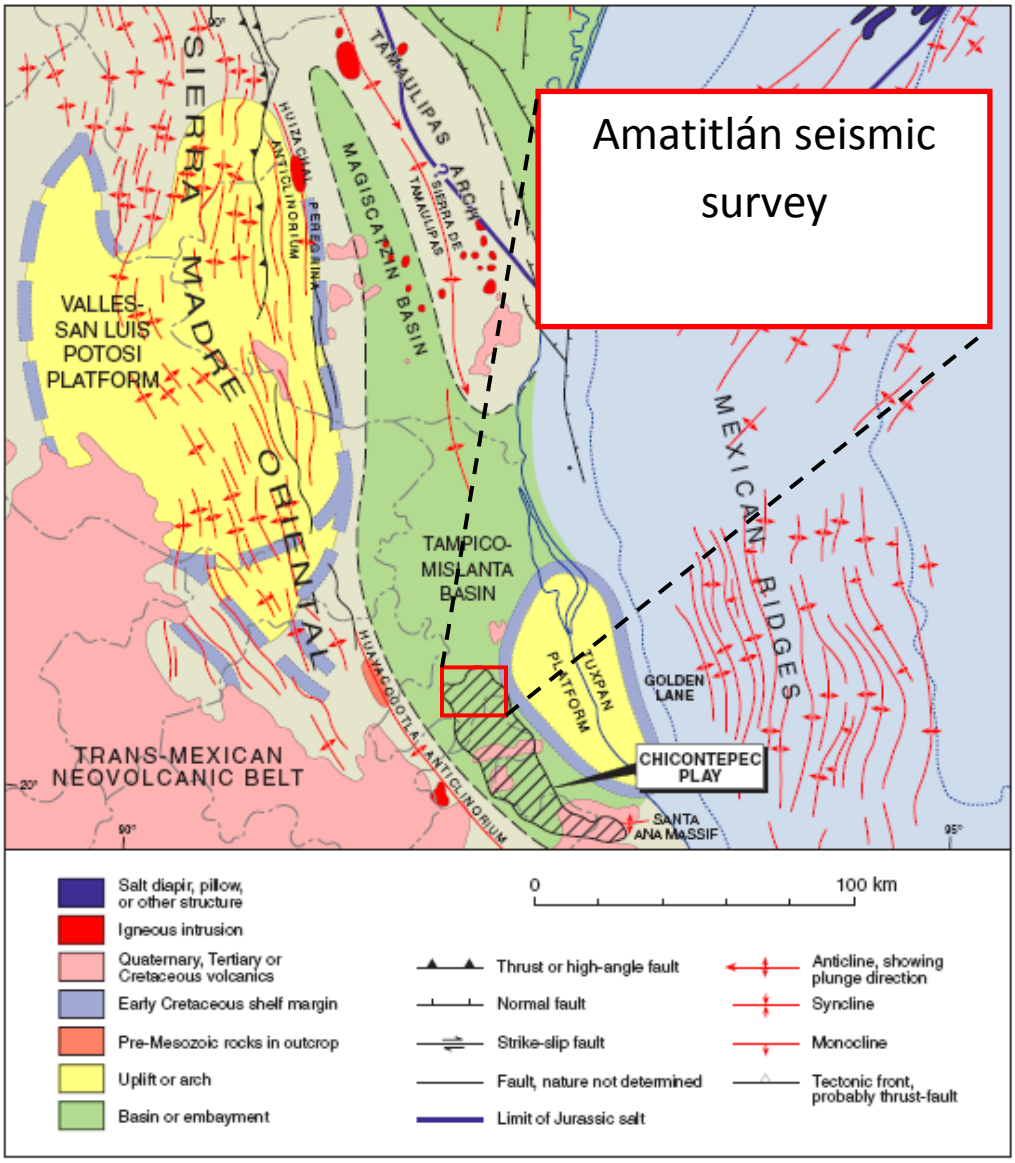

Figure 2.3. *Regional structural setting of the Tampico-Misantla Basin of east-central Mexico, west of the Tuxpan platform. Note that the trans-Mexican neovolcanic belt (in pink) extends east into the study area. (After Salvador, 1991; Goldhammer and Johnson, 2001; Diaz, 2008).*

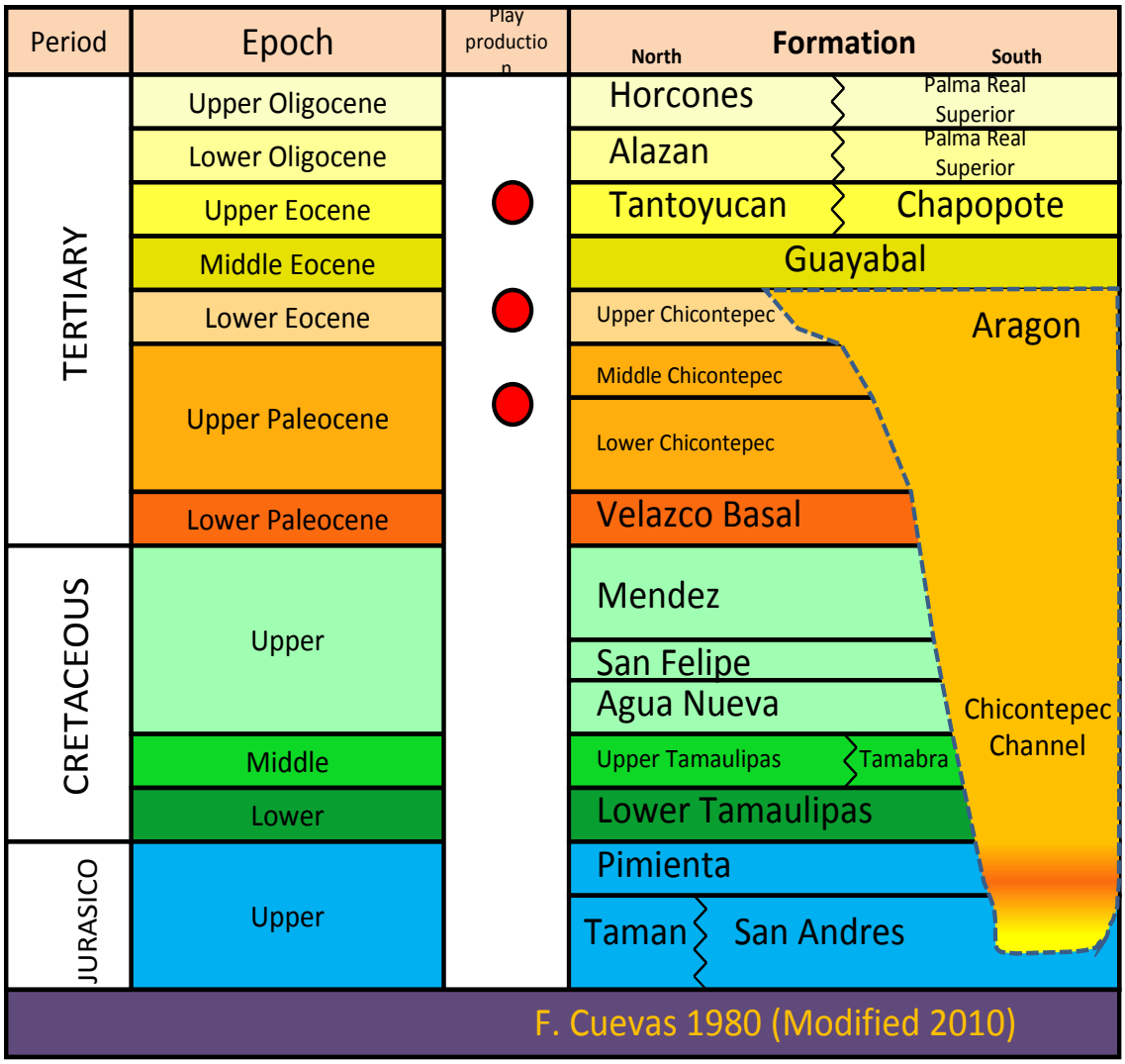

Figure 2.4. *Regional Geologic Column. (After F. Cuevas 1980; Modified 2010).*

Chapter 3: Seismic Data Quality

The data were originally acquired and processed in 2003 using a well-established acquisition and processing workflow that had proven effective in other areas of Veracruz State. However, the Amatitlán survey was both more expensive and more difficult to acquire than most other surveys. In addition to rugged topography, dense forest, human settlements, and sensitive archaeological sites, there appeared to be strong impedance anomalies in the shallow section that generated amplitude shadows deeper in the section (Figure 3.1a). For this reason, the Amatitlán survey was reprocessed in 2007 with the objective of obtaining better shallow imaging. The new processing flow did not introduce new processing technology, but rather focused on much more detailed, much more processor-intensive attention to details in trace editing, amplitude balancing, statics, regularization, and a careful, very detailed velocity analysis. After this basic reprocessing, the data were prestack Kirchhoff time migrated; the migrated gathers were subjected to residual NMO corrections, random noise attenuation, and multiple suppression.

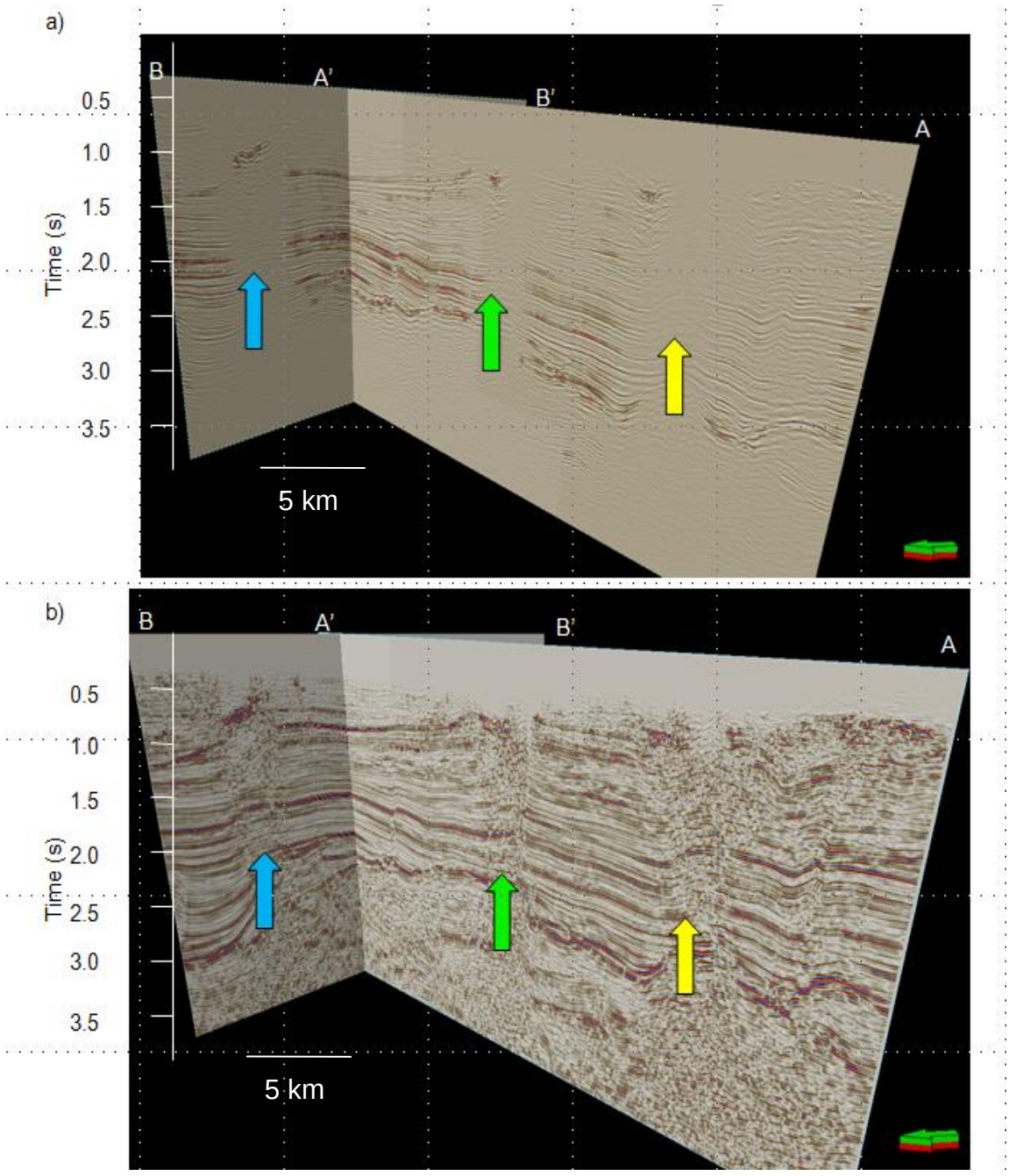

Figure 3.1. *Vertical slices along lines AA' and BB' through the seismic amplitude volume generated using the (a) original and (b) improved processing flow. Arrows indicate low-amplitude chaotic zones that we interpret to be due to shallow overlying volcanics. Location of lines shown in Figure 5.5.*

Chapter 4: Attribute Expression of Intrusive and Extrusive Igneous Rocks

A seismic attribute is any measure of seismic data that helps us visually enhance or quantify features of interpretation interest. Seismic attributes are a powerful aid to seismic interpretation allowing the geoscientist to interpret faults and channels, recognize the deposition environment, and unravel the structural deformation history more rapidly (Chopra and Marfurt, 2007). Generally, igneous bodies have high impedance, such that when encased in a sedimentary matrix, tey give rise to an strong impedance contrast, and high amplitude reflection. Rugose surfaces give rise to incoherent back-scattered and forward-scattered diffractions.

For this work, I use seismic attributes to identify and characterize igneous intrusive bodies from my 3D seismic volume. Figure 4.1 displays a time slice through the Amatitlán seismic amplitude volume. Note the effect of shallower ingenuous bodies on the reflection quality (yellow, green, and blue arrows). Note the strong reflection (red arrow) associated with an igneous body cut by the time slice. Blending the seismic amplitude with the coherence highlights the chaotic, poor data quality areas (yellow, green, and blue arrows) as well as the edges of the intrusive igneous body cut the time slice (red arrow) (Figure 4.2).

Below is a list of seismic attributes that I found which aided in the identification of igneous bodies on 3D seismic data.

4.1 Dip Magnitude Attribute

Seismic reflection events can be approximated by local tangent planes that in turn can be represented by dip magnitude and dip azimuth. The apparent dip is the angle measured in the vertical x-z and y-z planes from the horizontal to the interface. Dip components are sensitive to the rugose nature of intrusive igneous bodies, such as those seen in the Amatitlán survey. The dip magnitude attribute show artifacts below for the shallow igneous bodies (yellow, green, and blue arrows) and the top of igneous intrusive cut by the time slice is rogues (red arrow) (Figure 4.3).

4.2 Similarity Attribute

4.2.1 Sobel Filter Similarity

Sobel filter similarity is an amplitude-sensitive, multitrace attribute. Introduced by Luo et al. (1996). the computation has three steps. First, derivatives along a plane defined by reflector dip and azimuth are taken. Secondly, these derivatives are stacked along a vertical analysis window to improve the signal-to-noise ration. Finally, the result is normalized by dividing the differences made by the energy off the input traces, such that relative changes in amplitude rather than absolute changes are measured (Chopra and Marfurt, 2007).

Highly similar waveforms having the same amplitude maps to white. Chaotic areas map to black. Figure 4.4 shows that the Sobel filter delineates the chaotic areas due to the shallower ingenuous bodies effects (yellow, green, and blue arrows). It also maps the edges of the igneous bodies indicated by the red arrow.

4.2.2 Energy-ratio Coherence

Like Pierson normalized cross-correlation, energy ratio similarity is sensitive only to changes in waveforms, and not to changes in amplitude. The configuration involves KL-filtering a window of data, computing its energy, and then normalizing by the energy of the unfiltered data (Chopra and Marfurt, 2007).

For large offset discontinuities, energy-ratio coherence will usually show sharper images than semblance or Sobel filter similarity. This is the case for the Amatitlán survey data. The chaotic area due to the shallow igneous bodies is better defined (yellow, green, and blue arrows) while the edges of the igneous intrusive out by the time slice (red arrow) is better delineated. Faults are also better delineated (orange arrows) (Figure 4.5).

4.3 Curvature Attribute

Curvature calculations performed directly on the dip and azimuth cubes provide good edge-detection images for high-quality data (Chopra and Marfurt, 2007). Numerous types of curvature can be determined at every point on a gridded surface by fitting a quadratic surface to the data and using the coefficients of the quadratic equation. The curvature of the tangent circle with the smallest radius in a normal plane is called the maximum curvature, k_{max}. The curvature of the tangent circle in the normal plane perpendicular to this has the minimum curvature, k_{min}, such that $|k_{max}| > |k_{min}|$. Alternatively, k_{min} and k_{max} can be expressed as the most-positive and most-negative principal curvatures, k_1

and k_2, where $k_1 = MAX(k_{max}, k_{min})$ and $k_2 = MIN(k_{max}, k_{min})$, such that the signed values $k_1 \geq k_2$.

For this work, the most-positive and most-negative principal curvature provided the best result for imaging the igneous bodies' effects and features. Figure 4.6 displays the definition of 3D quadratic shapes expressed as a function of the most positive and most negative principal curvature. In Figure 4.7, I blended coherence, most positive, and most negative attributes to demonstrate how well curvature resolves the shallow igneous bodies' effects (yellow, green, and blue arrows) and edges of the igneous intrusive cut by the time slice (red arrow). Not only does this blending of multiple attributes image the edges of igneous features, but it also locates the fault zone running northwest-southeast (orange arrow).

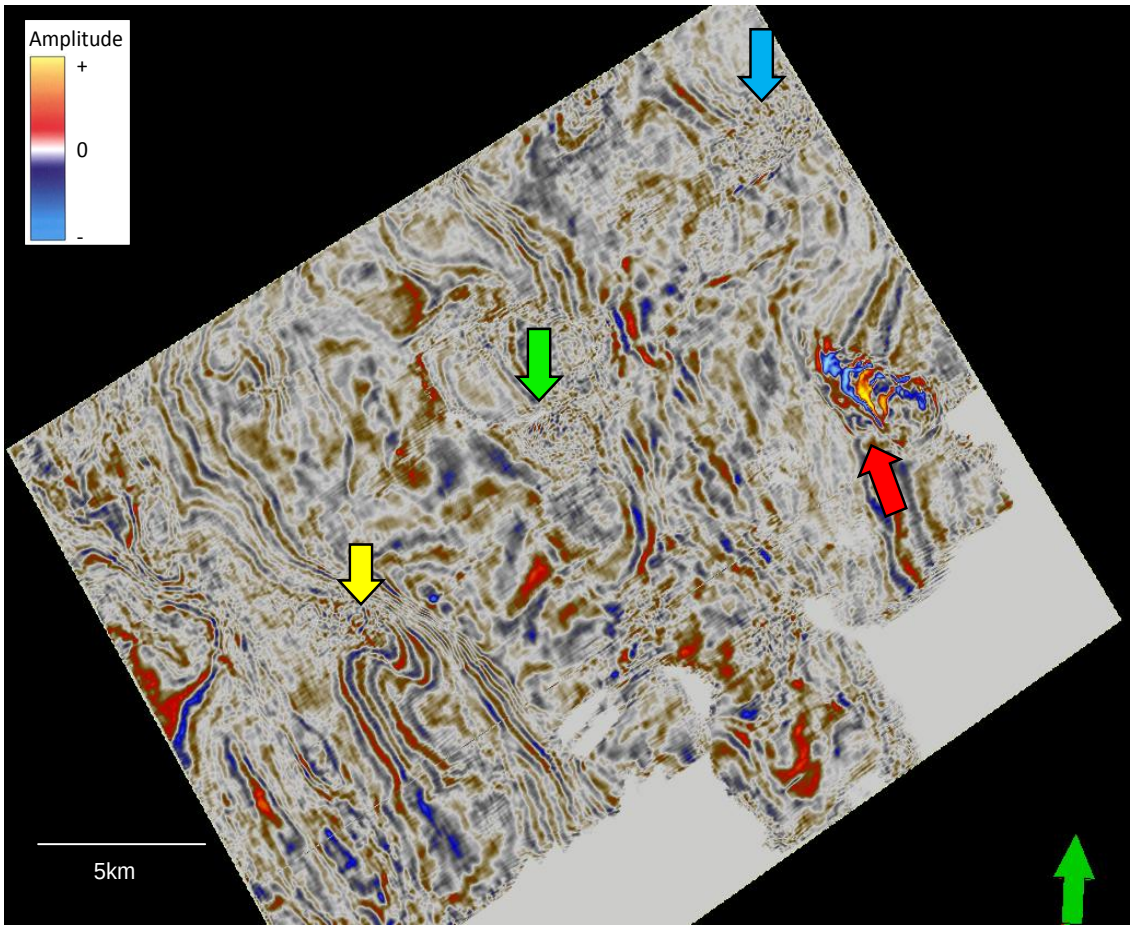

Figure 4.1 *Amplitude time slice at t=1335ms.Yellow, green, and blue arrows indicate incoherent seismic energy on the time slice affected by shallower igneous bodies. Red arrow indicates high amplitude reflections of an igneous body cut by the timeslice.*

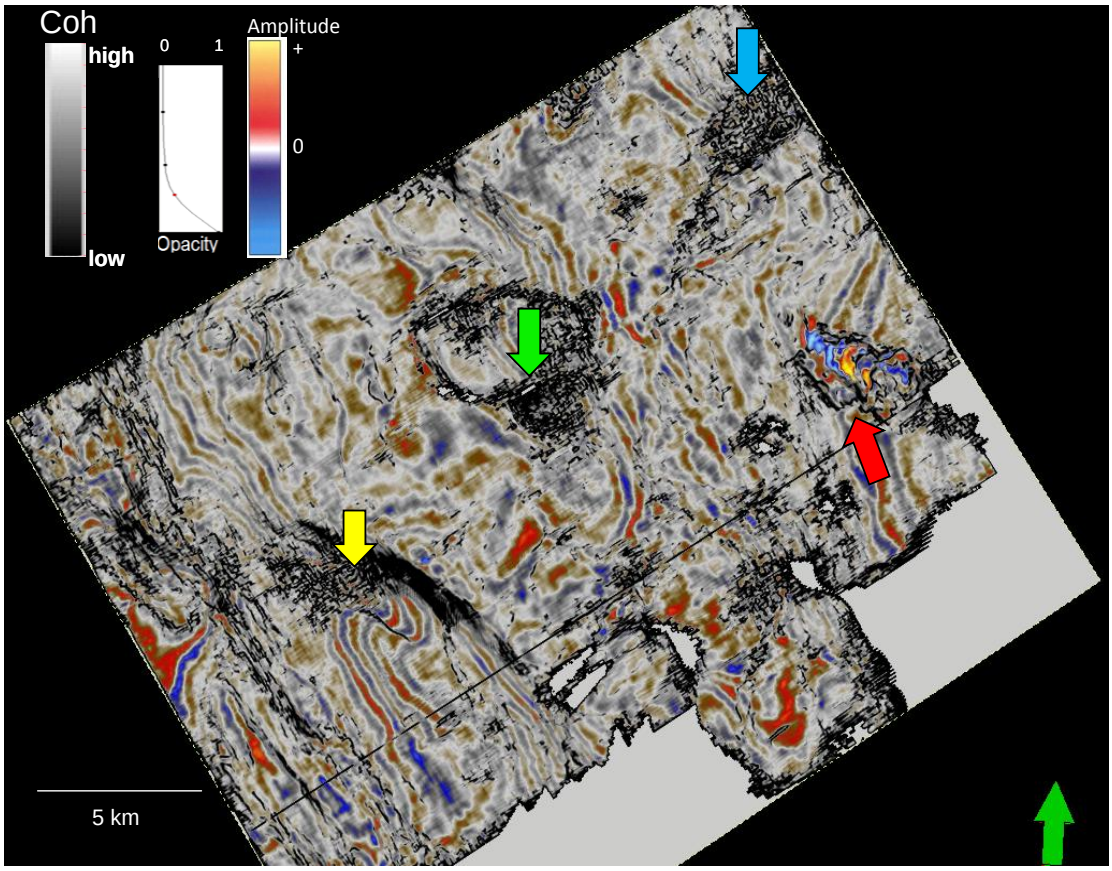

Figure 4.2 *Co-rendering using transparency in a timeslice at t=1335ms through seismic amplitude modulated by coherence. Yellow, green, and blue arrows indicate incoherent seismic energy on the time slice affected by shallower igneous bodies. Red arrow indicates high amplitude reflections of a igneous body cut by the timeslice.*

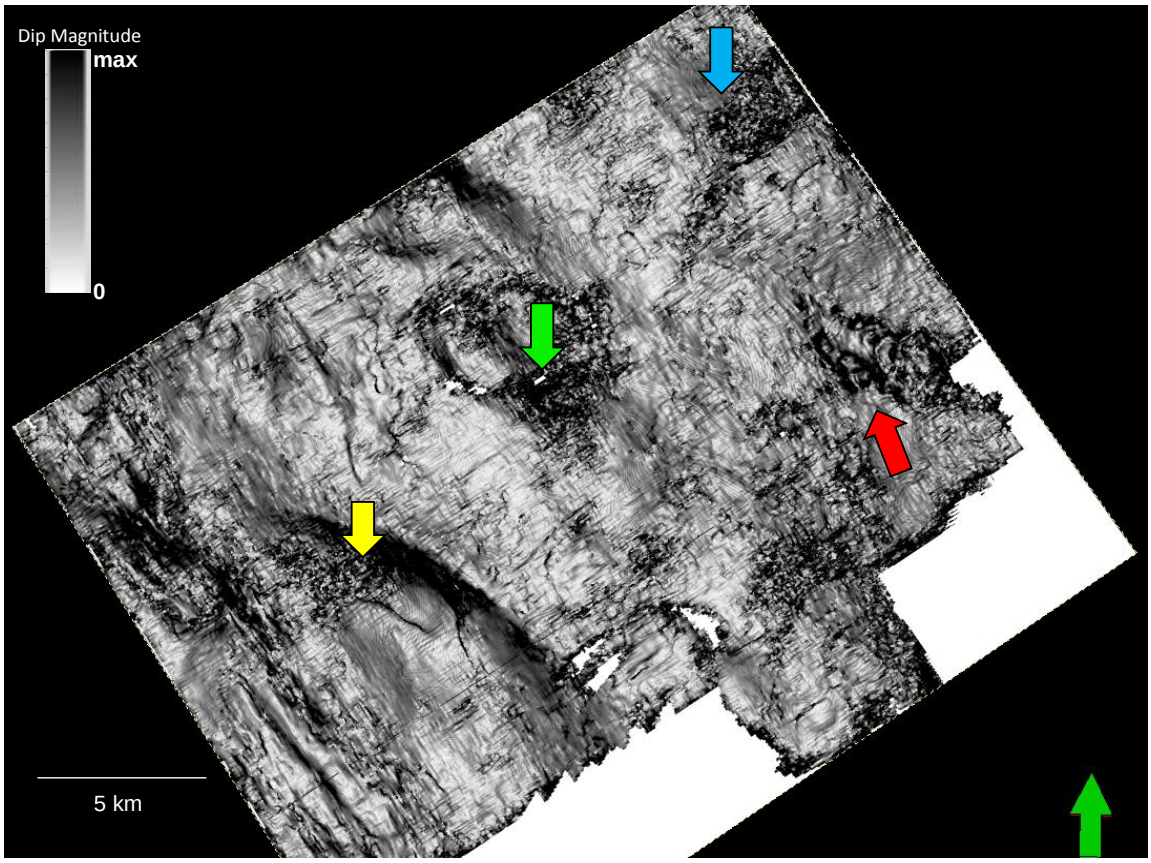

Figure 4.3 *Time slice at t= 1335ms through the dip magnitude volume. Yellow, green, and blue arrows indicate steeply dipping chaotic noise due to shallow igneous bodies. Red arrow indicates an igneous body cut by the time slice that has steep (high dip magnitude) edges. NE-SW lineaments are an acquisition footprint artifact associated with migration operator aliasing.*

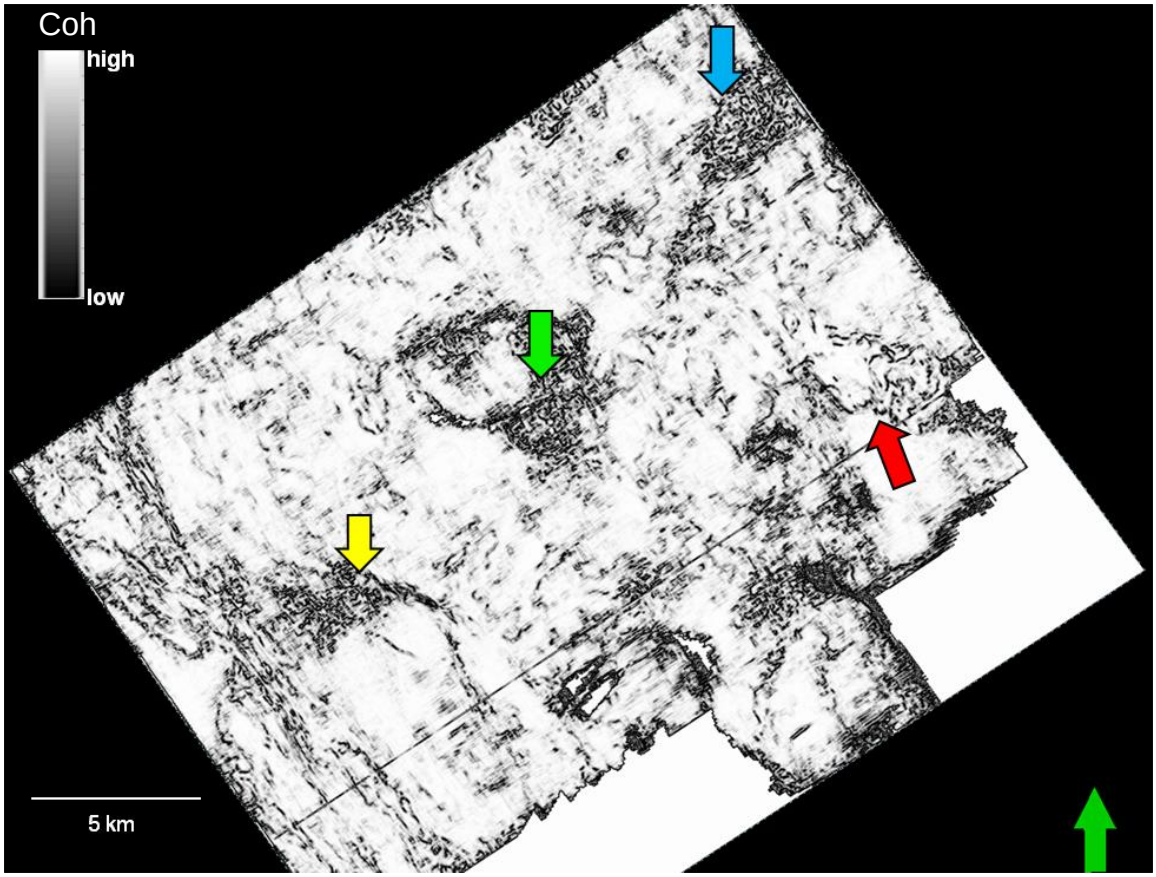

Figure 4.4 *Sobel filter similarity time slice at t= 1335ms. Yellow, green, and blue arrows indicate chaotic zones due to shallower igneous bodies. Red arrow indicates igneous body cut by the time slice.*

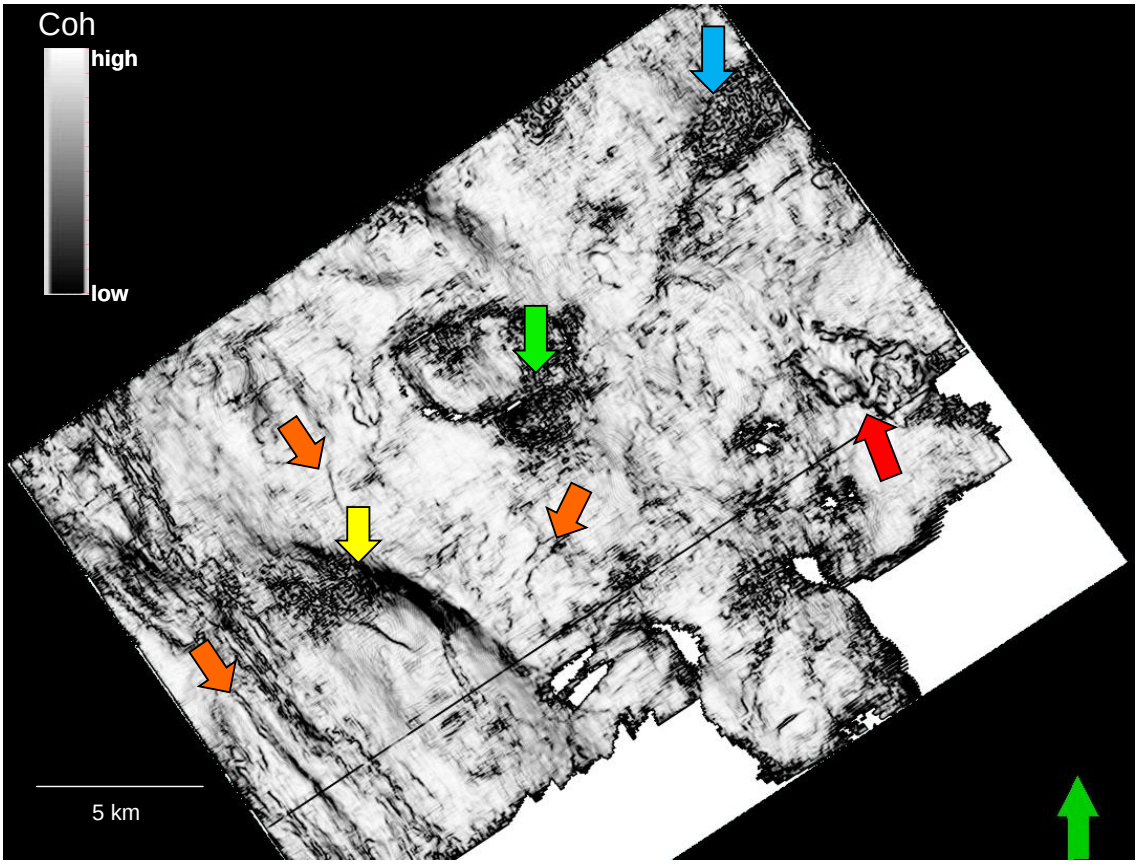

Figure 4.5 *Energy-ratio coherence attribute time slice at t= 1335 ms. Yellow, green, and blue arrow indicate chaotic zones due to shallower igneous bodies. Red arrow indicates igneous body cut by the timeslice that is well-delineated. Overall, this image is similar to the Sobel filter similarity image displayed in Figure 4.4. However, the faults are better delineated (orange arrows).*

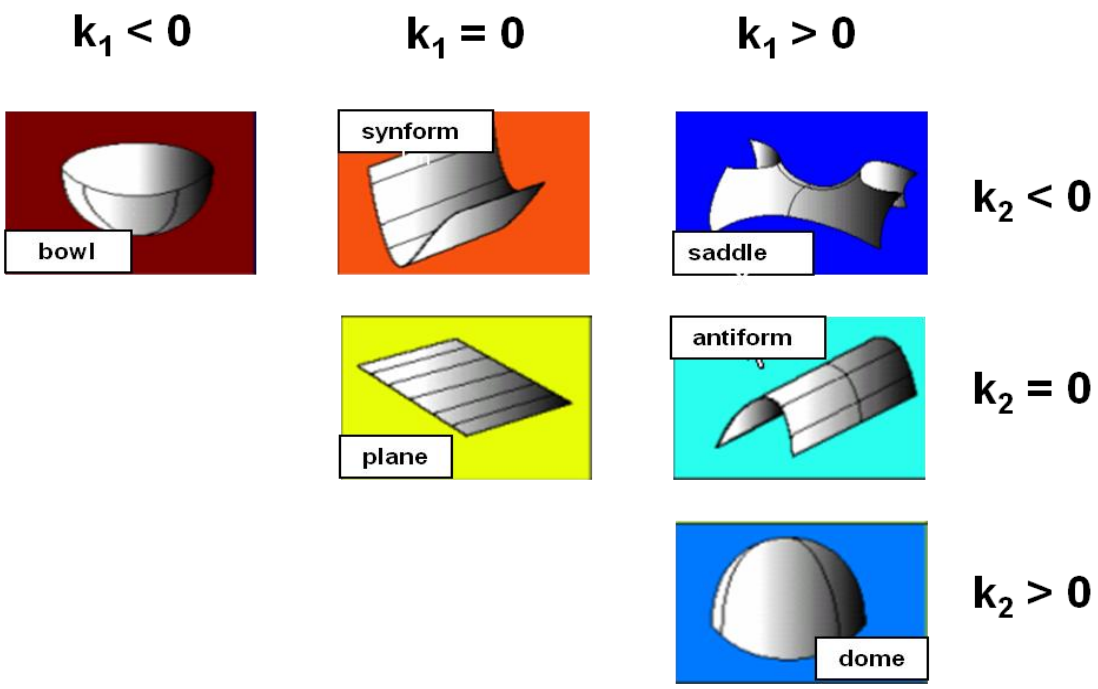

Figure 4.6 *The definition of 3D quadratic shapes expresses as a function of the most- positive and most negative principal curvatures, K_1, and K_2. (after Bergbauer et al., 2003).*

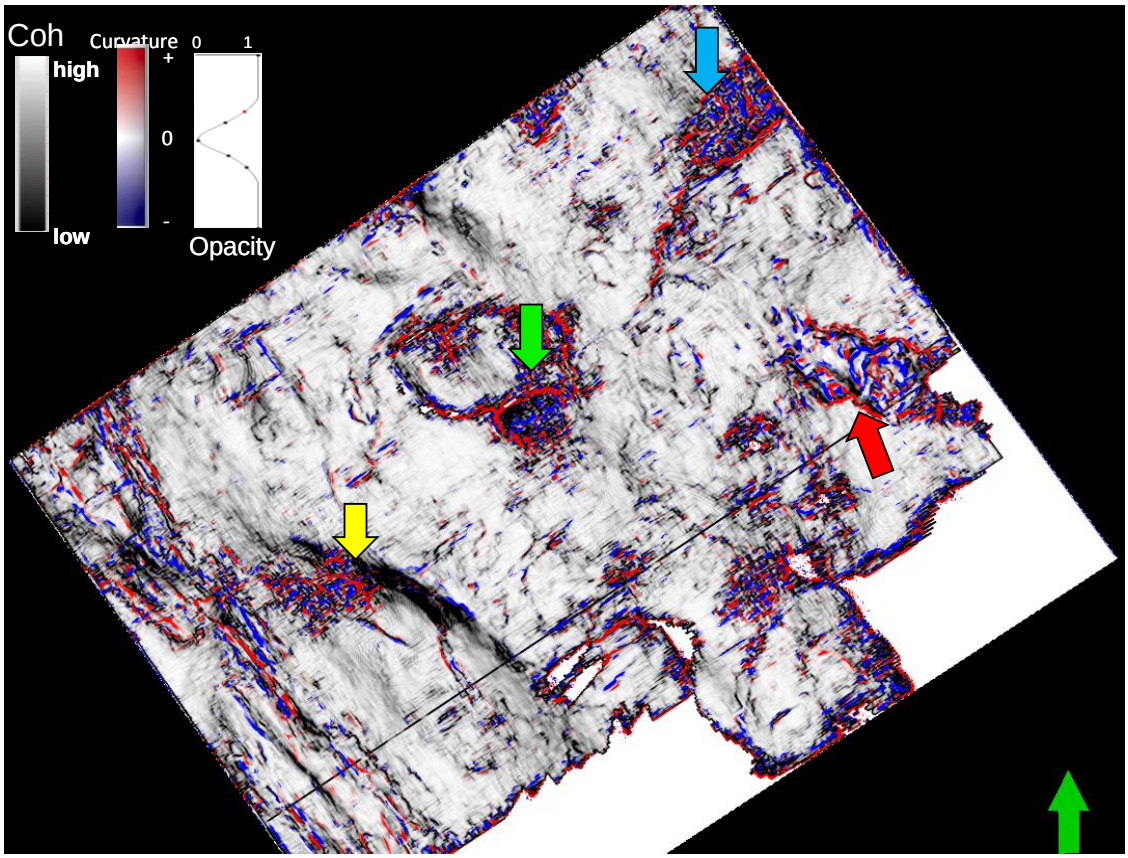

Figure 4.7 *Co-rendered image using transparency of a timeslice at t=1335 ms through K_1, K_2, and curvatures coherence attribute. Yellow, green, and blue arrows indicate chaotic zones due to shallower igneous bodies. Red arrow indicates an igneous body cut by the timeslice.*

Chapter 5: Correlation of Extrusive and Intrusive Igneous Bodies to Magnetic Data

Potential field anomalies generally contain a wide range of signals from various sources and depths. Short wavelength anomalies typically reflect shallow features while lager and broader anomalies are often indicative of deeper, regional sources allowing anomalies of interest to be separated. Potential field enhancement and filtering techniques are designed to better image and delineate both regional scale anomalies associated with Precambrian structures and local anomalies of interest, which cannot easily be in raw data (Elebiju, 2009).

A typical potential field data enhancement and filtering workflow will include residual anomaly separation, upward continuation processing, reduction to the pole or reduction to the equator, pseudogravity transformation, horizontal gradient magnitude, tilt derivative and horizontal derivative of the tilt derivative, analytical signal, first and second vertical derivatives, and directional filtering.

Potential field enhancement and filtering products derived are similar to seismic attributes (Verduzco et al., 2004) and can often help with geological interpretation. However, seismic attributes and filtered potential field data often target different ranges of anomaly wavelengths. These products facilitate the ability to relate physical properties associated with potential field data with geological features of interest (Elebiju, 2009).

Most volcanics have a strong, distinct pattern. However, since volcanics cool slowly through the Curie point, they also acquire a strong remanent magnetization. The magnetic response is the vector sum of the induced magnetization, which is a function on the inclination of Earth's magnetic field at the present time, and the remanent

magnetization, which is a function of the inclination of Earth's magnetic field at the time of magmatic cooling. Figure 5.1a is a shaded relief map of the Amatitlán survey area. The topography ranges from near sea level in the east to 600 m within the survey. Arrows indicate volcanic cones and what appears to be an elongate ridge which falls within the survey. Figure 5.1b is a total magnetic intensity map that has been reduced to the pole to correct for the weak inclination at this latitude. As a processing step, the data have been upward continued to produce a long-wavelength approximation of the data, and then subtracted from the original data. This 'shallow response' image suffers from less Gibb's artifacts than if the data were high-pass filtered. I note that two of the volcanic structures (a ridge which may be a dike, as well as a cone) have a positive magnetic response. The volcanic cone indicated by the blue arrow has a negative magnetic response, suggesting remnant magnetization aligned with a magnetic pole reversal similar to that found in Picuri, New Mexico, USA, by Grauch and Keller (2004) (Figure 5.2). The large cones indicated by the yellow arrows do not correspond to a simple magnetic anomaly, suggesting that there are deeper sills contributing to the total response. In order to better correlate the surface topography to the total magnetic intensity I blended the two images (first converting the topography image to a gray scale) in Figure 5.3.

The overall fold of the seismic survey ranges between 30 and 40 although I noted that an anomalous ring-shaped low-fold area is associated with lower elevation areas (Figure 5.4). In general, low fold results in lower signal-to-noise ratios, which in turn gives rise to the lower seismic coherence anomalies seen in Figures 5.5. By blending the shaded relief topography map shown in Figure 5.1a with the seismic coherence image (Figure 5.6a) and the magnetic intensity map (Figure 5.6b) I interpret other low

coherence areas as being due to shallow volcanics (the yellow, green, and cyan arrows corresponding to those on the vertical slices in Figure 1.2). The orange arrow indicates a low coherence area corresponding to two overlying volcanic sills, which are displayed on vertical seismic in Figure 5.7.

Figure 5.8 shows a suite of shallow sills in the shallow section of the seismic data. I noted in Figure 5.8b that the sill indicated by the yellow arrow starts at depth, jumps to a higher level perhaps through a dike, and continues horizontally across, repeating this pattern at least three times. This nearly horizontal intrusion pattern does not seem to adversely affect the deeper seismic data quality.

Igneous sills where extracted from the seismic data as Geobodies (Figure 5.9), and in Figure 5.10, I display a time-structure map of the larger extracted igneous sills in the survey. By blending this map with the coherence image at t=1.335 s I see a direct correlation between the location of some of the volcanic sills and the seismic data quality (incoherent zones) deeper in the section.

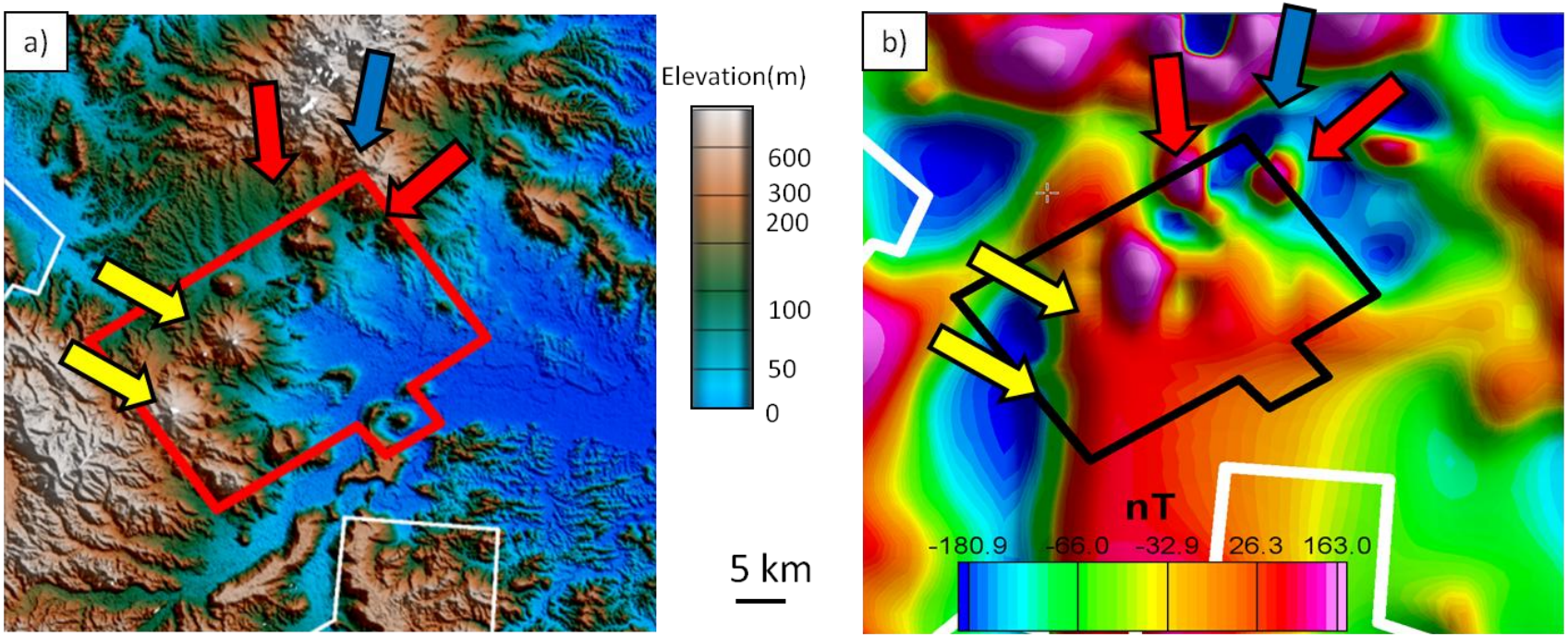

Figure 5.1 *(a) Topographic map with the Amatilán seismic survey outlined in red. Arrows indicate volcanoes and a possible dike. White outlines indicate limits of municipalities. (b) Total Magnetic Intensity (TMI) map of the same area filtered to enhance shallow magnetic anomalies (survey outlined in black). The blue arrow indicates a negative and the red arrows indicate a positive magnetic anomalies. The signature of the volcanoes, indicated by yellow arrows, is more complex, suggesting buried magnetic sources. (Topography data from http://seamless.usgs.gov/website/seamless/viewer.htm. TMI data from ftp://ext.usgs.gov/pub/cr/co/denver/musette/pub/open-file-reports/ofr-02-0414)*

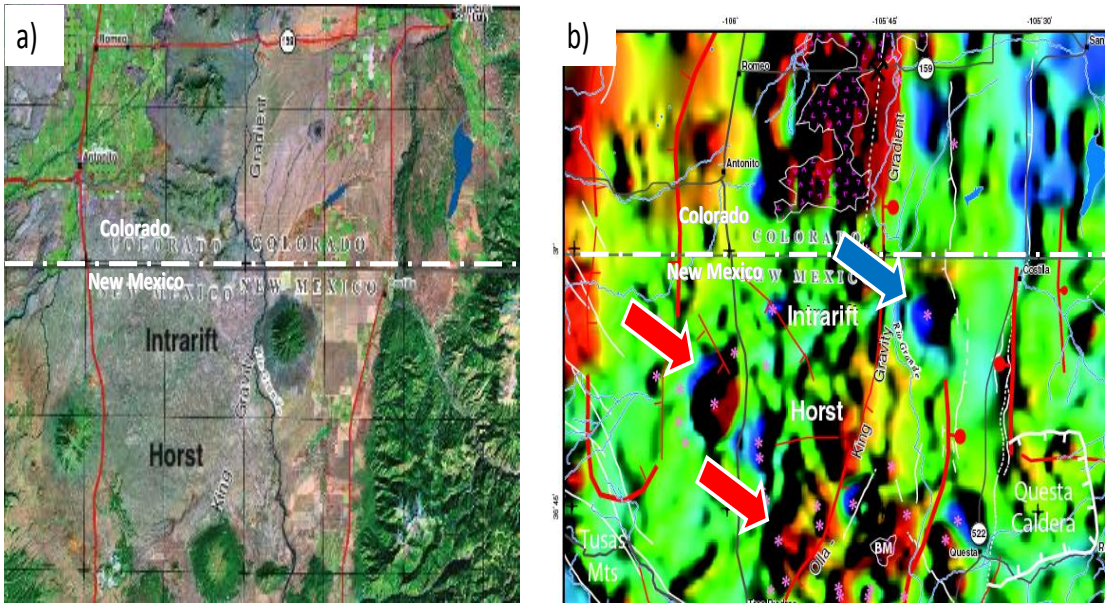

Figure 5.2 *(a) Thematic mapper image and (b) Total magnetic intensity map over the Picuri area of New Mexico, U.S.A. Red arrows indicates volcanic cones that has a positive response, while blue arrow indicates one that has a strong negative response. This negative response is due to remnant magnetization locked in during a magnetic polar reversal. (After Grauch and Keller, 2004).*

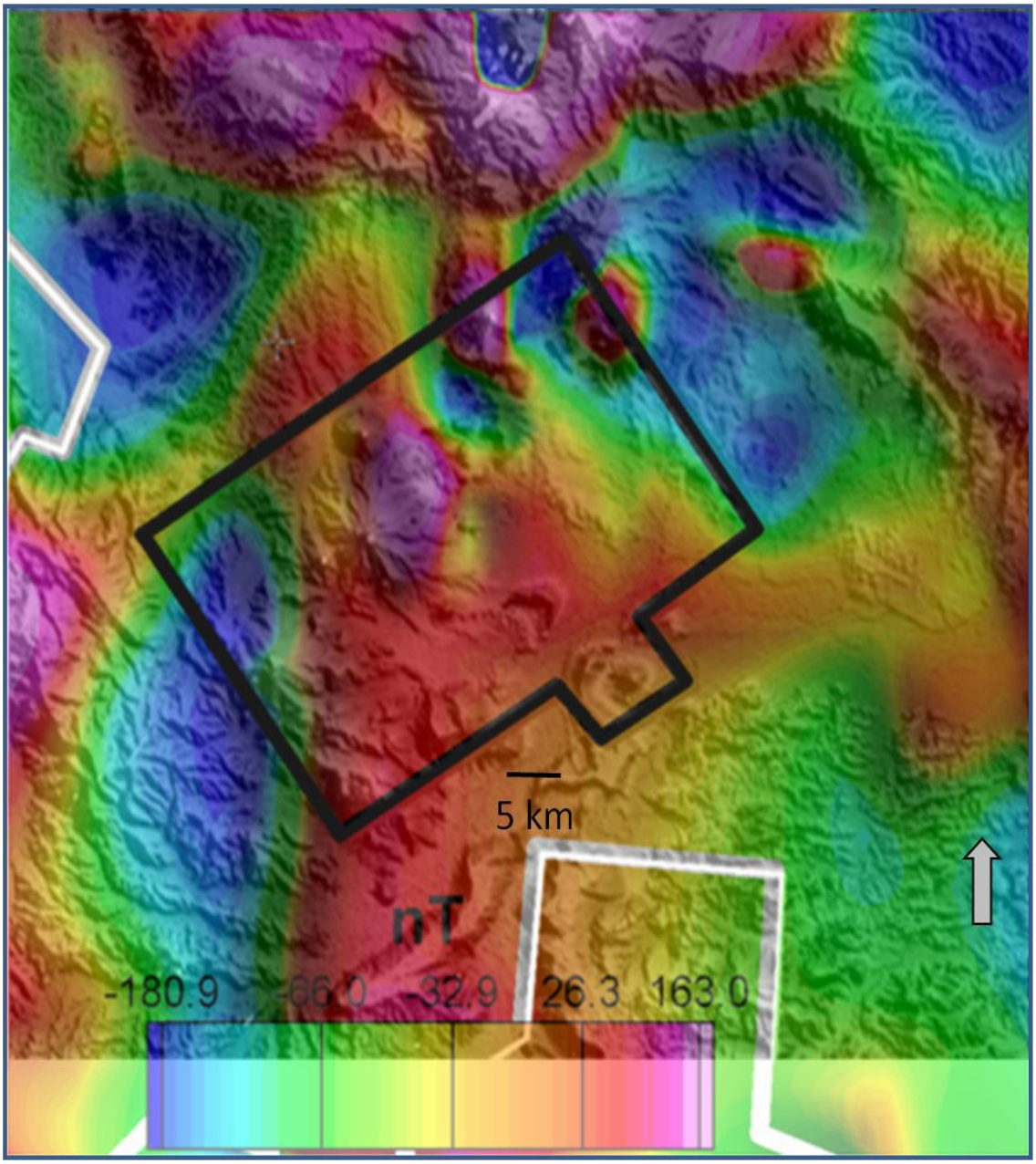

Figure 5.3. *Blended image of Total magnetic intensity with relief topographic map (TMI) map and topography plotted against a gray scale. (Topography data from http://seamless.usgs.gov/website/seamless/viewer.htm . TMI data from ftp://ftpext.usgs.gov/pub/cr/co/denver/musette/pub/open-file-reports/ofr-02-0414)*

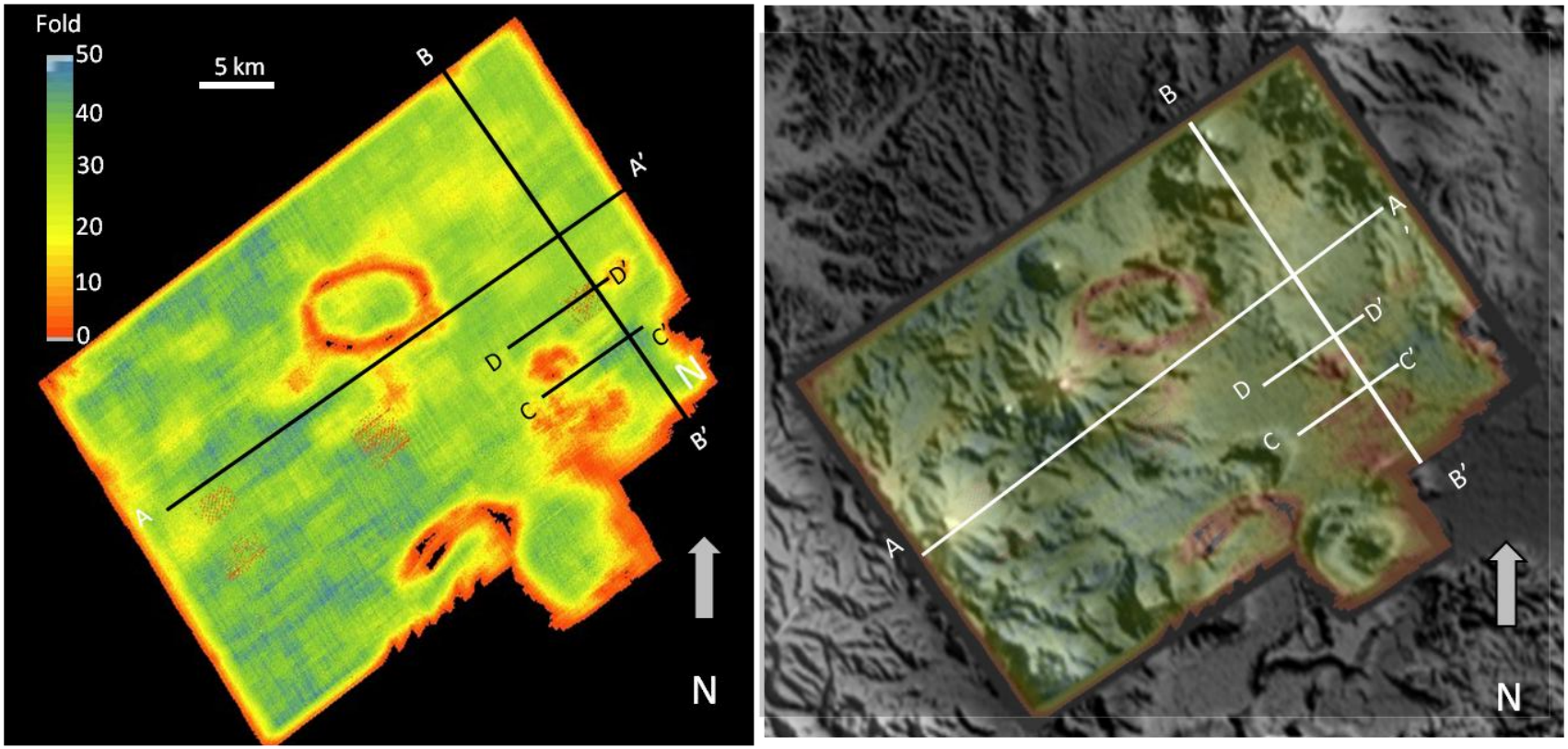

Figure 5.4. *(a) Fold map for the Amatitlán seismic survey. (b) Fold map blended with the topography. Low fold areas are not associated with the prominent volcanoes, but rather with lower elevation, swampy areas.*

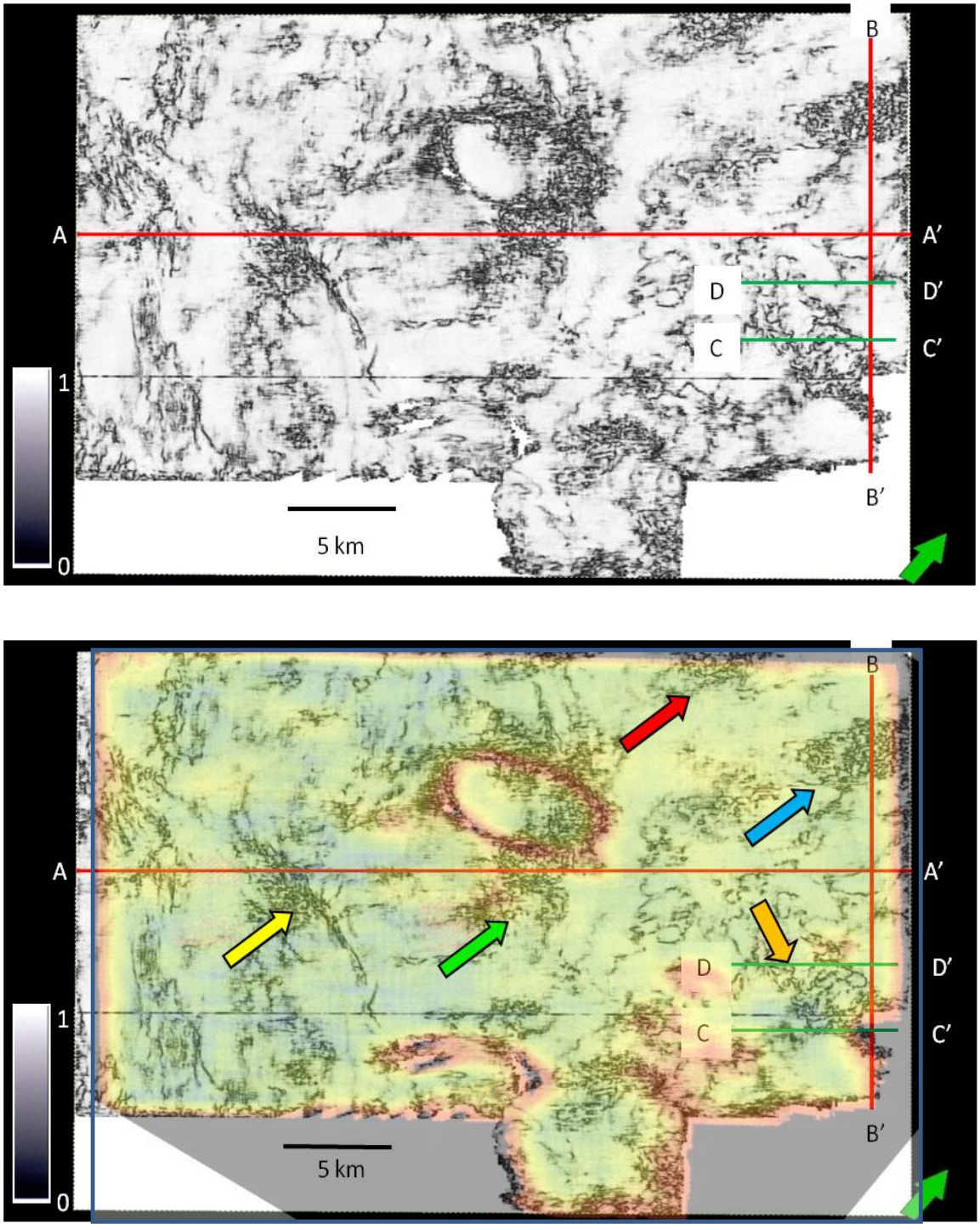

Figure 5.5. *(a) Time slice at t = 1.335 s through a coherence volume computed from the improved processing flow, and (b) blended with the seismic common midpoint fold map.*

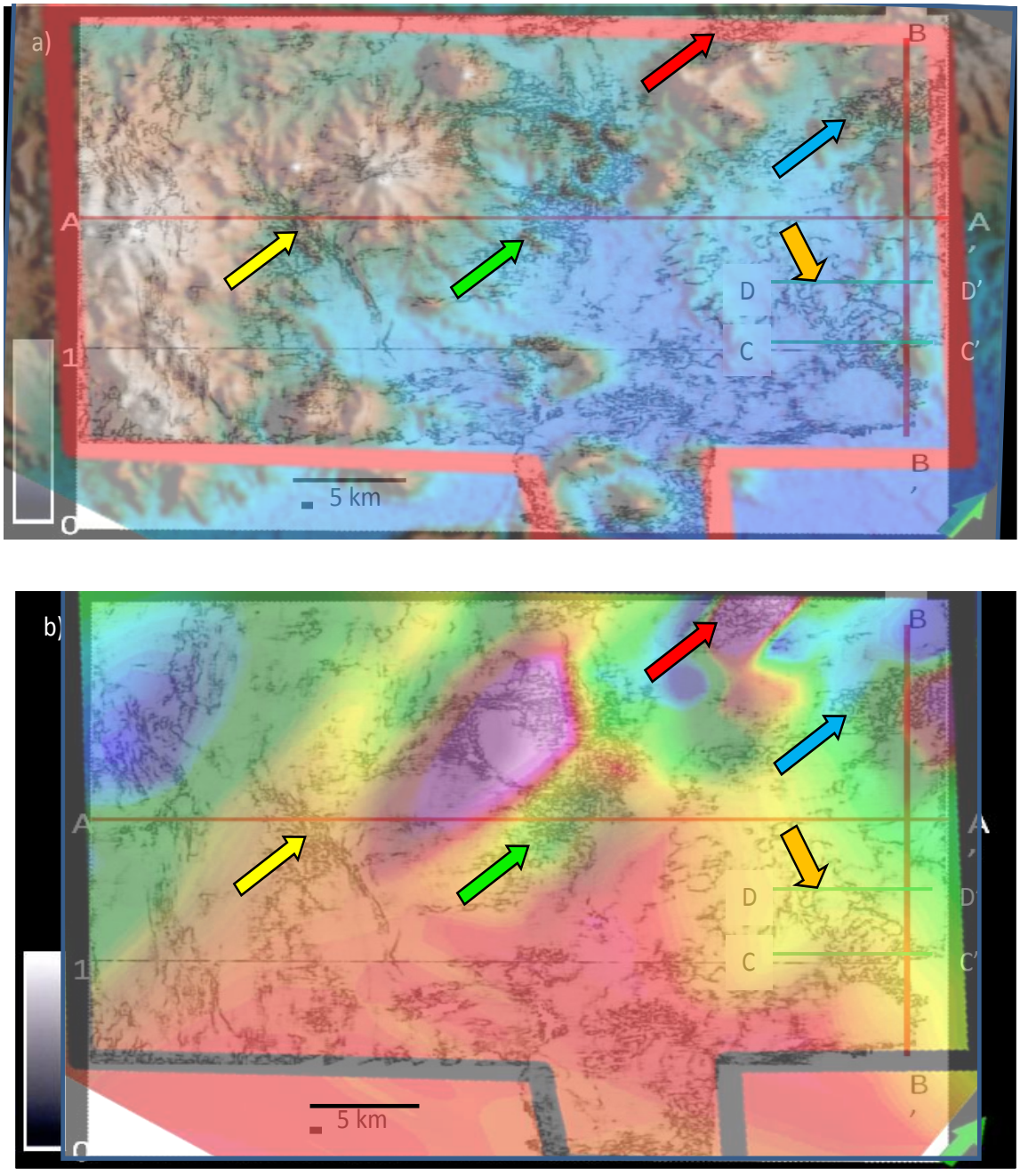

Figure 5.6. *Time slice at t = 1.335 s through a coherence volume (a) blended with the topography map, and (b) blended with the RTP total magnetic intensity map.*

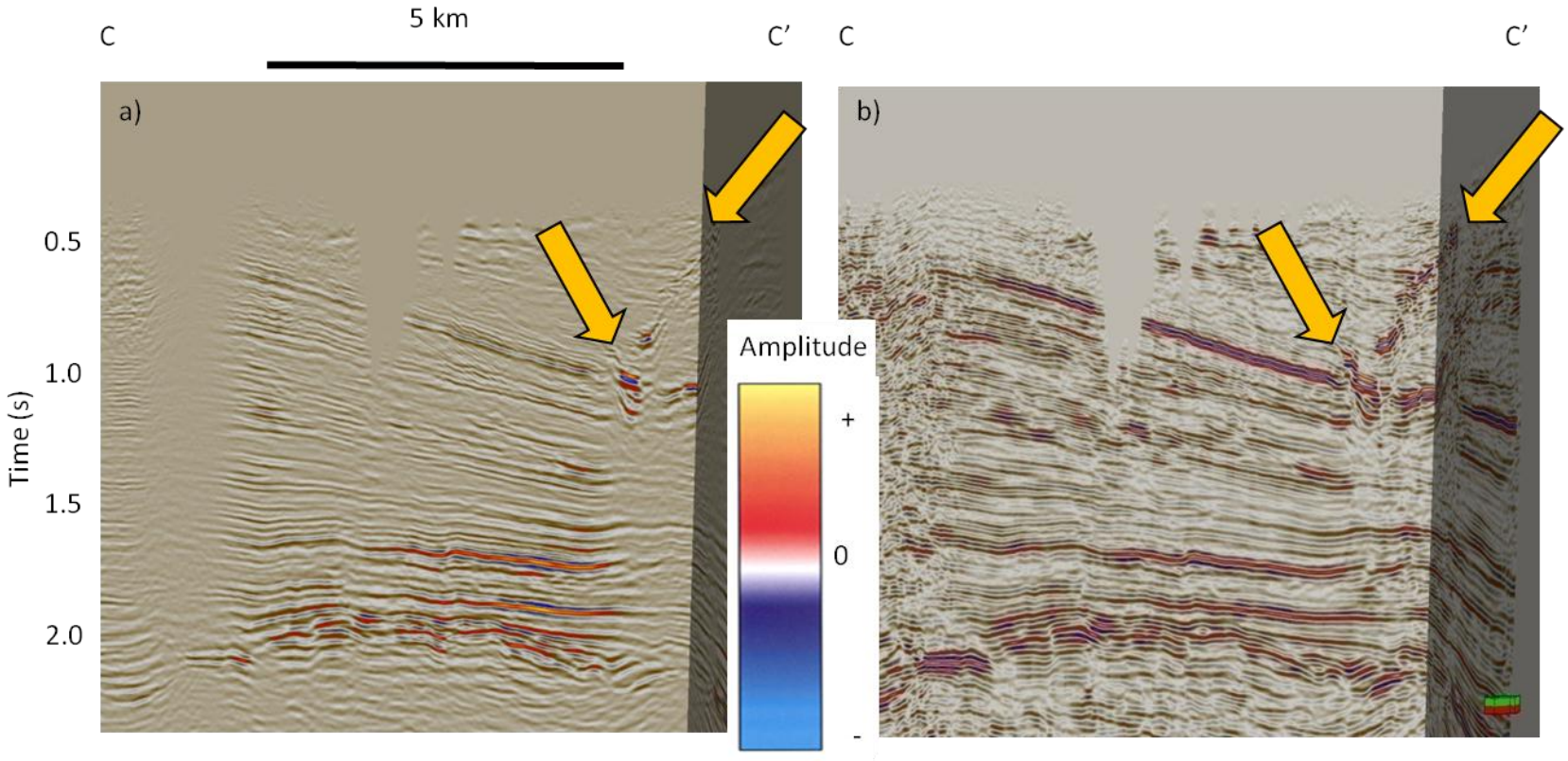

Figure 5.7. *Seismic expression of two stacked igneous intrusive sills for the (a) and (b) reprocessed data. Notice the lower amplitude below the volcanic sills indicated by the orange arrows has been better balanced while interbed multiples have been better attenuated. Location of lines shown in Figure 5.4a.*

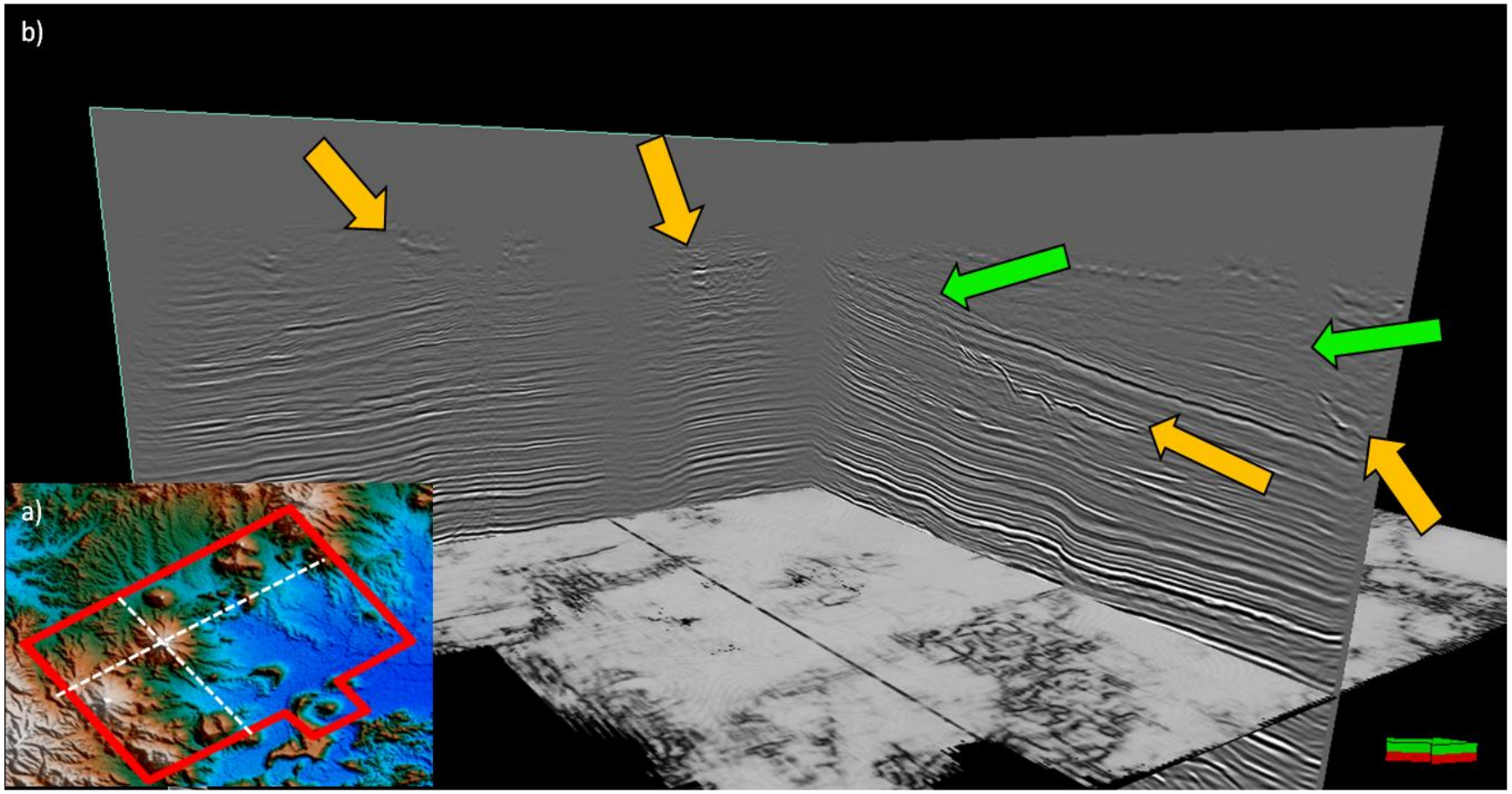

Figure 5.8. *(a) Location of two vertical seismic lines crossing beneath the largest volcanic cone. (b) The two seismic lines shown in (a), along with the coherence time slice at t=1.335 s. Orange arrows indicate volcanic sills. Green arrows indicate mounds that we interpret to be volcanoclastic buildups*

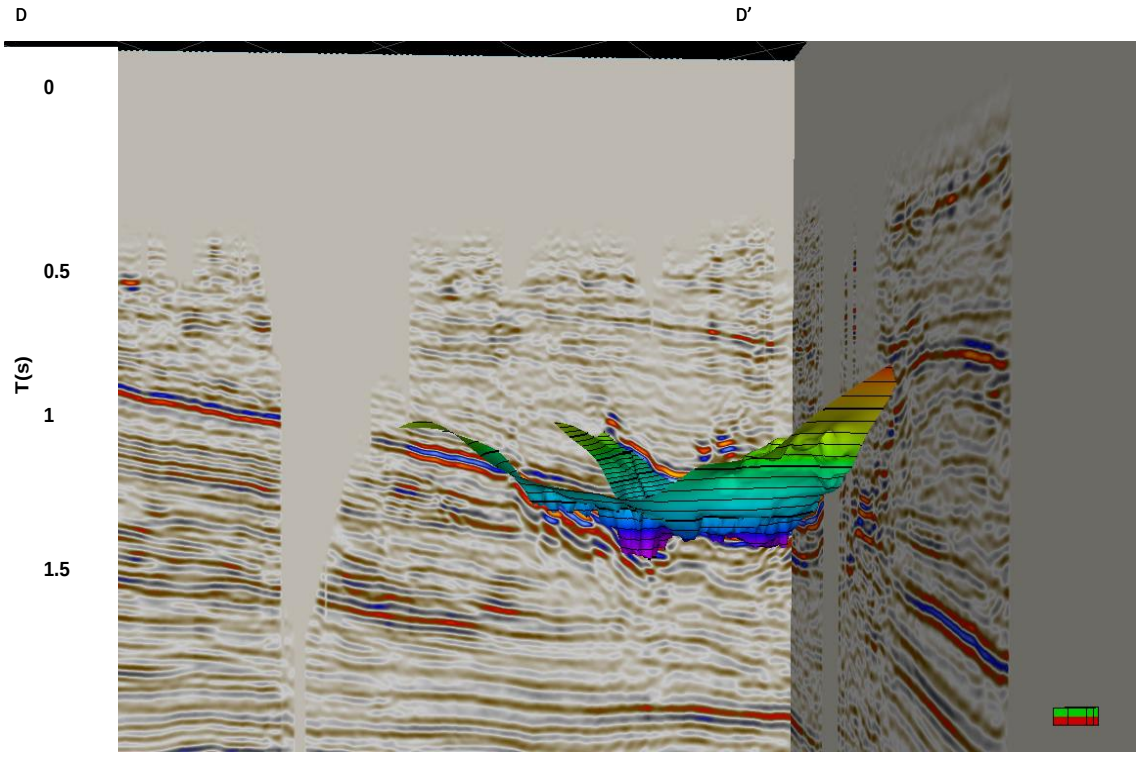

Figure 5.9. *Seismic line displaying the extraction of one igneous sill as a geobody.*

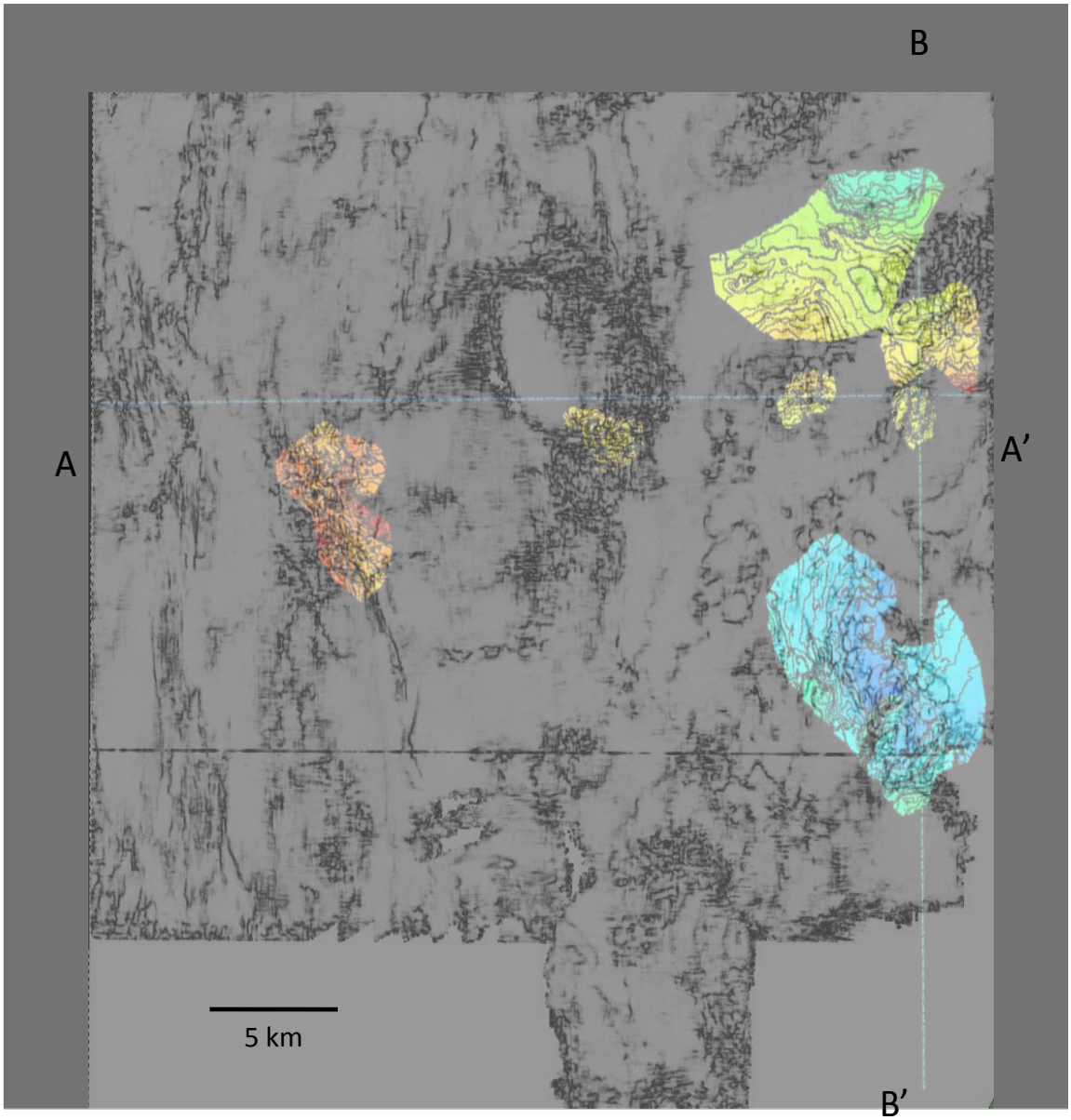

Figure 5.10. *Blended image of the time structure map with the coherence image at t=1.335 s. Note the correlation between the location of some of the volcanic sills and the data quality (incoherent zones) deeper in the section.*

Chapter 6: Seismic Modeling of Igneous Sills

To better understand the effect of shallow intrusive on the deeper reservoir objectives, I generated numerical models of a representative vertical section of the Amatitlán survey using both asymptotic ray tracing and finite-difference solutions of the elastic wave equations. The model was constructed from picked horizons and well logs from the survey and augmented by values extracted from the rock physics literature. P-velocities, S-velocities, and density were assigned to layers of intrusive and extrusive igneous bodies, sand, and shale. The source/receiver offsets and separation were similar to those used for the Amatitlán survey (Figure 6.1). For this model I assumed my igneous intrusion pattern was similar to those by Davies et al. (2004) in their North Sea case study (Figure 6.2). The sill distribution is complex with numerous discordant and compound sills being modeled.

6.1 Ray Trace Modeling

Ray tracing modeling provides a fast and efficient means of computing ray-paths and travel times from sources and receivers to any target horizon of interest and is commonly used in subsurface illumination studies as part of the acquisition design process. I used a commercial algorithm that solves the Eikonal equation with a finite-difference method. Each layer is assigned P-velocities, S-velocities, and densities. My primary objective in using the ray trace model was to observe the ray path's behavior as they traveled through the intrusive and extrusive igneous bodies.

Figure 6.3 shows the extent of the diffraction that occurred as the rays went through the upper intrusive igneous body (marked in purple). Figure 6.4 shows the ray

behavior as they traveled through the extrusive igneous body (marked in blue) and lower intrusive igneous body (marked in purple). Finally, Figure 6.5 is a stacked section from the ray tracing model showing a discontinuous, broken, target horizon (red arrow).

6.2 Acoustic Modeling

Finite difference solution of the scalar wave equation provides accurate estimates P-wave reflections, diffractions and headwaves events resulting in accurate arrival times suitable for structural modeling. Since elastic effects (such as mode conversions and polarizations) are ignored, the amplitude calculation is only approximate. The solution to the two-way equation includes multiples in the simulated wavefield, thereby allowing me to observe the scattering and interference effects of the high-impedance intrusive and extrusive igneous bodies.

Figure 6.6 shows a sequence of snap shots from a source located in the middle of the model. Some of the more relevant features include a strong reflection from the extrusive body (red arrow), a diffraction due to the igneous intrusive (yellow arrow), lack of energy from a deeper reflector (blue arrow), the large amount of multiples (orange arrows), and the poorly transmitted energy of the direct wave after going through the intrusive igneous body (green arrow).

Reflections from Figure 6.7 show the corresponding a shot gather for this location where it is easy to identify the intrusive and extrusive igneous bodies (red arrows). Since this is a two-way acoustic simulation, the modeled gather contains not only primary but also multiples (yellow arrows).

After stacking the data using pre stack Kirchhoff depth migration (Figure 6.8), I was able to observe that those areas below the shallow intrusive igneous bodies (yellow arrow) were poorly resolved, creating false discontinuities in the horizons. The presence of multiples created additional artifacts throughout the seismic model (red arrows).

6.3 Elastic Modeling

The technique used for my elastic modeling was based on the finite-difference method. The finite-difference algorithm used for the elastic modeling describes the P- and S-wave propagation and is suitable for detailed stratigraphic modeling in which amplitude has the same importance as travel time. As with the acoustic model, the elastic model was based on a two-way equation, which allowed for the multiples in the simulation wavefield to be included. The elastic model is 2D framework and the acquisition a suite of 61 commons shot gathers with each shot point having 81 receivers 50 m apart.

Figure 6.9 shows a representative snapshot of the elastic model. Note that as the direct wave propagates through the igneous instrusives, that it loses its simple form and becomes a suite of complex diffractions followed by a train of interbed multiples. Such a broken direct wave can not be approximated by a relatively smooth prestack migration velocity depth model. While there is considerable energy propagating through the igneous intrusive, this energy will not be properly focused without putting in a very detailed igneous intrusive velocity model.

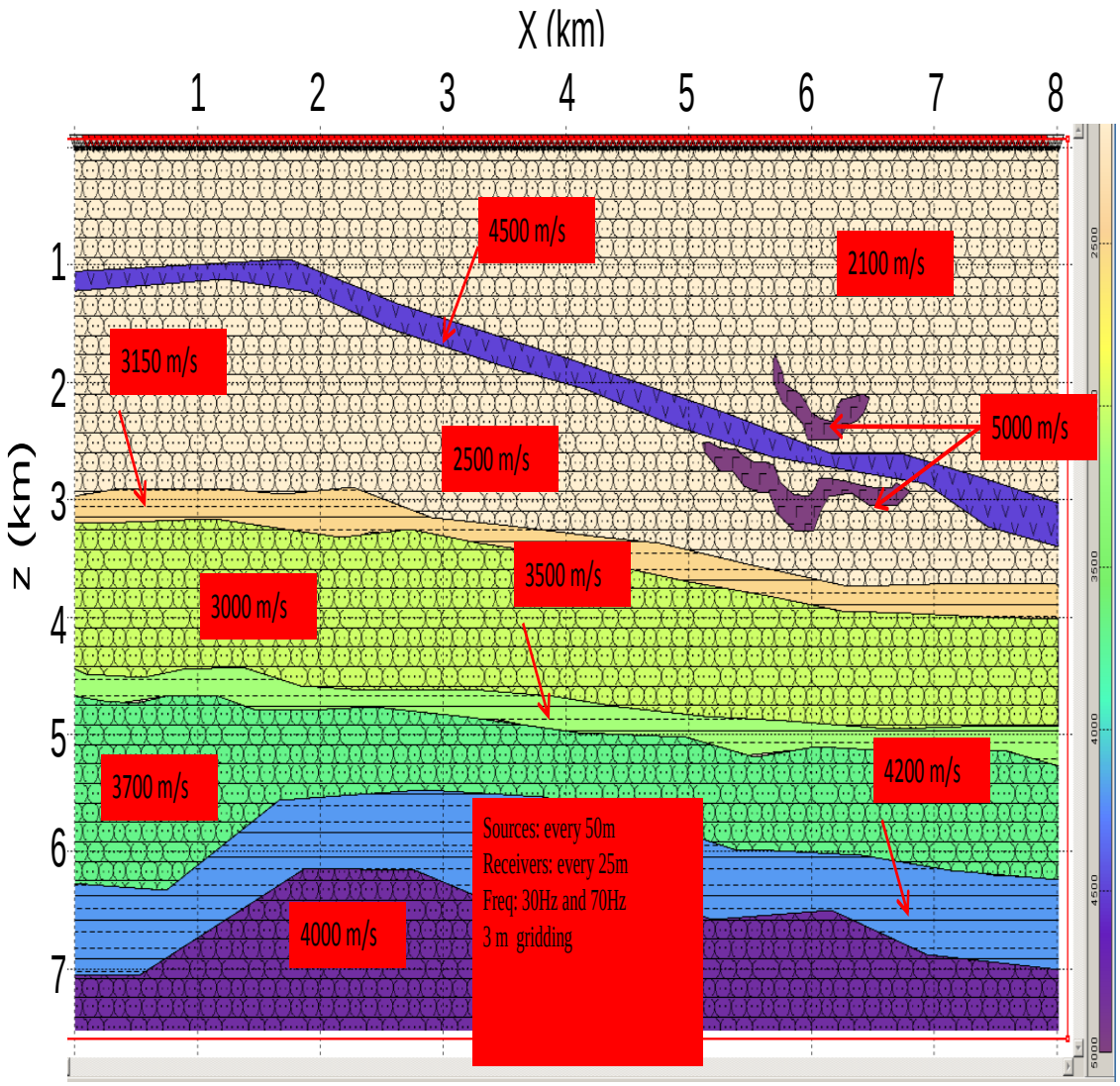

Figure 6.1 *Model extracted from the Amatitlan Survey with the presence of igneous intrusives (upper purple body) and extrusive (dark blue body).*

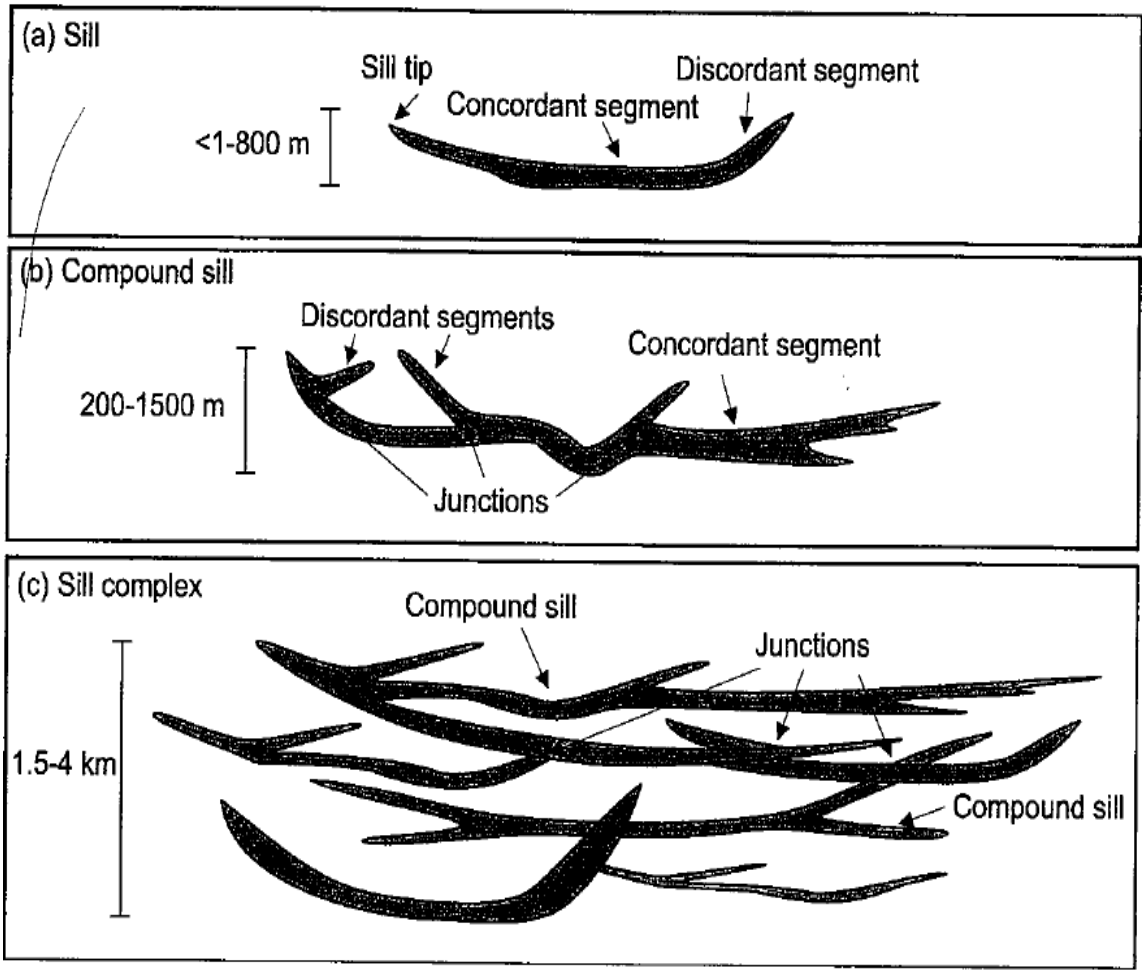

Figure 6.2 *Schematic cross-sections illustrating different levels of the three-dimensional geometrical complexity of igneous bodies recognized on 3D seismic data: a) Sill, b) Compound sill, and c) Sill complex (After Davies et al. 2004).*

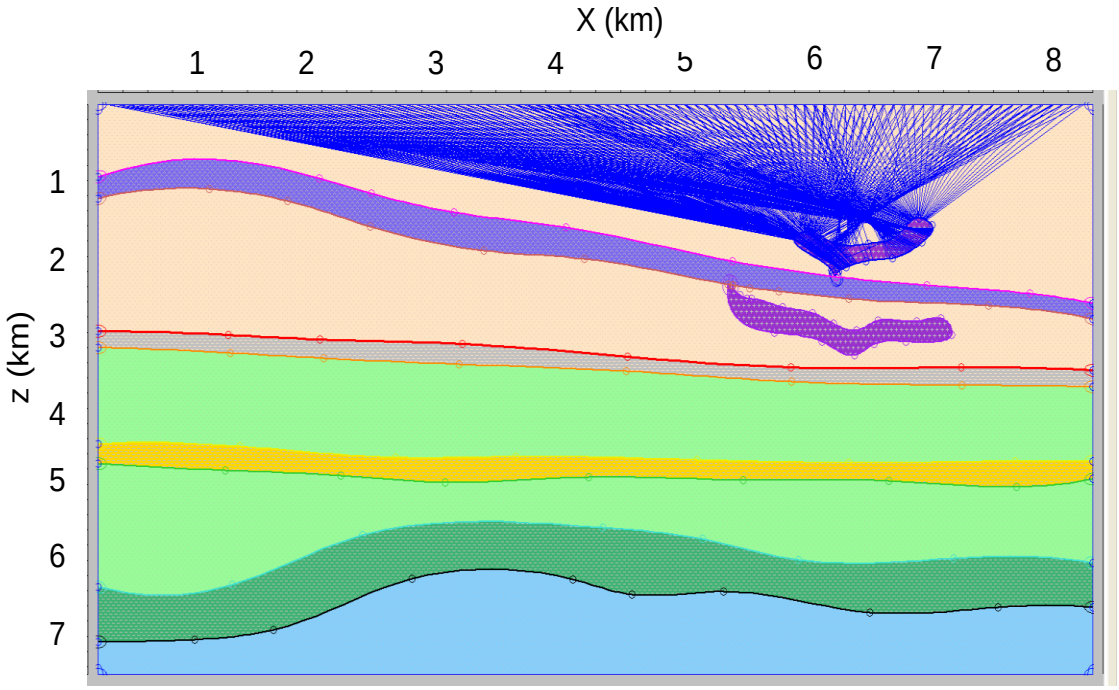

Figure 6.3 *Ray trace model of the Amatitlán survey showing rays that illuminate the upper and lower boundaries of one of the igneous intrusive bodies.*

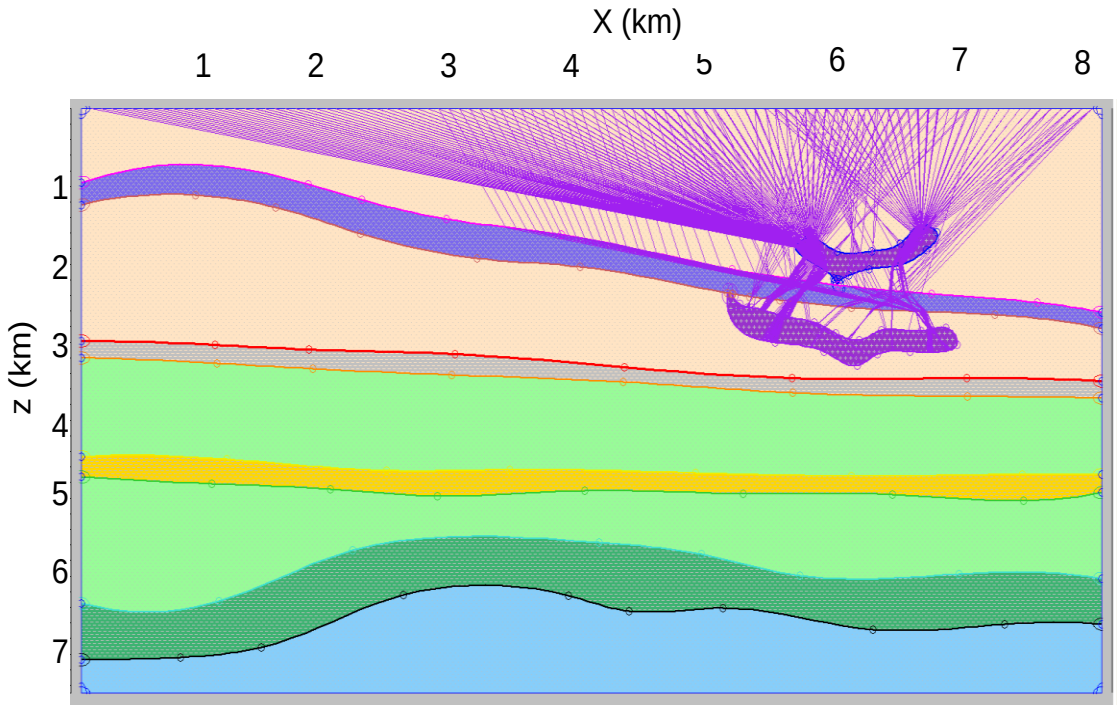

Figure 6.4 *Ray trace model of the Amatitáln survey showing rays that illuminate the upper and lower boundaries of lower igneous intrusive body.*

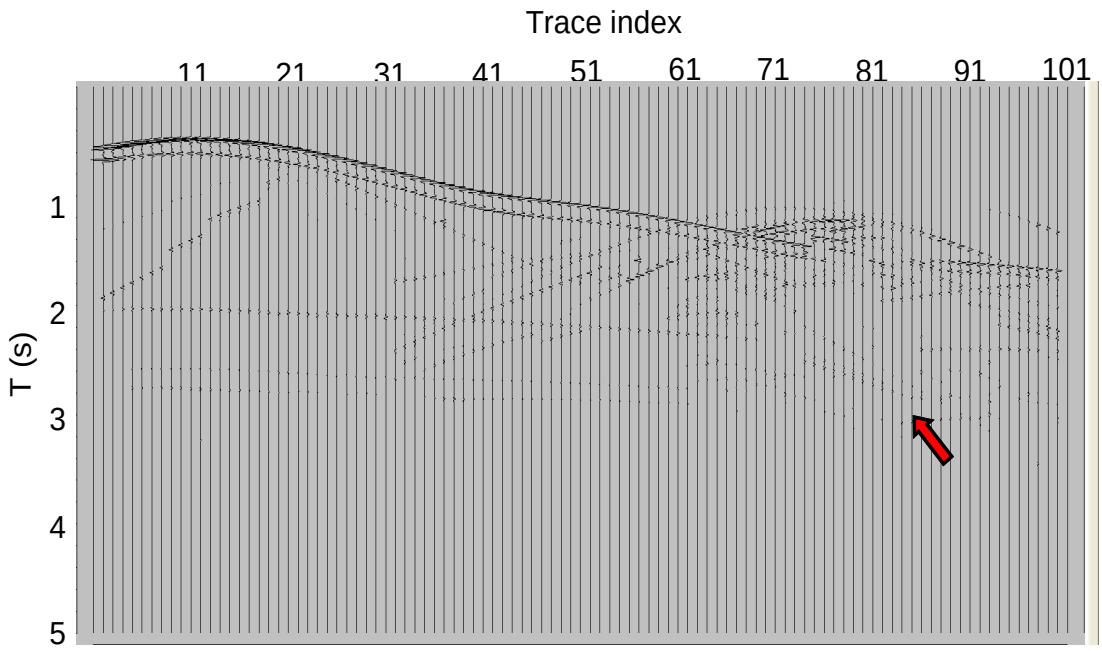

Figure 6.5 *Stack section from the ray tracing model. Note the discontinuity in the horizons below the igneous intrusive.*

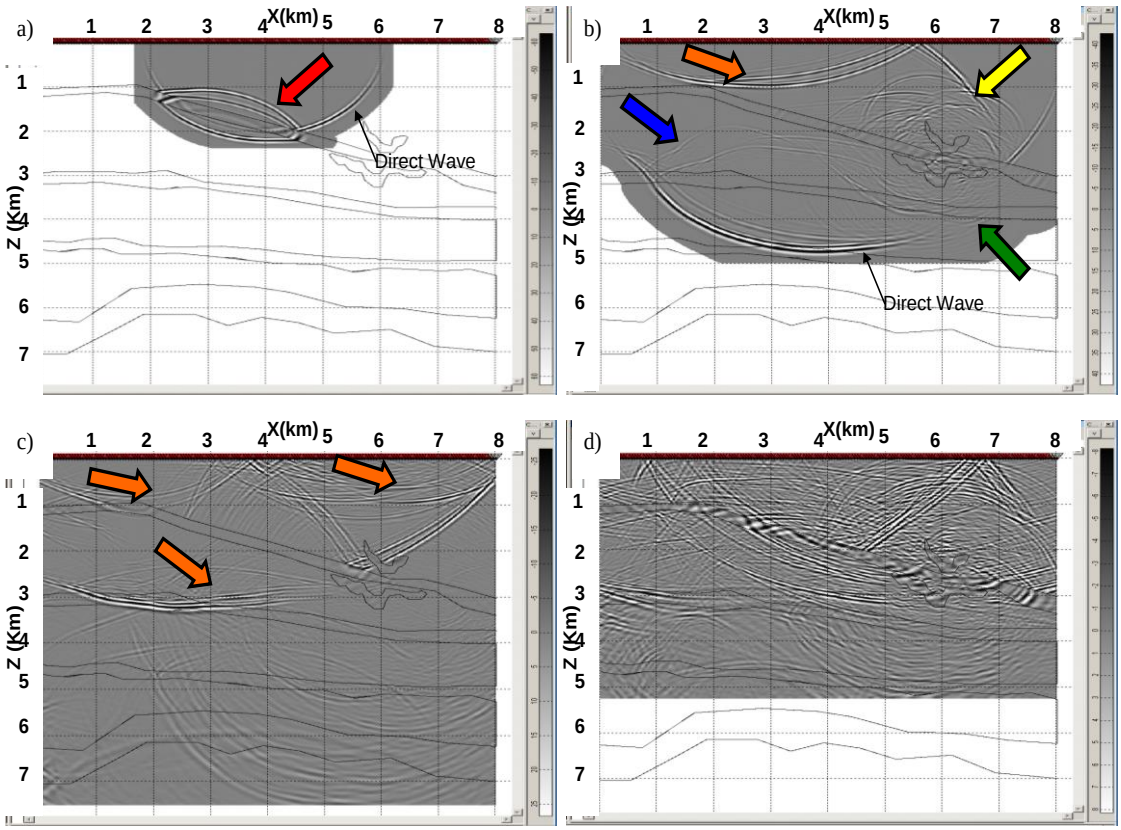

Figure 6.6 *Snap shots at (a) t=0.2 s, (b) t=0.4 s, (c) t=0.6 s, and (d) t=0.8 s for a shot location indicated by the star. every 0.2 s displaying the strong reflection from the extrusive body (red arrow), the diffraction due to the intrusive igneous bodies (yellow arrow), the lack of energy from deeper reflector (blue arrow), the large amounts of multiples (orange arrows), and the poorly transmitted energy of the head wave after going through the intrusive igneous bodies (green arrow) .*

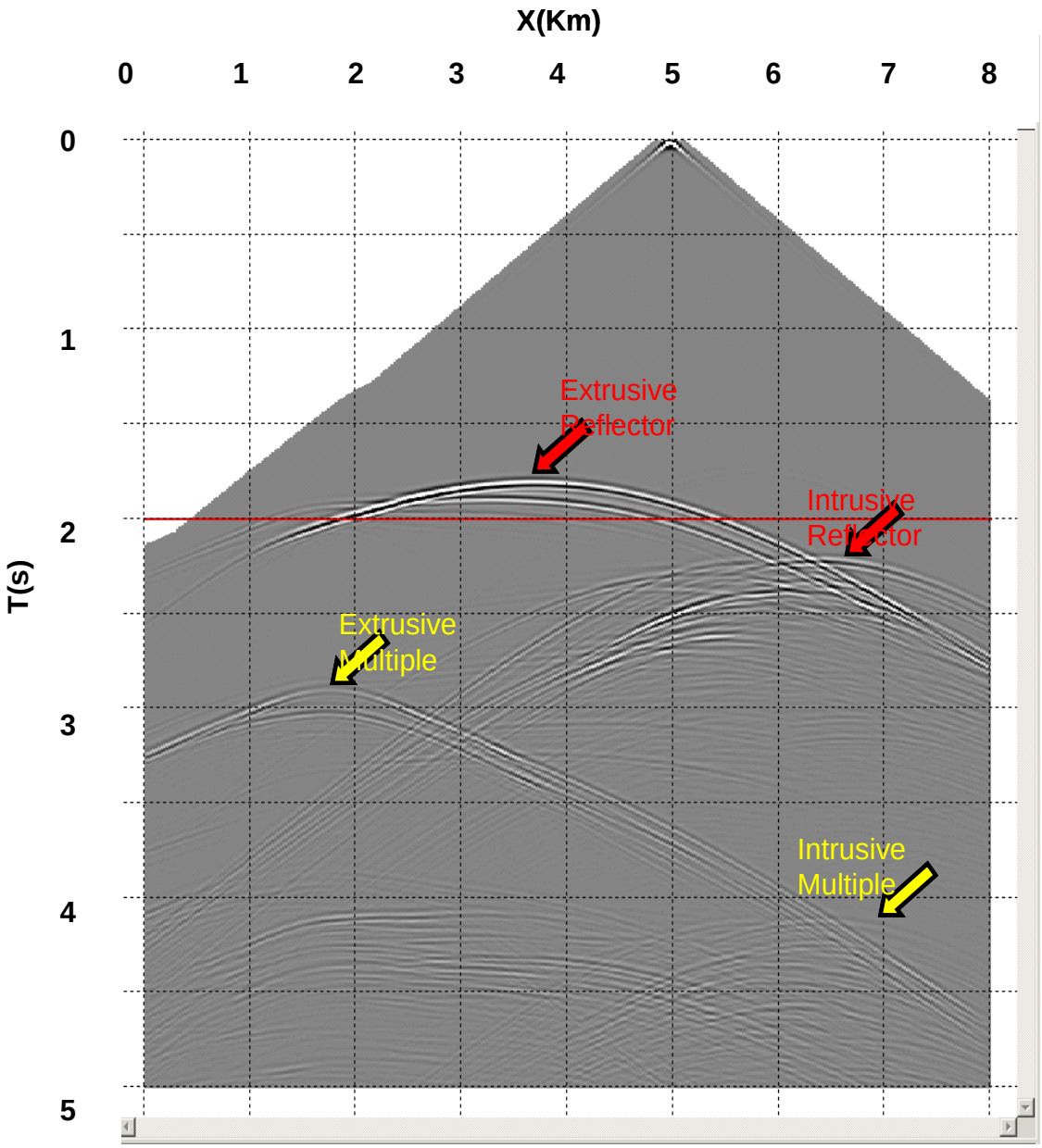

Figure 6.7 *Synthetic common shot gather corresponding to the snap shots displayed in Figure 6.6. Note the strength of the the igneous intrusive and extrusive reflections (red arrows). As this is a two-way acoustic simulation, the modeled gather contains not only primary but also long period surface-related multiples (yellow arrows) as well as shorter period interbed multiples (green arrows).*

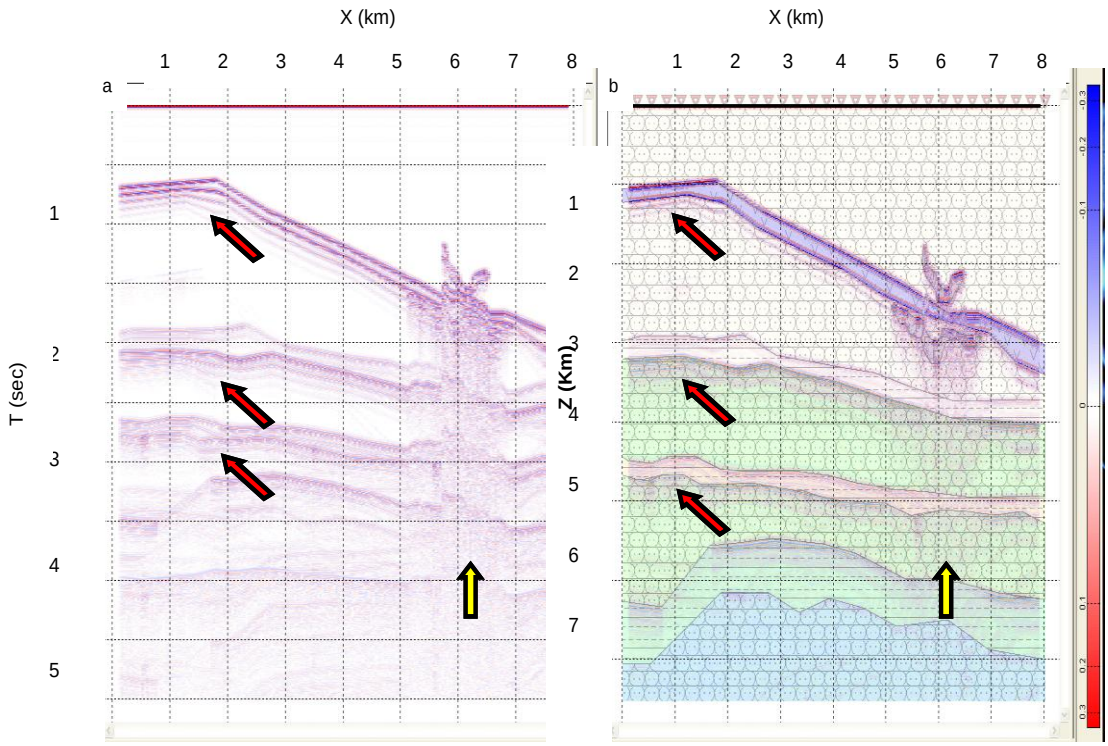

Figure 6.8 *a) Stack obtained after pre-stack Kirchhoff depth migration of a suite of 91 common shot gathers represented by the one in Figure 6.7. b) Original model blended with stack using depth pre-stack Kirchhoff migration model. Shallow intrusive igneous bodies (yellow arrow) were poorly resolved, creating false discontinuities in the deeper horizons that will result in low-coherence anomalies. Multiples create artifacts throughout the seismic model (red arrows).*

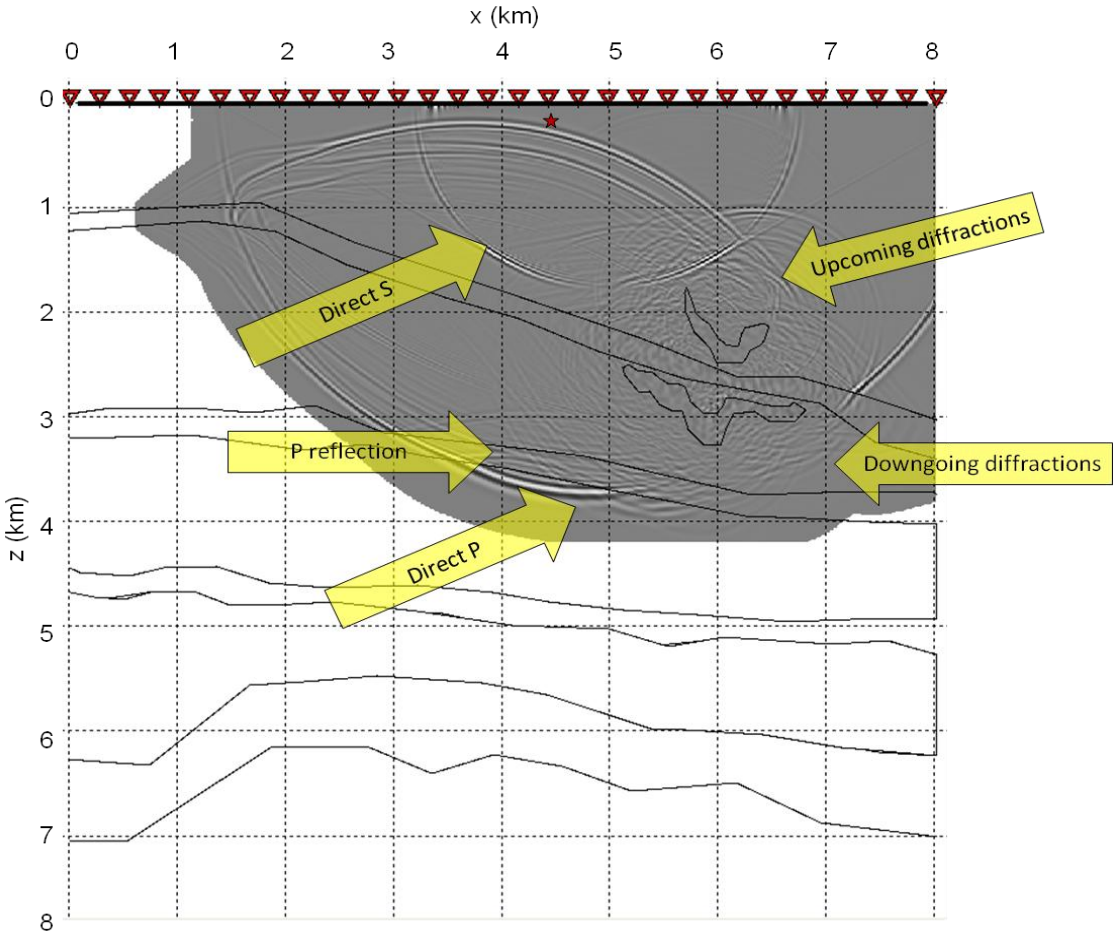

Figure 6.9 Representative s*napshot at t=0.6 s of the vertical component of particle velocity from a finite difference elastic modeling for a source location represented by the red star. The top of the igneous intrusive will be well imaged since the upcoming diffractions are traveling through a relatively smooth background velocity model. Note that the direct P-wave necessary to illuminate the deeper target reflectors is a simple coherent event to the left of the igneous intrusive. In contrast, below the igneous intrusives, we no longer have a single direct P-wave event, but rather a complex suite of downgoing diffractions. While considerable energy penetrates through the intrusives, it is so broken up that it will not be accurately imaged using a smooth background velocity model.*

Chapter 7: Seismic Processing

The data were originally acquired and processed in 2003 using a well-established acquisition and processing workflow that had proven effective in other areas of Veracruz State. However, the Amatitlán survey was both more expensive and more difficult to acquire than most other surveys. Some of the acquisition parameters included:

Source type	Dynamite
Bin size	25x25 m
Receiver interval	50 m
Source interval	50 m
Nominal Fold	36
Receiver line interval	250 m
Source line interval	350 m
No. Active lines per shot	12
No. Channels per line	84
No. Active Channels per shot	1008
Recording time	6 s
Sampling interval	2 ms

Table 7.1 *Acquisition parameters used in the Amatitlán survey.*

In addition to rugged topography, dense forestation, human settlements, and sensitive archaeological sites, there appeared to be strong impedance anomalies in the shallow section that generated amplitude shadows deeper in the section. For this reason, the Amatitlán survey was reprocessed in 2007 with the objective of obtaining better shallow imaging.

7.1 Previous Work

The reprocessing work in 2007 was done by PEMEX Exploration and Production. After the pre-stack data were received, read, and verified, the 2007 PEMEX Exploration and Production in-house processing team designed an amplitude-friendly workflow. Processing steps were used to attenuate low frequency noise and spikes within the seismic traces. Careful deconvolution was performed to detect and filter out some of the reverberations, multiples and ghosts. Refraction statics were calculated and velocity analysis was performed for the CMP gathers. Coherent noise suppression workflow was applied with the specific goal of attenuating coherent shot-generated noise. Amplitude compensation was run to obtain a better amplitude balance and reduce distortions. Trace mutes, datum corrections, aliased noise suppression, and azimuth moveout was applied prior to Kirchhoff pre-stack time migration.

7.2 Velocity Analysis

One of the more important steps in processing is the velocity analysis. Velocity analysis consists of calculating stacking or NMO velocities from measurements of normal moveout. It also involves finding velocities that give the best fix to flatten the hyperbolic events in the common-midpoint gathers. If the

velocity is too low, after normal moveout correction, common midpointgather will show an under-corrected effect (frowns). If the velocity is too high, after normal moveout correction, the common midpoint gather will have an over-corrected effect (smiles).

Although the 2007 reprocessed data were superior to the original 2003 processing, I wanted to see if I could incrementally improve upon the results. Starting with the prestack time migrated common gathers as shown in table 7.2; I first removed the NMO correction corresponding to the migration velocity analysis. Using the concept of the Deregowski Lopp (1990) I then performed residual velocity analysis with a very detailed analysis on areas where my interpretation of the migrated stack indicated that the velocities would be affected by the overlying igneous bodies. The velocity analysis was performed on a 250 m inline by 175m crossline grid. In the target area, I analyzed every 15th inline, and 10^{th} crossline, with velocity scans ranging from 1000m/s to 7000m/s. In the absence of overlying igneous bodies, the velocity spectrum, appears as well-defined bull-eyes (Figure 7.1). In contrast, beneath the igneous bodies, the velocity spectra are less well defined (Figure 7.2), making an interpretation difficult.

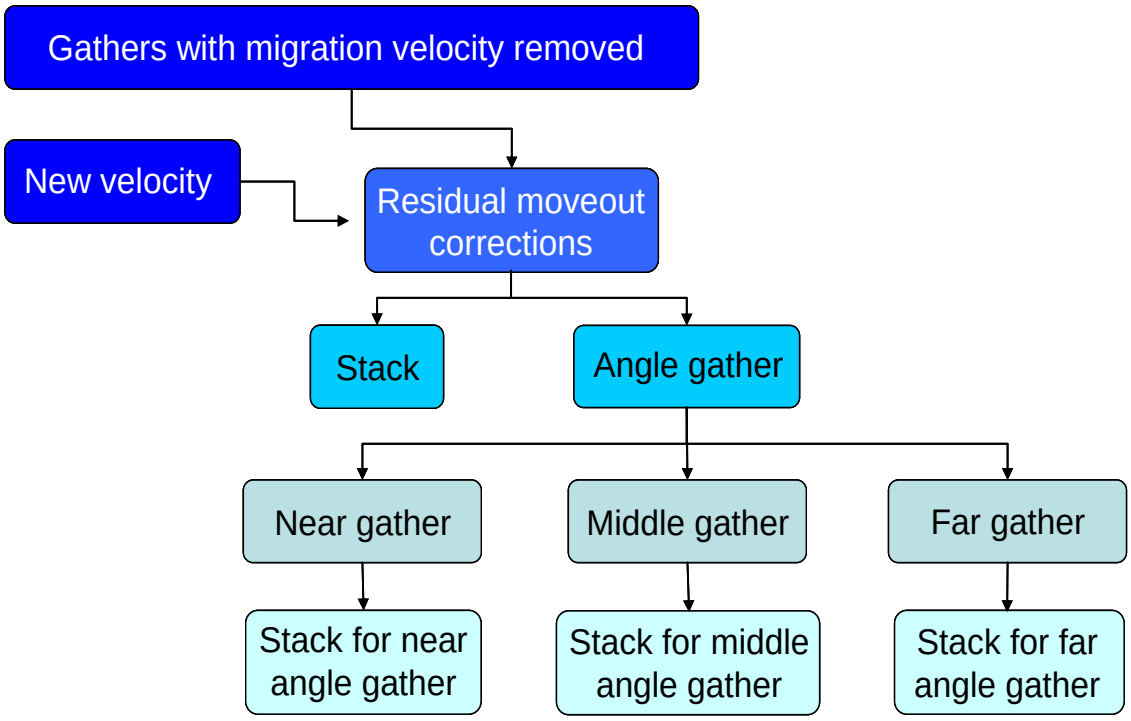

Table 7.2 *Workflow used for the new reprocessing work*

7.3 NMO Correction

After the velocity analysis the next step in residual velocity analysis is to reapply the NMO correction to flatten the common reflection point gathers. In a processing center with sufficient computer resources, the original prestack common shot gathers might be remigrated using this updated velocity. Figure 7.3 shows a representative migrated common reflection point gather correction resulting from the 2007 reprocessing by PEMEX. These gathers are located in areas of high igneous bodies' presence. Note that some of the gathers are under-corrected (yellow arrows). Figure 7.4 shows same gather after application of reverse-NMO using the migration velocity. Figure 7.5 shows the new and

improved NMO correction (with mutes) using velocities picked with the knowledge that there is an overlying igneous intrusive.

Figure 7.7 shows line II' from the 2007 velocity analysis and prestack time migration. Figure 7.8 shows the same line after residual reverse NMO, residual velocity analysis, and NMO have been applied beneath the shallow igneous bodies. Note the increase in vertical and lateral resolution and the more continuous horizon (yellow arrow) due to the noisy areas being removed. Additionally, Figures 7.9 and 7.10 show similarity attributes at t= 1750ms from the 2007 velocity analysis and the new residual velocity analysis respectively. A majority of the incoherence created by the shallow igneous bodies has been removed by the new residual velocity analysis.

7.4 Angle Gathers

Seismic data are acquired with sources and receiver separated by a given offset. Offsets and incident angles (more amenable to AVO and prestack inversion analysis) represent similar information, with a nonlinear relationship between them. With this objective in mind, I reorganized the common offset migrated gather into near (0 to 12 degrees), middle (12 to 24 degrees), and far (24 to 36) angle stacks. Figures 7.11-7.13 show the near-, mid-, and far-angle stacks for line II' affected by of the shallow igneous bodies. Note that at farther angles, the energy increases below the igneous bodies (blue arrows), the lateral resolution increases and noisy areas (green arrows) decrease.

7.5 Structure-Oriented Filtering

Structure-oriented processing applies simple spatially-limited filters along the dip and azimuth of seismic reflection events. In this work, I use a multiwindow Kuwahara, edge-preserving algorithm. In doing so, random noise is removed and lateral continuity is enhanced. The key to structure-oriented filtering is to differentiate between the dip and azimuth of the reflector and those of the overlying noise. Once we have estimated this dip and azimuth, I apply a filter to enhance signal along the reflector, much as interpreters do with time-structure and amplitude-extraction maps using interpretation workstation software. The most familiar filters are mean, median, and α-trim mean filters.

For this study, the three methods were used, all showing an overall similar result. Several iterations were run over the Amatitlán survey using the mean filter. The results of filtering on line HH' for none (Figure 7.15), two (Figure 7.16), six (Figure 7.17), and ten (Figure 7.18) interations show the impact on fault and igneous bodies. Note the improvement in the fault zone definition as the iterations increase (yellow Arrows), and better definition on the horizons below the igneous body (blue arrow). Additionally, Figures 7.19 and 7.20 show similarity attributes at t= 1335ms without and with ten passes of structure oriented filter iterations respectively. Note the increment on lateral resolution at the fault zone (orange arrow), and the in-situ igneous intrusive (red arrow).

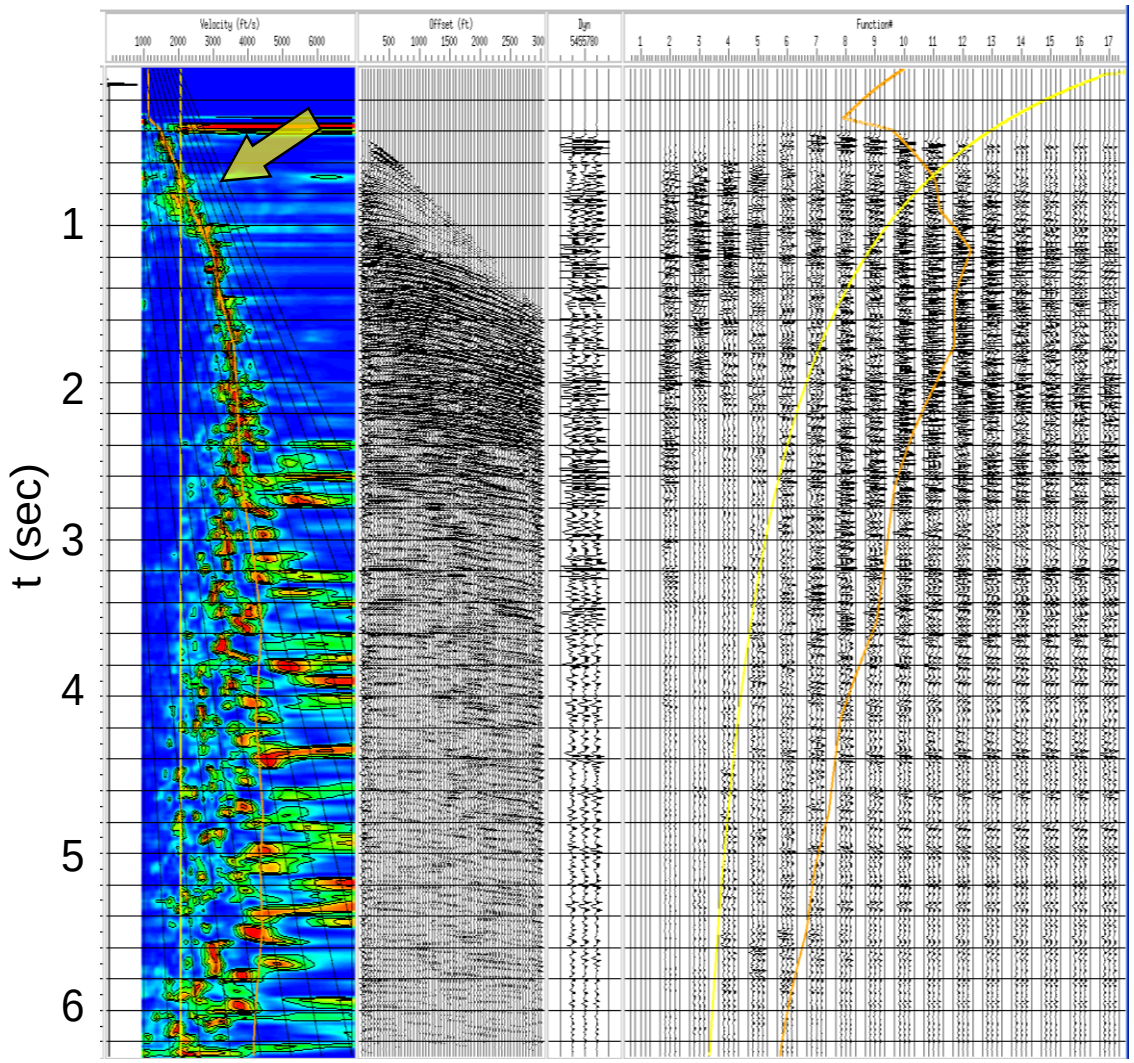

Figure 7.1 *Velocity spectral for areas without igneous bodies. Panel display in velocity analysis is divided into sections panels. From left to right are semblance, gather, dynamic stack, and velocity function stack. The semblance panel shows the plot of velocity guide functions (black lines), the picked velocities from previous picks (orange line) and the next picks (yellow line). The gather panel displays the offset-binned supergather. The dynamic panel shows a representation of a stack generated by the current velocity pick. The velocity function shows multi CDP stacks.*

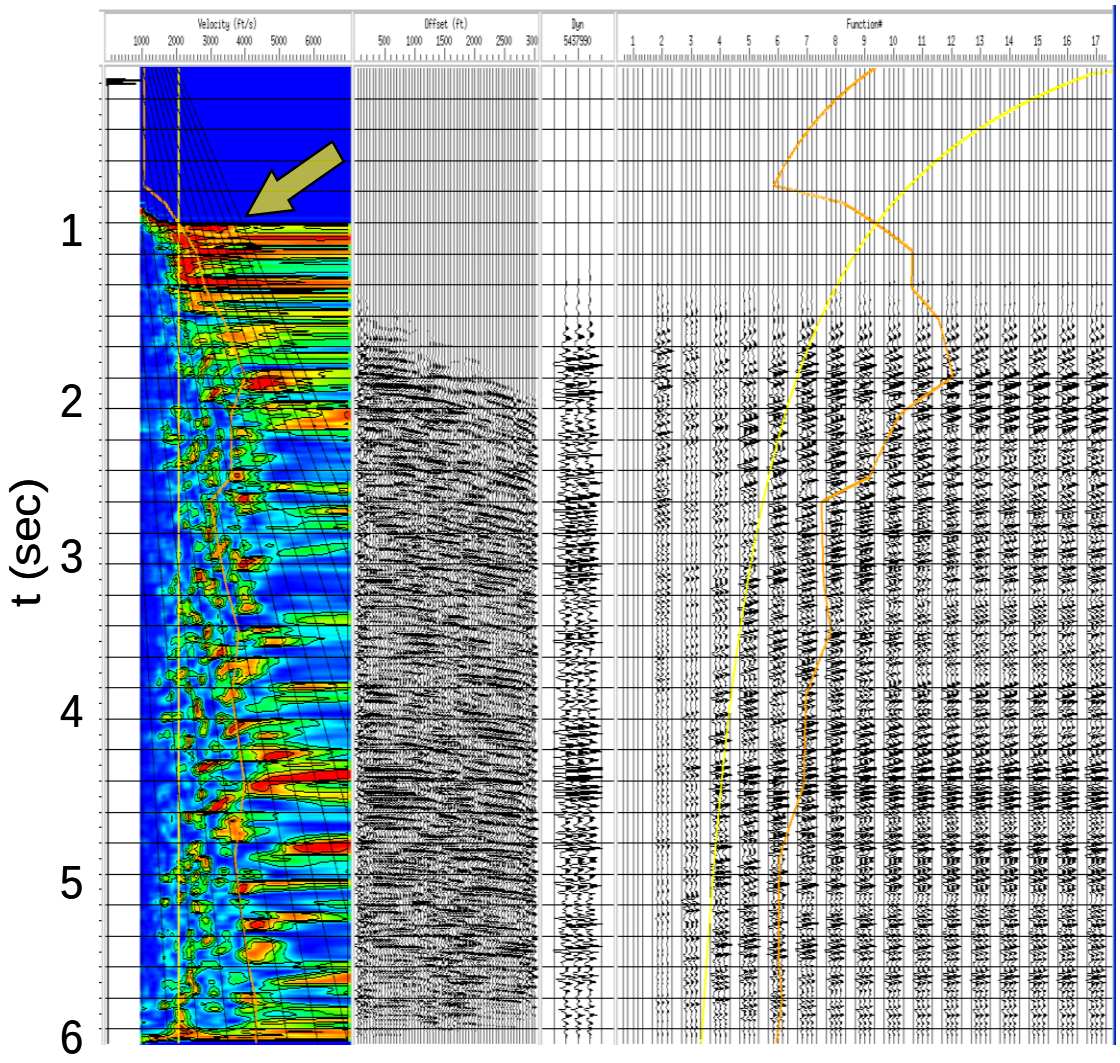

Figure 7.2 *Velocity spectrums for areas with igneous bodies. Panel displays velocity analysis and is divided into sections panels. From left to right are semblance, gather, dynamic stack, and velocity function stack. The semblance panel shows the plot of velocity guide functions (black lines), the picked velocities from previous picks (orange line) and the next picks (yellow line). The gather panel displays the offset-binned supergather. The dynamic panel shows a representation of a stack generated by the current velocity pick. The velocity function shows multi CDP stacks.*

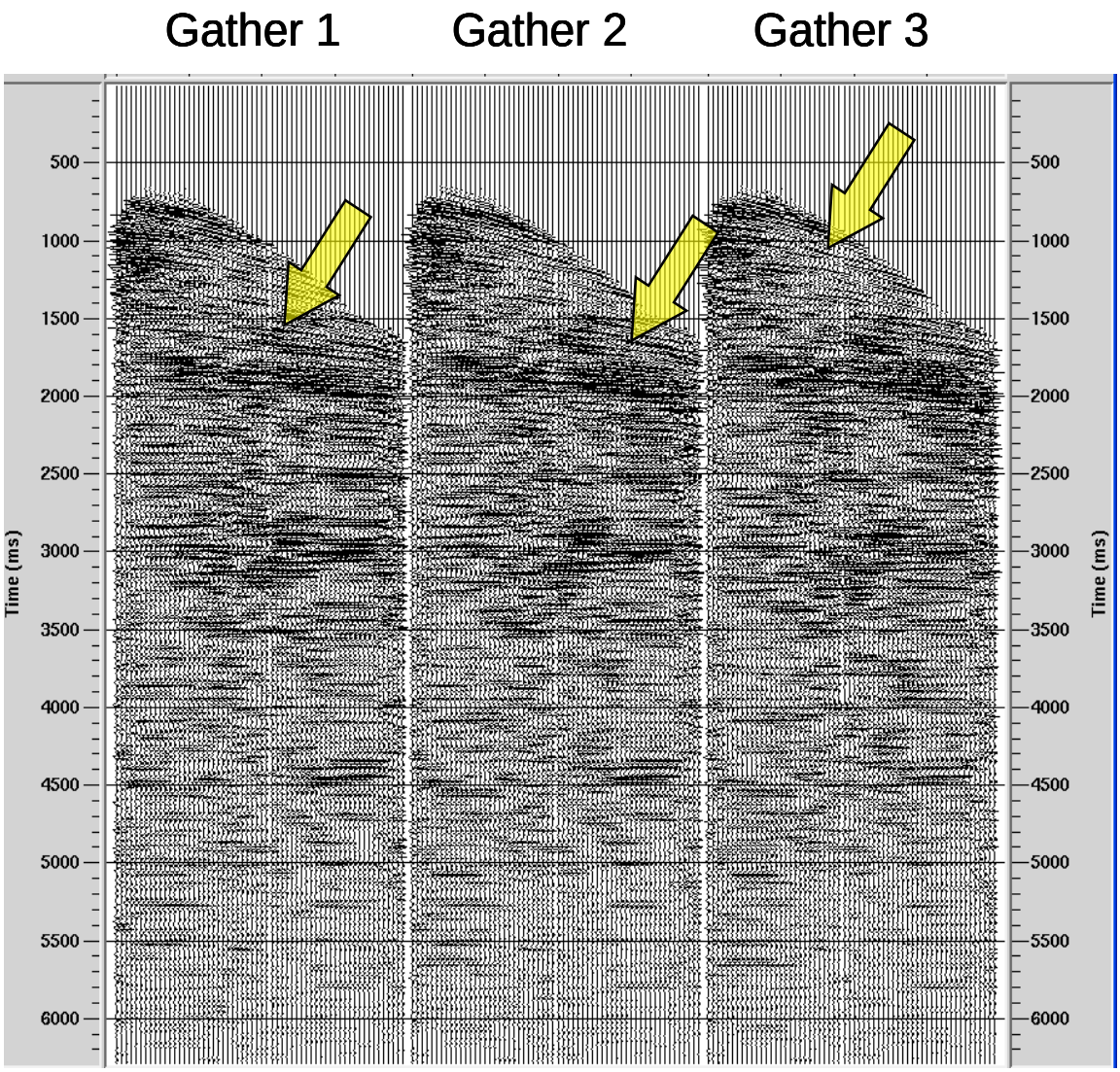

Figure 7.3 *Representatives migrated common reflection point gather correction resulting from the 2007 reprocessing by PEMEX*

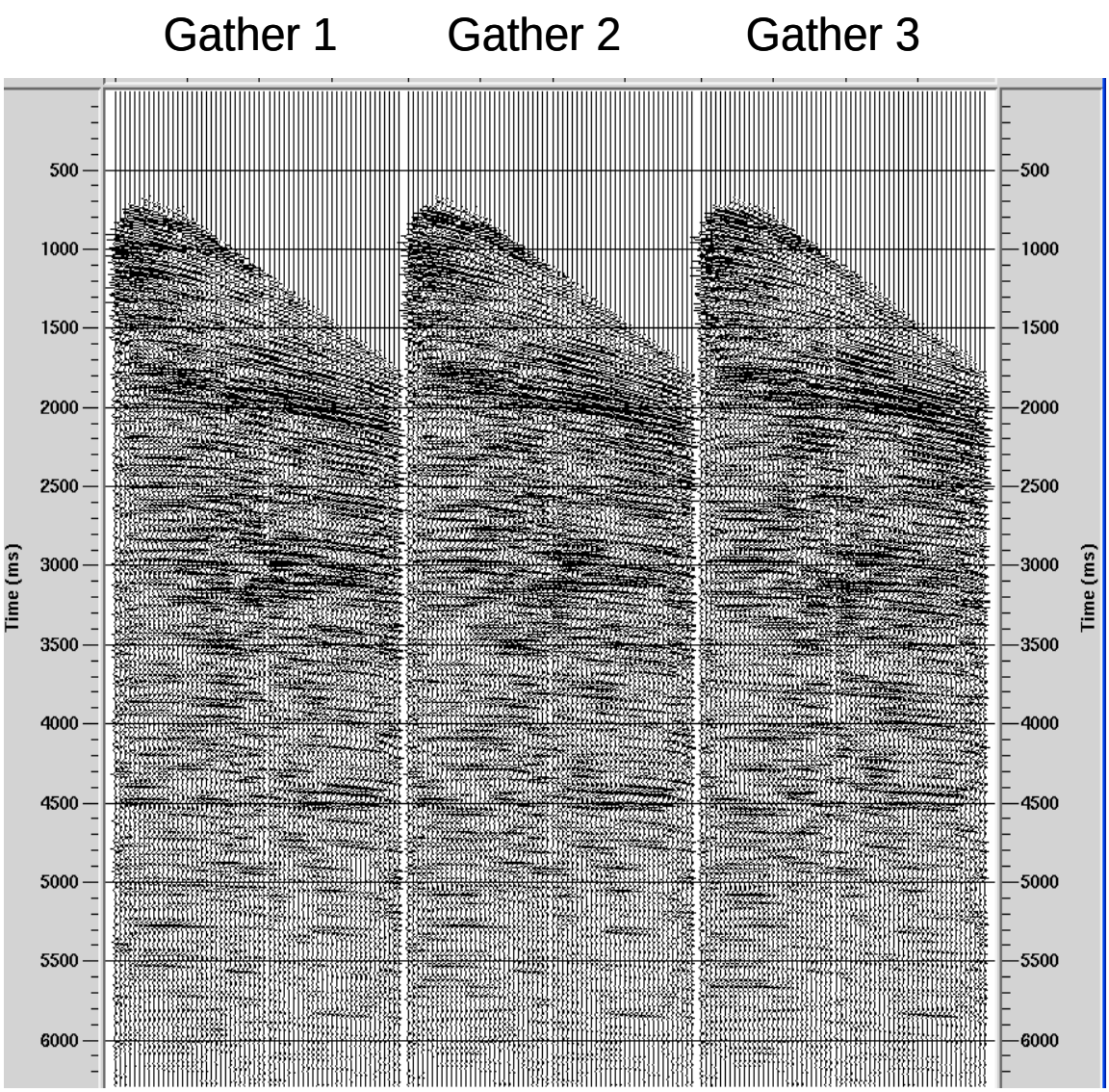

Figure 7.4 *Gather after application of reverse-NMO using the migration velocity*

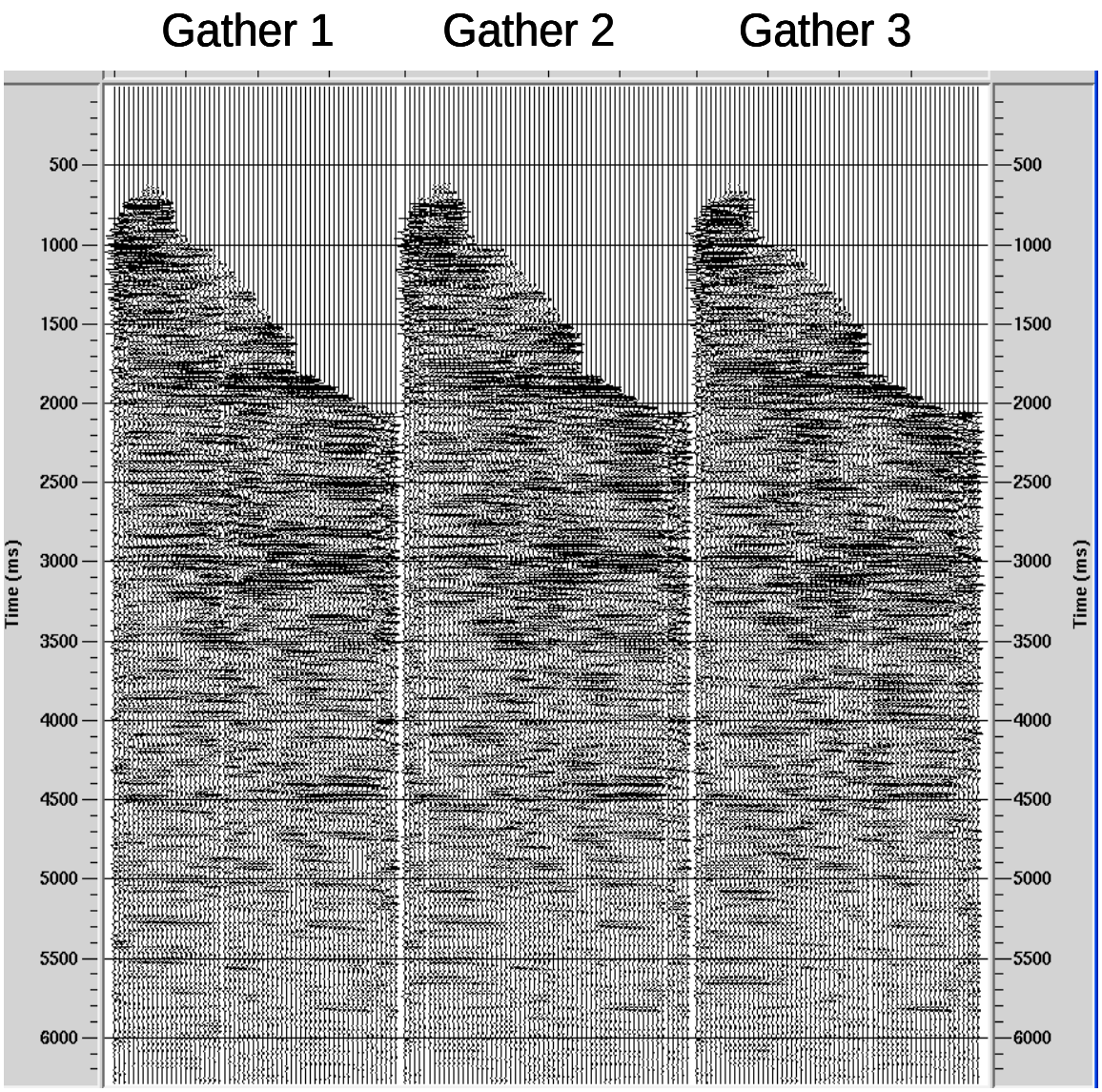

Figure 7.5 *The new and improved NMO correction (with mutes) using velocities picked with the knowledge that there is an overlying igneous intrusive*

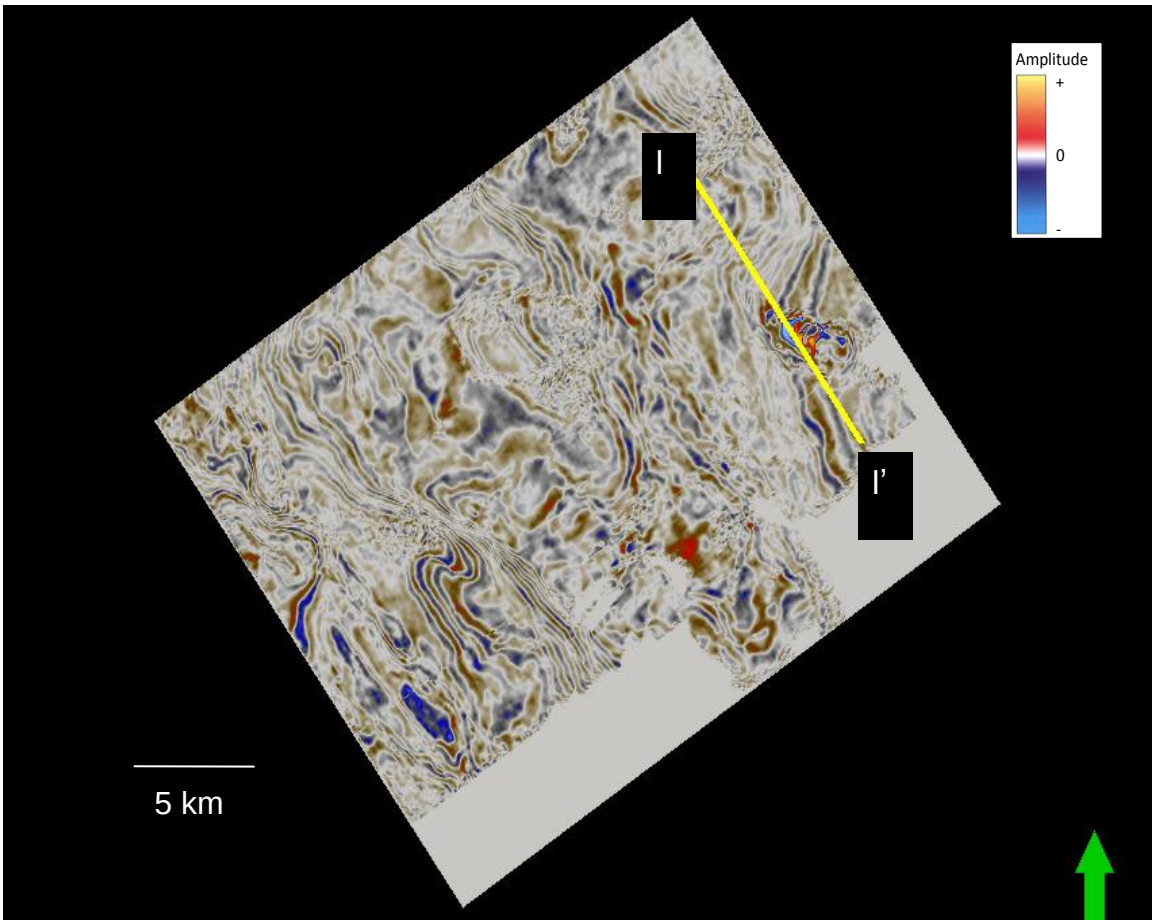

Figure 7.6 *Time slice at time t=1250ms through the migrated amplitude data showing the location of line II'.*

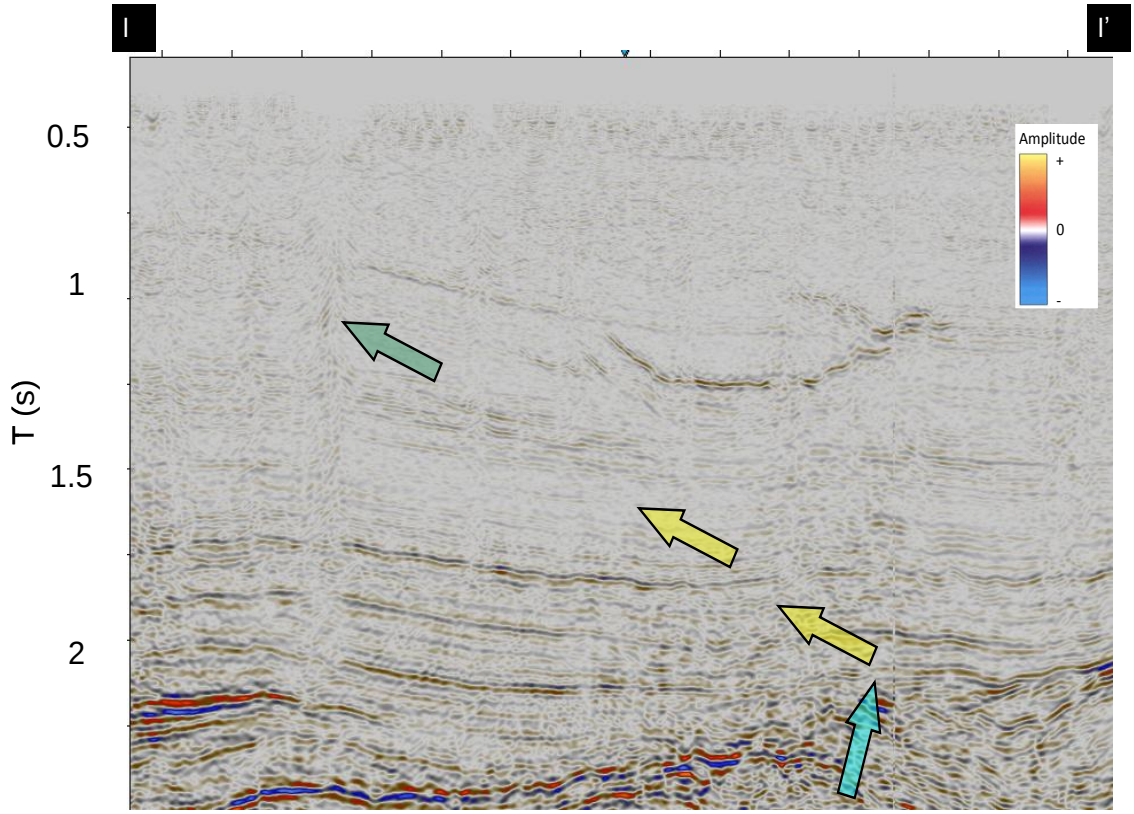

Figure 7.7 *Line II' after the prestack Kirchhoff time migration 2007 reprocessing effort green arrow indicates the noisy effect due to a shallow igneous body. Yellow arrows indicate the poor resolution of the horizons below igneous bodies. Blue arrow indicates the lost of energy for beds below igneous bodies.*

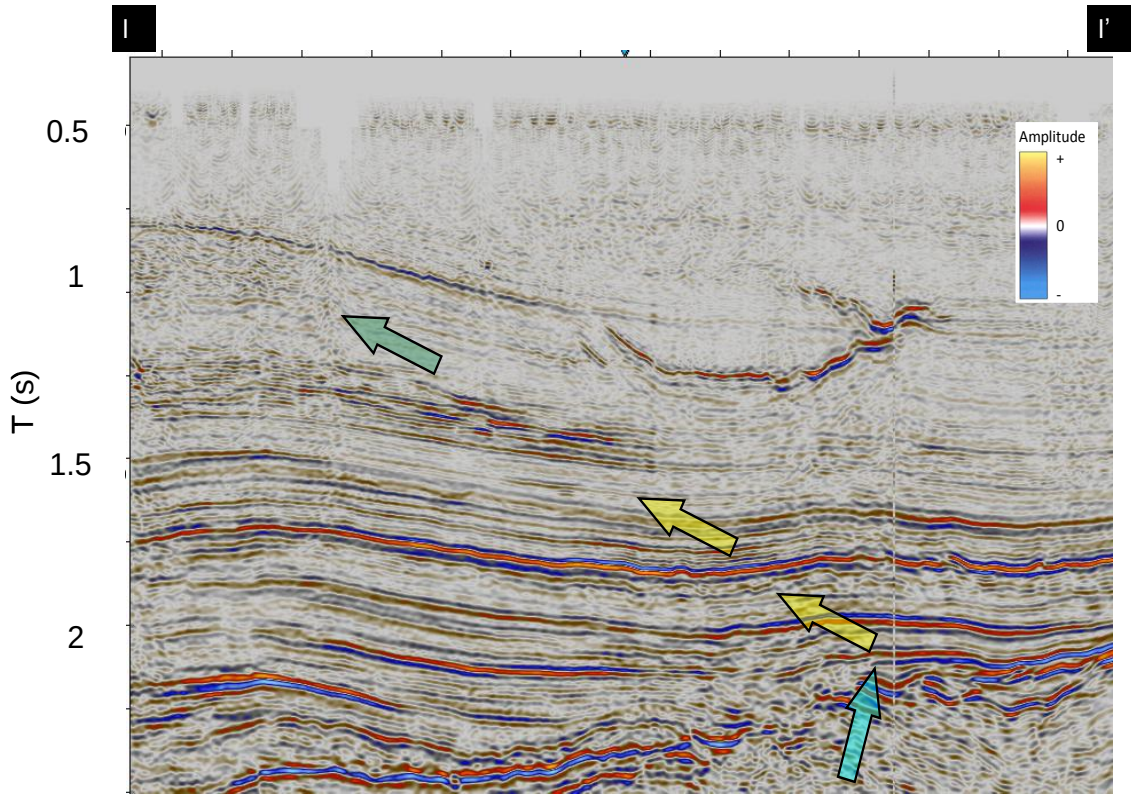

Figure 7.8 *Line II' after the residual velocity analysis workflow. Note the increase in vertical and lateral resolution and the more continuous horizon (yellow arrow) due to the noisy areas being removed.*

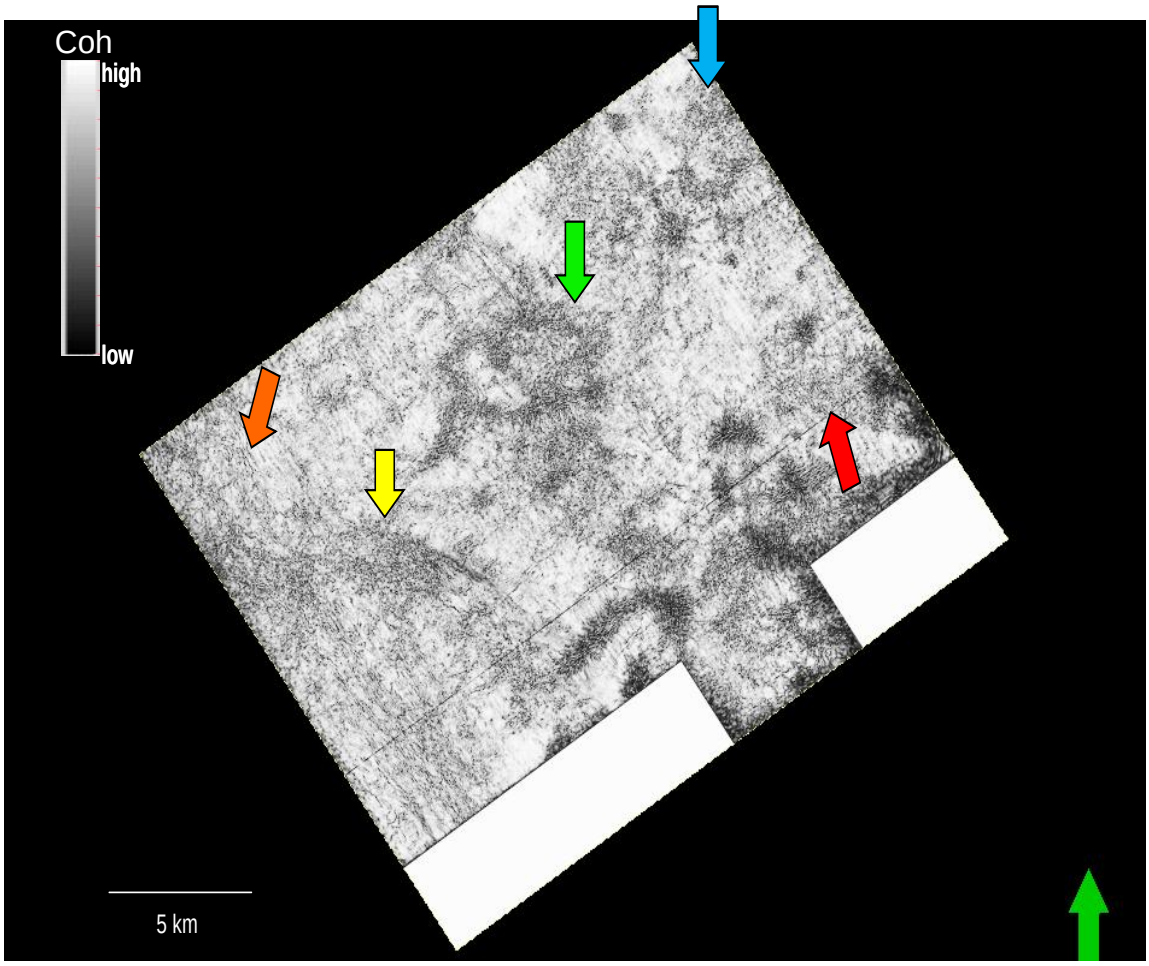

Figure 7.9 *Similarity attribute at t= 1750ms after the prestack Kirchhoff time migration 2007 reprocessing effort. Yellow, green, and blue arrows indicate location on the time slice affected by shallow igneous bodies. Red arrow indicates in-situ igneous body. Orange arrow indicates fault with a northwest-southeast trend.*

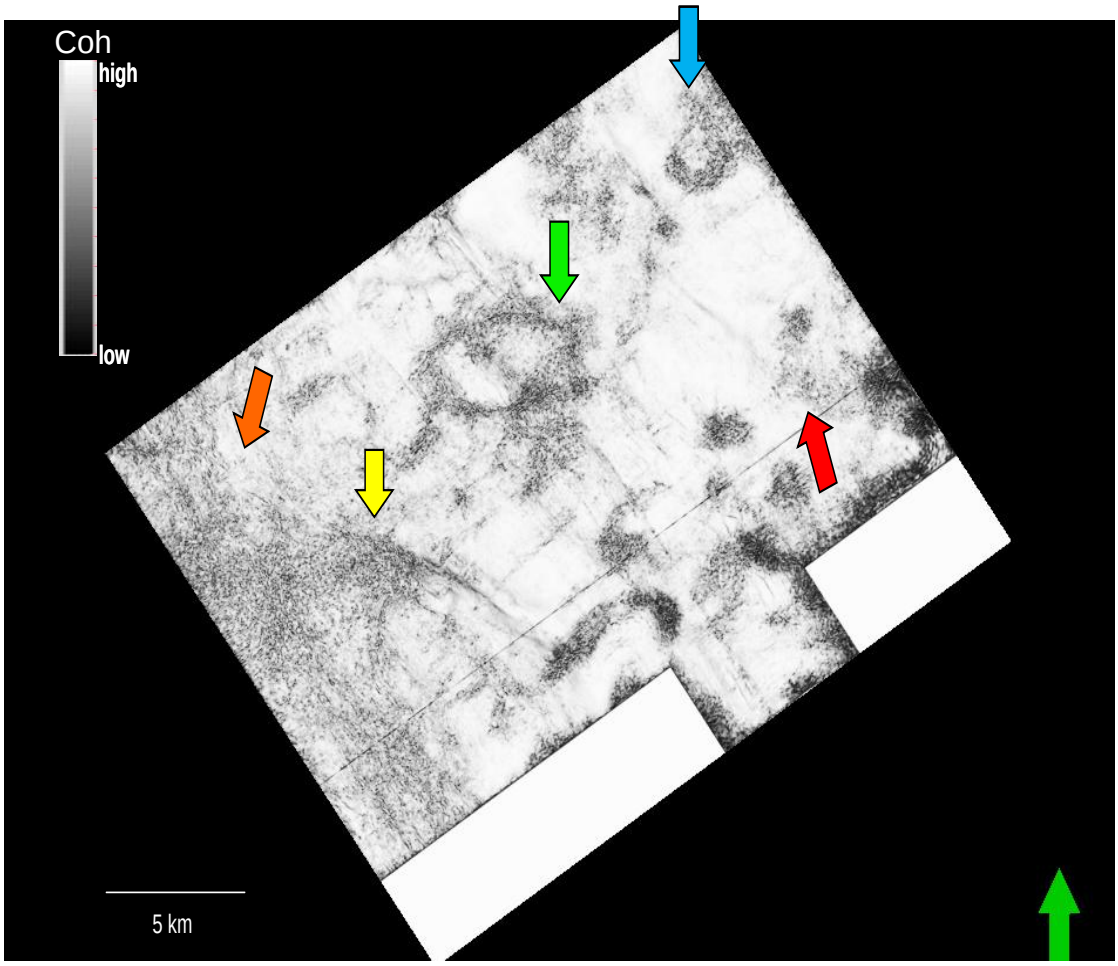

Figure 7.10 *Similarity attribute at t= 1750ms after the residual velocity analysis workflow. Yellow, green, and blue arrows indicate location on the time slice affected by shallow igneous bodies. Red arrow indicates in-situ igneous body. Orange arrow indicates fault with a northwest-southeast trend.*

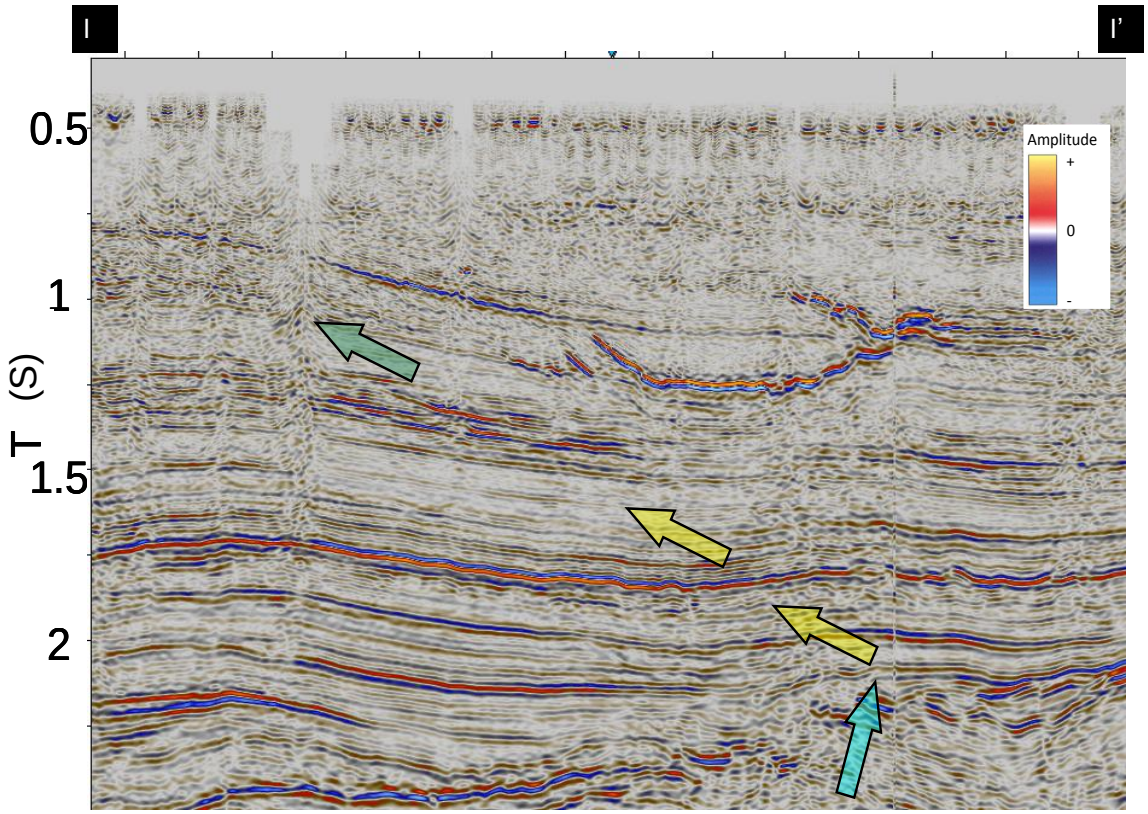

Figure 7.11 *Line II' near angle stack. Note that at farther angles, the energy increases below the igneous bodies (blue arrows), the lateral resolution increases, noisy areas (green arrows) decrease, and more continuity is observe on the beds (yellow arrows) .*

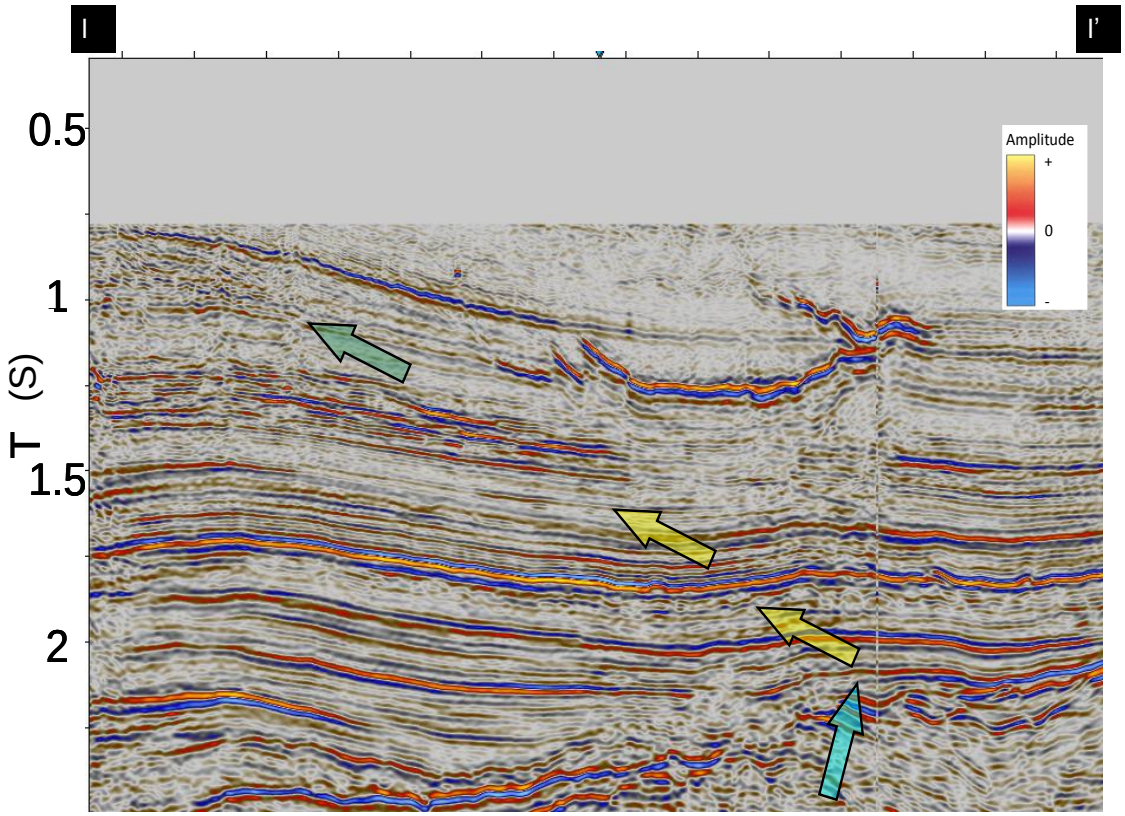

Figure 7.12 *Line II' mid-angle stack. Note that at farther angles, the energy increases below the igneous bodies (blue arrows), the lateral resolution increases, noisy areas (green arrows) decrease, and more continuity is observe on the beds (yellow arrows) .*

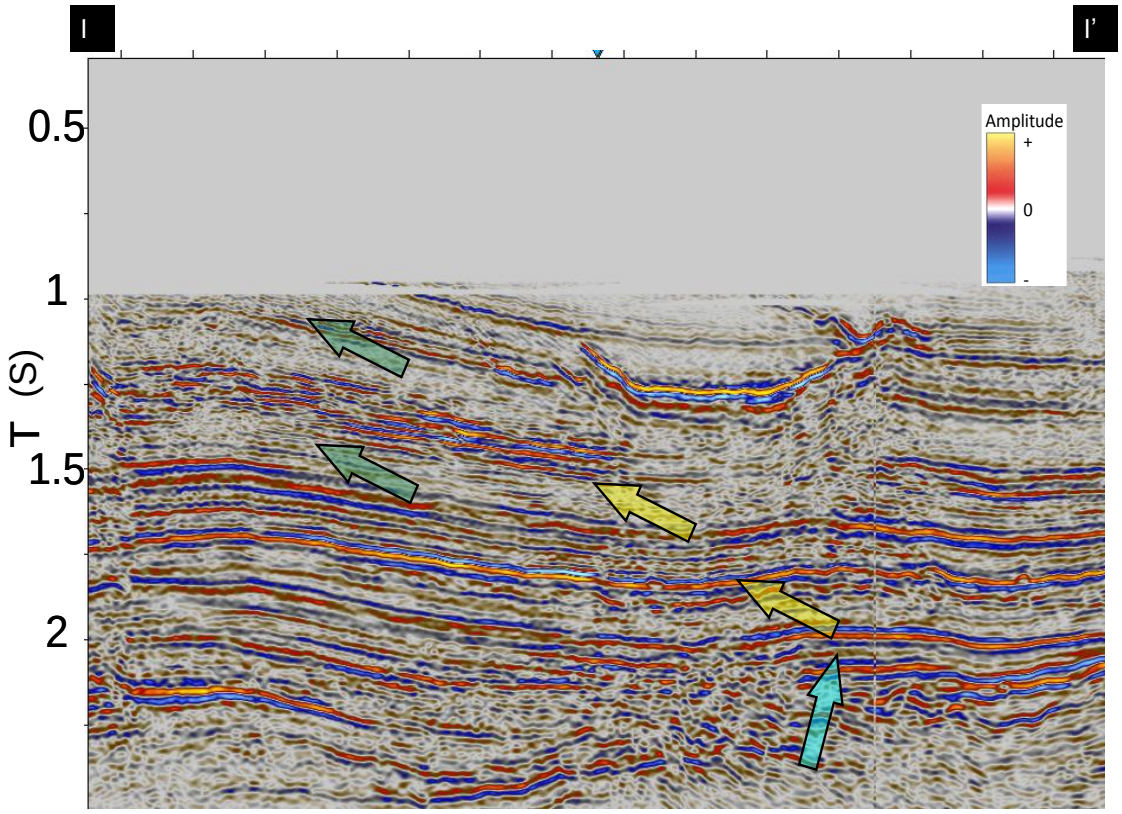

Figure 7.13 *Line II' far-angle stack. Note that at farther angles, the energy increases below the igneous bodies (blue arrows), the lateral resolution increases, noisy areas (green arrows) decrease, and more continuity is observe on the beds (yellow arrows) .*

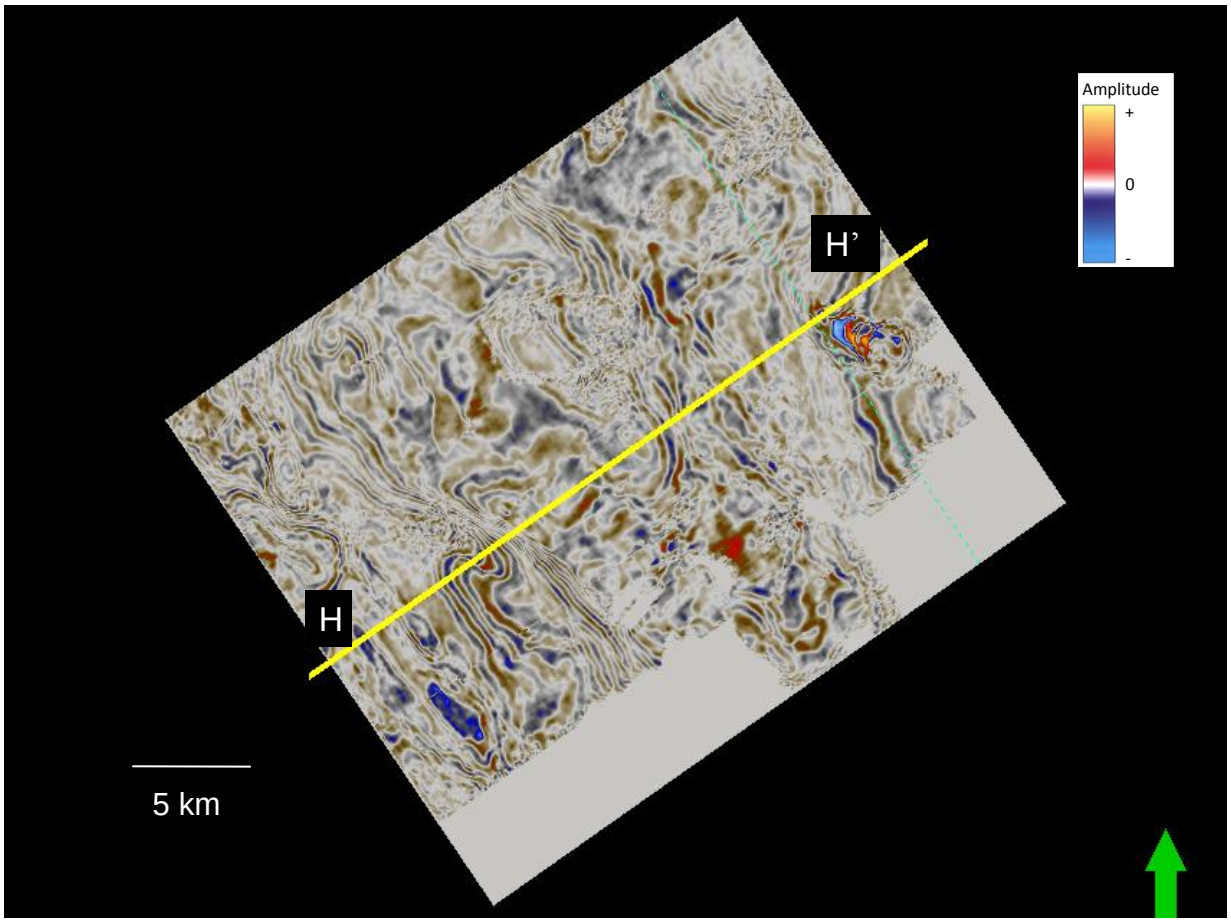

Figure 7.14 *Time slice at t=1250ms showing location of line HH'.*

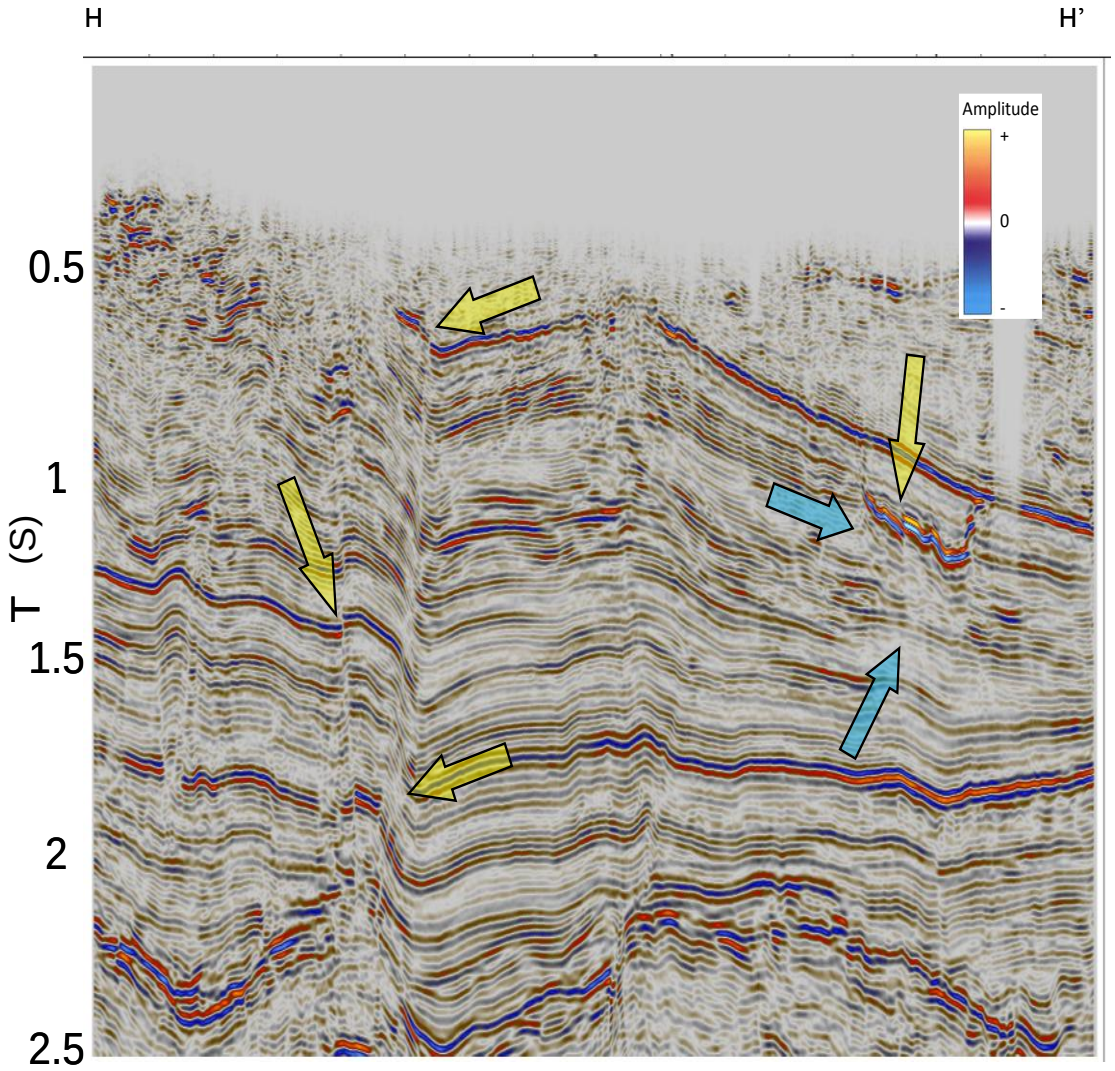

Figure 7.15 *Seismic line without structure oriented filter iteration for inline HH'. Note the improvement in the fault zone definition as the iterations increase (yellow Arrows), and better definition on the horizons below the igneous body (blue arrow).*

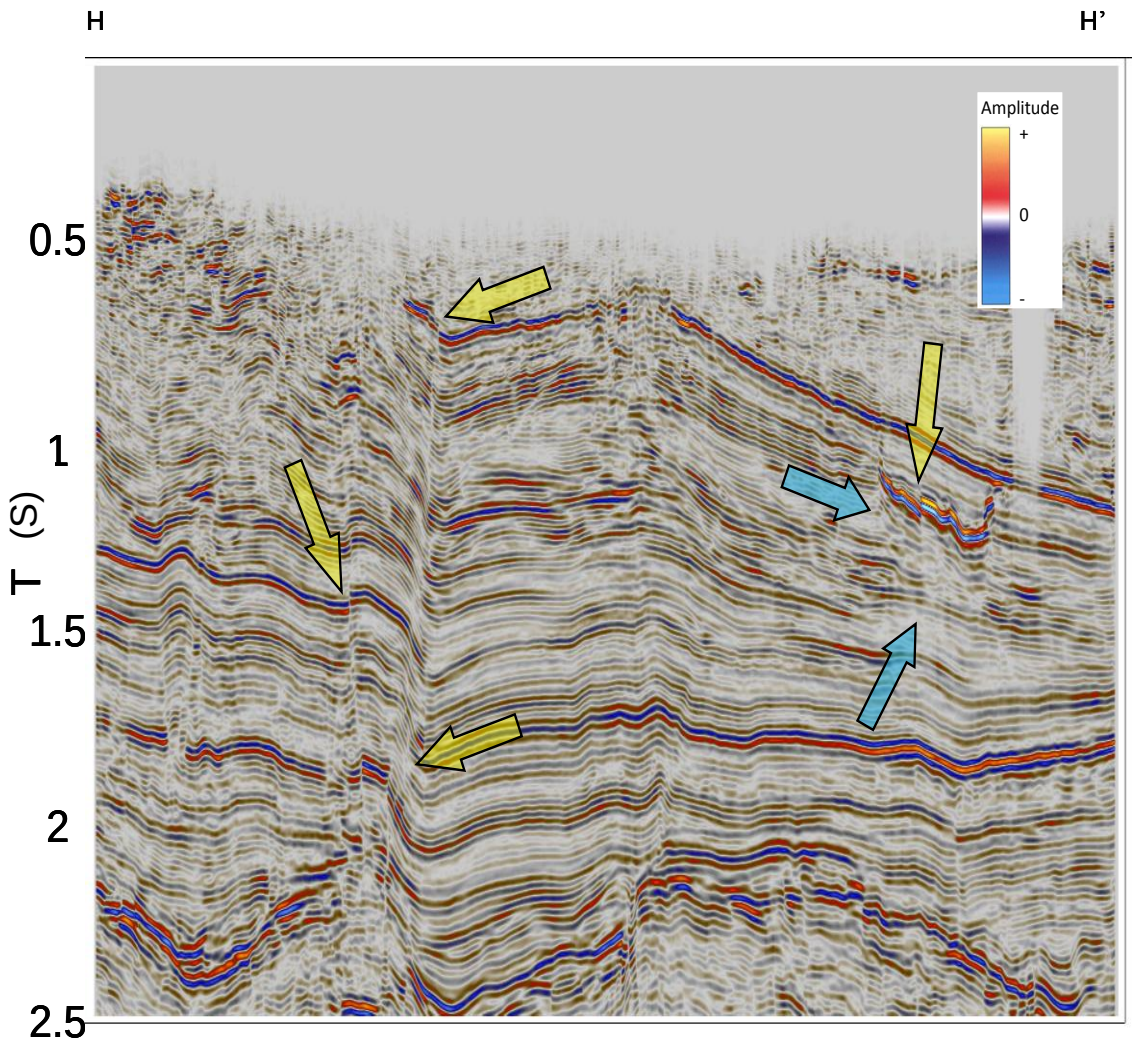

Figure 7.16 *Seismic line HH' after two passes of structure-oriented filter. Note the improvement in the fault zone definition as the iterations increase (yellow Arrows), and better definition on the horizons below the igneous body (blue arrow).*

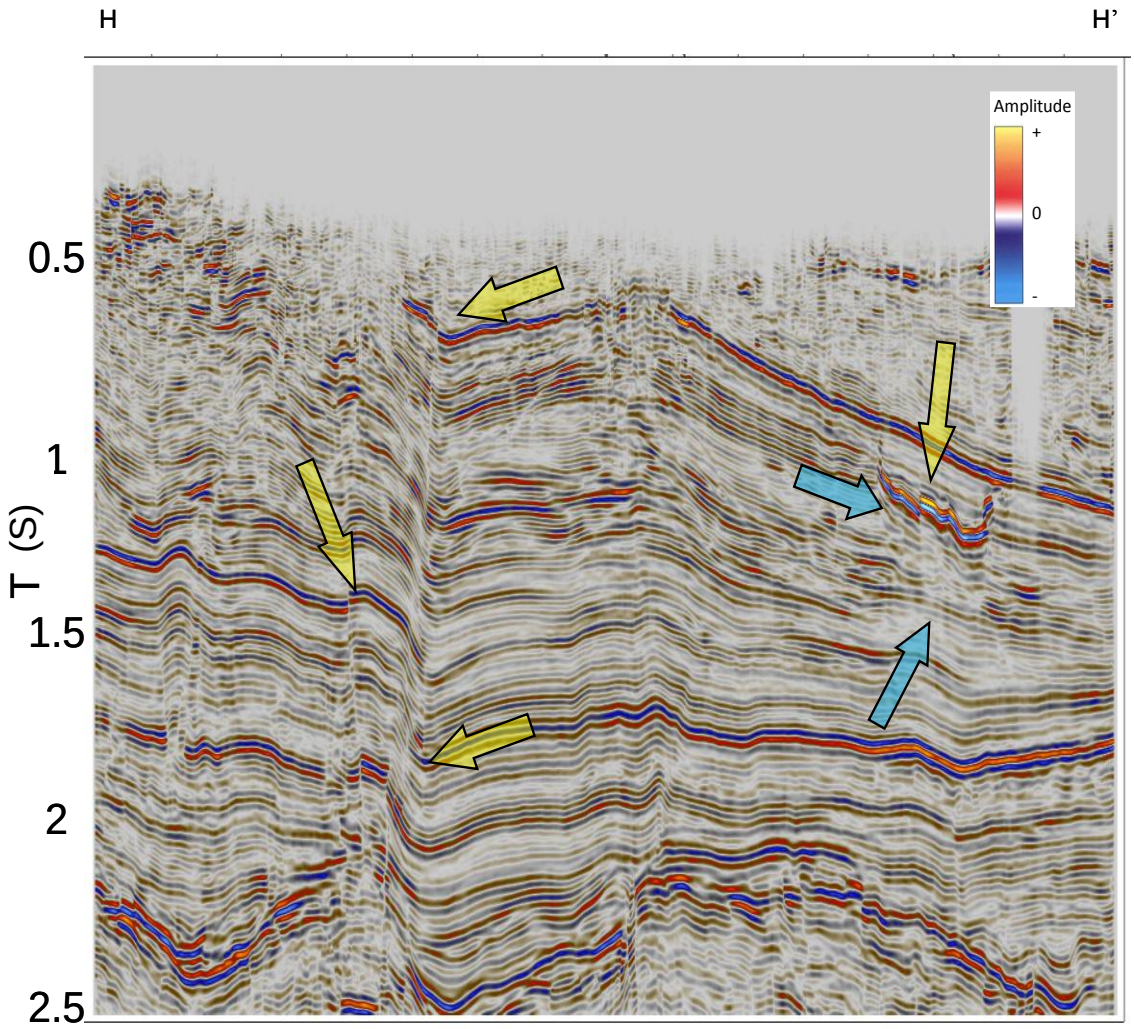

Figure 7.17 *Seismic line HH' with six passes of structure oriented filter iteration. Note the improvement in the fault zone definition as the iterations increase (yellow Arrows), and better definition on the horizons below the igneous body (blue arrow).*

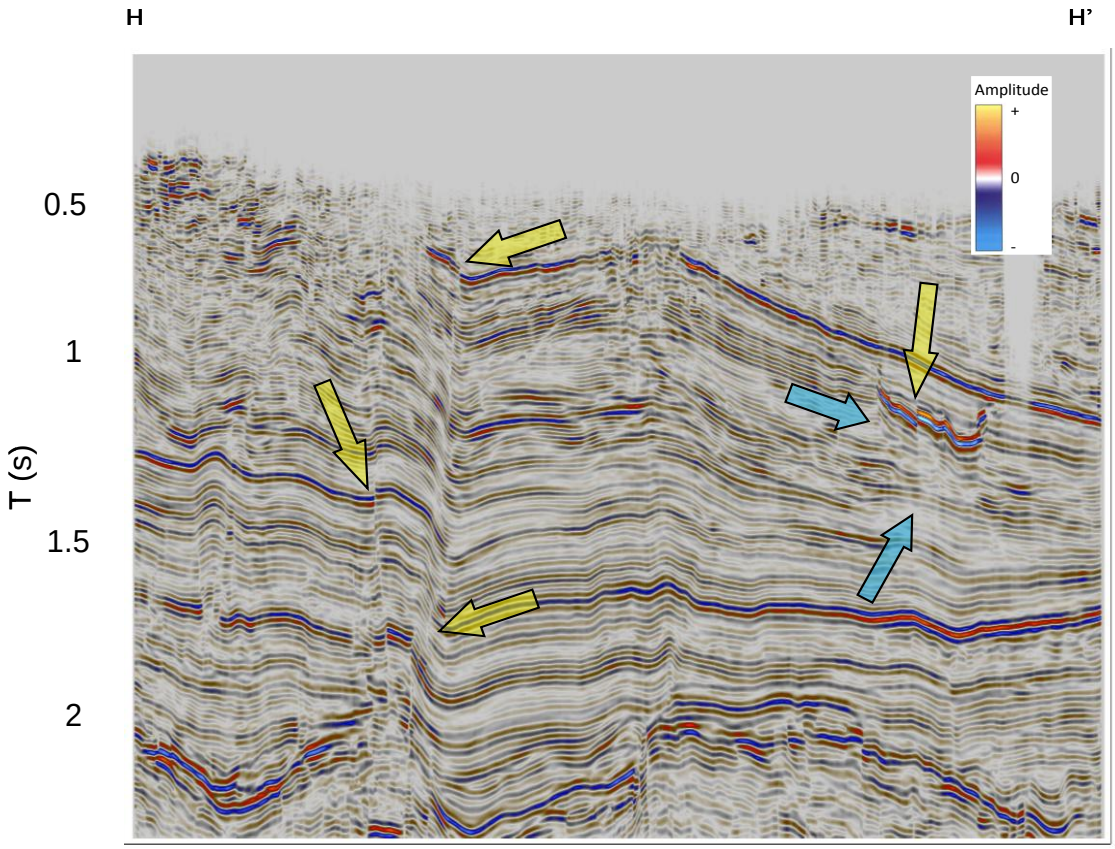

Figure 7.18 *Seismic line HH' with ten passes of structure oriented filter. Note the improvement in the fault zone definition as the iterations increase (yellow Arrows), and better definition on the horizons below the igneous body (blue arrow).*

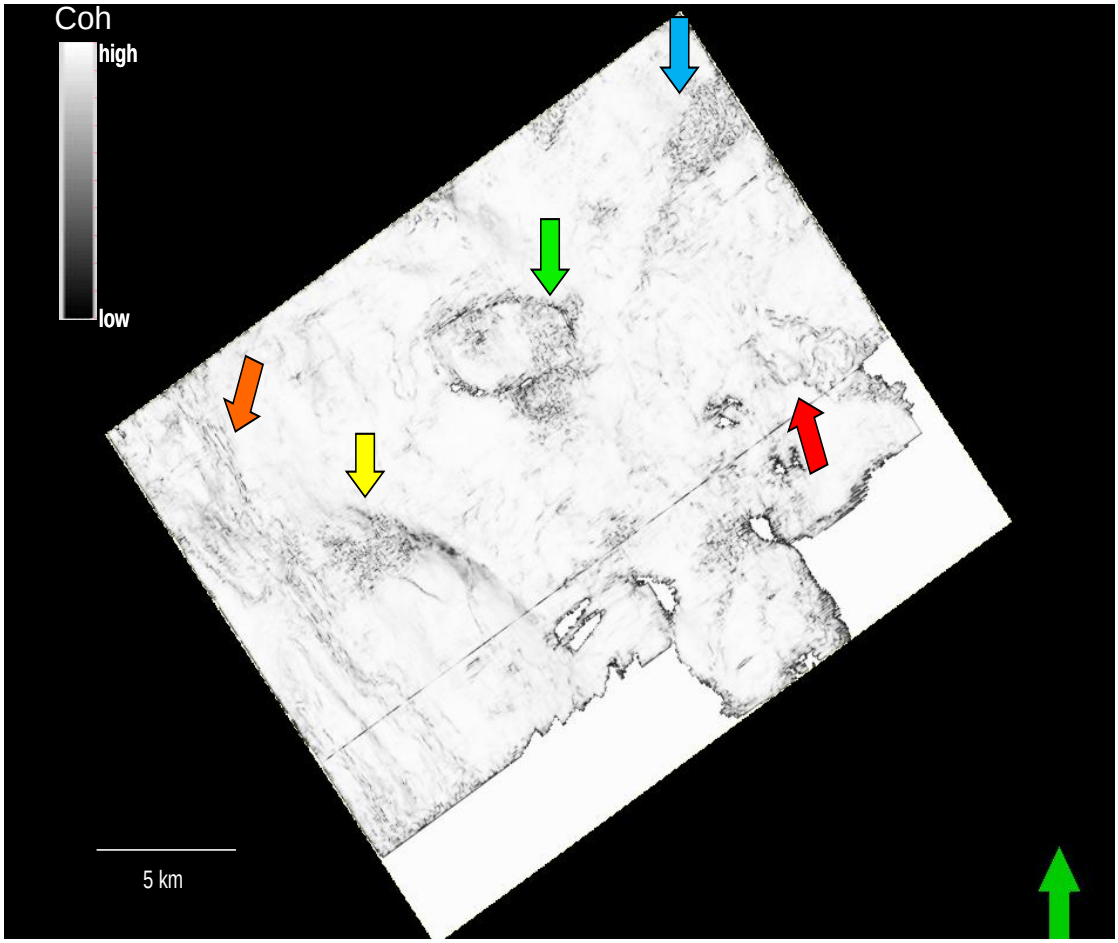

Figure 7.19 *Similarity attribute at t= 1335ms without structure oriented filter iteration. Yellow, green, and blue arrows indicate location on the time slice affected by shallow igneous bodies. Red arrow indicates in-situ igneous body. Orange arrow indicates fault with a northwest-southeast trend.*

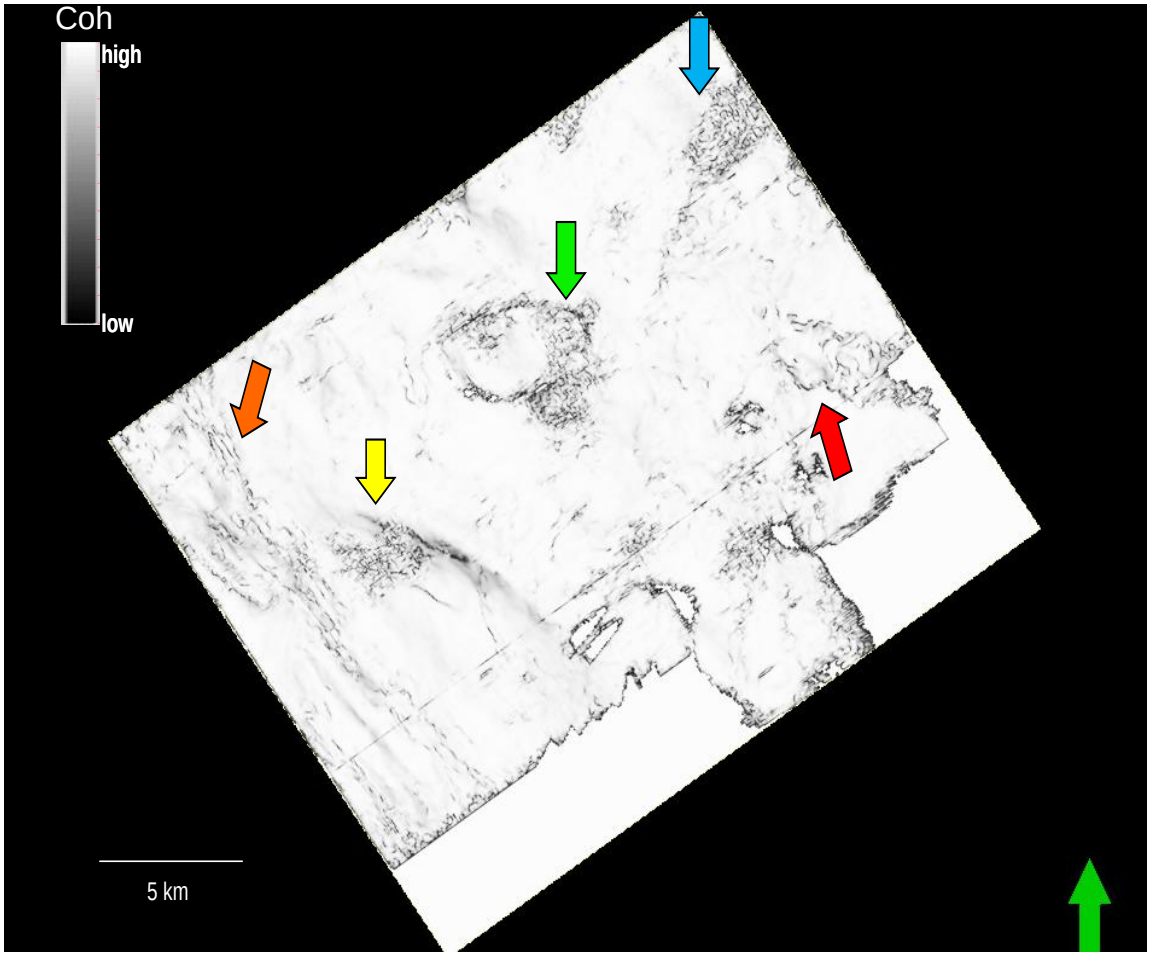

Figure 7.20 *Similarity attribute at t= 1335ms with 10 passes of structure oriented filter. Yellow, green, and blue arrows indicate location on the time slice affected by shallow igneous bodies. Red arrow indicates in-situ igneous body. Orange arrow indicates fault with a northwest-southeast trend.*

Conclusion

The primary exploration objective in the Amatitlán survey area to map the Chicontepec formation is handicapped by the presence of shallow volcanics that disrupt the deeper signal. The Chincontepec formation is composed of low-permeability turbidites and sheet sands that are encased in a shale matrix and cut by incoherent mass transport complexes. Geomorphological recognition of turbidites and mass transport complexes is made by their relatively chaotic texture as seen on seismic attributes. This pattern is overprinted by the chaotic nature of the seismic data associated with the overlying volcanics. Through careful statics, trace balancing, and velocity analysis, many of these disruptions can be attenuated, particularly those that give rise to 'shadows' beneath the high impedance volcanics. Sills that are intruded parallel to stratigraphic horizons do not cause significant problems in deeper seismic data. However, sills that cut upward from horizon to horizon as well as stacked sills, generate interbed multiples and downgoing diffracted direct waves that correlates to low seismic coherence seen at greater depths.

Seismic modeling allowed me to understand the ray-path and wavefield behavior as they propagate through extrusive and intrusive igneous rocks. Reprocessing workflow focuses on a more careful velocity analysis in areas affected by igneous bodies, providing improved vertical and lateral resolution in areas below the extrusive and intrusive igneous bodies. In addition, the new reprocessing workflow increased some of the energy deep in the section. I found

seismic attributes and magnetic data to be excellent tools in mapping the shallow igneous features, thereby highlighting areas for careful velocity analysis.

Additional processing including angle gathers and structure-oriented filtering increases the vertical and lateral resolution for areas below the intrusive and extrusive bodies. Although the lateral resolution decreases at the father angles below the igneous bodies, such 'undershooting' results in an increase in energy increases and decrease in noise, resulting in more continuous reflectors at the target horizon. .Structure-oriented filtering improves fault zone definition as well as more coherent reflectors below the igneous bodies.

References

Berbauer, S., T. Mukerji, and P. Hennings, 2003, Improving curvature analyses of deformed horizons using scale-dependent filtering techniques: AAPG Bulletin, **87**, 1255-1272.

Bermúdez, J., J. Araujo-Mendieta, M. Cruz-Hernández, H. Salazar-Soto, S. Brizuela-Mundo, S. Ferral-Ortega, and O. Salas-Ramírez, 2006, Diagenetic history of the turbiditic litharenites of Chicontepec Foramtion, northern Veracruz: controls on the secondary porosity for hydrocarbon emplacement: Gulf Coast Association of Geological Societies Transactions, **56**, 65-72.

Cantu Chapa, A., 2001, Mexico as the western margin of Pangea based on biostratigrapic evidence from the Permian to the Lower Jurassic, in Bartolini, C., Buffler, R. T., and Cantu-Chapa, A., *eds.*, The Western Gulf of Mexico Basin-Tectonics, Sedimentary Basin, and Petroleum System: AAPG Memoir, no. 75, 1-28.

Chopra, S., and K. Marfurt, 2007, Seismic attributes for prospect identification and reservoir Characterization: Geophysical Development, **11,** Society of Exploration Geophysics.

Davies, R. J., J. Cartwright, J. Stewart, A. Lappin, and M. Underhill, 2004, 3D seismic technology: Application to the exploration of sedimentary basins: Geological Society of London Memoir **29**.

Deregowski, S.M., 1990, Common-offset migrations and velocity analysis: First Break, **8**, no. 6, 224-234.

Diaz, G., 2008, Sequence stratigraphy of Chicontepec Play, Tampico-Misanta basin, Mexico: M.S. Thesis, the University of Oklahoma.

Klarner, S., B. Ujetz, R. Fontana, and J. Altenkirch, 2006, Seismic signature of Upper Cretaceous volcanics: Santos basin, Brazil: 68th International Meeting EAGE Expanded Abstracts, 105.

Garten, P., M. Houbier, S. Planke, and H. Svensen, 2008, Vent complex at Heidrun: 77th Annual International Meeting of the SEG, Expanded Abstracts, 809-813.

Goldhammer, R.K., and C. A. Jhonson, 2001, Middle Jurassic-Upper Cretaceous paleogeographic evolution and sequence-stratigraphic framework of the northwest Gulf of Mexico rim, in Bartolini, C., Buffler, R. T., and Cantu-Chapa, A., eds., The Western Gulf of Mexico Basin-Tectonics, Sedimentary Basin, and Petroleum Systems: AAPG Memoir **75**, 45-81.

Grauch, V. J. S. and G. R. Keller, 2004, Gravity and aeromagnetic expression of tectonic and volcanic elements of the southern San Luis Basin, New Mexico and Colorado: New Mexico Geological Society, 55th Annual Field Conference Guidebook, 230–243.

Horbury, A. D., S. Hall, F. Gonzalez-P., D. Rodrıguez-F., A. Reyes-F., P. Ortiz-G., M. Martinez-M., and G. Quintanilla-R., 2003, Tectonic sequence

stratigraphy of the western margin of the Gulf of Mexico in the late Mesozoic and Cenozoic: Less passive than previously imagined, in C. Bartolini, R. T. Buffler, and J. Blickwede, eds., The Circum-Gulf of Mexico and the Caribbean: Hydrocarbon habitats, basin formation, and plate tectonics: AAPG Memoir **79**, 184–245.

Luo, Y., W. G. Higgs, and W. S. Kowalik, 1996, Edge detection and stratigraphic analysis using 3D seismic data: 66th Annual International Meeting, SEG, Expanded Abstracts, 324-327.

Olubunmi, O. E., 2009, Integrated geophysical investigation of linkages between Precambrian basement and sedimentary structures in the Ucayaly Basin, Peru; Fort Worth Basin, Texas; and Osage County: PhD Thesis, the University of Oklahoma.

Pindell, J. L., and L. J. Kennan, 2001, Kinematic evolution of the Gulf of Mexico and Caribbean: Proceedings of Gulf Coast Section, Society for Sedimentary Geology (SEPM) Foundation, 21st Annual Research Conference, Petroleum Systems of Deep-Water Basins, 193–220.

Verduzco, B., D. J. Fairhead., C. M. Green, and C. MacKenzie, 2004, New insight into magnetic derivatives for structural mapping: The Leading Edge, **23**, 116-119.

Yilmaz, O., 2001, Seismic data analysis, 2nd. Ed.: Society of Exploration Geophysics